

INVESTIGATION OF THE NODULAR MICROSTRUCTURE OF SELECTED
SILSESQUOXANE AND EPOXY THERMOSETTING RESINS

By

KYLE KATHAN

A DISSERTATION PRESENTED TO THE GRADUATE SCHOOL
OF THE UNIVERSITY OF FLORIDA IN PARTIAL FULFILLMENT
OF THE REQUIREMENTS FOR THE DEGREE OF
DOCTOR OF PHILOSOPHY

UNIVERSITY OF FLORIDA

2005

Copyright 2005

by

Kyle Kathan

This work is dedicated to my grandparents William and Shirley Gray of Paulsboro, New Jersey.

ACKNOWLEDGMENTS

I would first and foremost like to thank my family, my parents Chris and Russ Kathan, my sister Kendra Kathan, my uncle Steven Gray, and my wife Dana for their support and love while pursuing my graduate studies.

I would like to additionally thank my advisor, Dr. Ronald Baney, who has made graduate school a worthwhile endeavor for me and has helped me through all of the academic challenges I have faced over the past four years.

As far as my research goes, I must first acknowledge the University of Florida Alumni Foundation for supporting me with a generous fellowship over the past four years, which has allowed me to pursue the research that is of the most interest to me. Additionally I would like to acknowledge the University of Florida McKnight Brain Institute (MBI) for allowing me to use its phenomenal facilities. I would like to acknowledge Jim Rocca and Tim Vaught of the MBI for their help with my research. I would like to thank Jim Rocca for all his help with NMR theory and practice and thank Tim Vaught for helping me with my optical microscopy work.

Additionally I would like to acknowledge the University of Florida Particle Engineering Research Center (ERC) for its help with my research. Specifically, I would like to thank Dr. Kevin Powers of the ERC for guiding my early work when I first started at UF.

I would like to thank Dr. Jack Mecholsky of the UF Materials Science and Engineering Department for helping me to better understand mechanical properties and fractals, topics which consumed a large portion of this research.

Lastly I would like to thank the entire Baney group. It is my feeling that the Baney group is far and away the most academically diverse group in the MSE department with people studying everything from nuclear fuel to bioactive materials. Four years of the Baney group have proved to be invaluable.

TABLE OF CONTENTS

ACKNOWLEDGMENTS	iv
ABSTRACT	xv
CHAPTER	
1 INTRODUCTION AND OVERVIEW OF CHAPTERS.....	1
1.1 Research Introduction.....	1
1.2 Fractal Basics.....	2
1.3 Materials Overview	4
1.4 Chapter Outline.....	6
2 FRACTALS AND FRACTURE	7
2.1 Introduction to Fractals.....	7
2.2 Fractals in Nature.....	8
2.3 Fractal Dimension.....	9
2.4 Mechanical Properties	15
2.5 Conclusions.....	18
3 EPOXIES, SILSESQUIOXANES, AND NODULAR STRUCTURE REVIEW.....	20
3.1 Introduction.....	20
3.2 Review of Nodular Epoxies.....	20
3.2.1 Introduction to Epoxies	20
3.2.2 Processing and Synthesis Factors Affecting Nodule Size.....	21
3.2.3 Observations of Nodule Size.....	24
3.2.4 Mechanical Properties of Nodular Epoxy Resins.....	28
3.3 Review of Silsesquioxanes	31
3.3.1 Introduction to Silsesquioxanes.....	31
3.3.2 Applications of Silsesquioxanes.....	34
3.3.3 Characterization of Silsesquioxanes.....	36
3.4 Conclusions.....	41
4 FRACTURE PROPERTIES OF EPOXY RESIN.....	42
4.1 Introduction.....	42
4.2 Epoxy Synthesis and Processing	44
4.3 Methodology and Experimental	45

4.3.1	Characterization of Mechanical Properties of Epoxy Resins	46
4.3.1.1	Introduction	46
4.3.1.2	Modulus.....	46
4.3.1.3	Failure stress.....	49
4.3.1.4	Flaw size.....	49
4.3.1.5	Fracture mechanics and toughness.....	52
4.3.2	Studies of Nodular Microstructure and Nodule Size.....	54
4.3.2.1	Scanning electron microscopy	54
4.3.2.2	Solvent extraction and particle size.....	56
4.3.2.3	Iodine staining of surfaces.....	58
4.3.3	Investigation of Fractal Dimensional Increment	60
4.3.3.1	Introduction	60
4.3.3.2	Flaw to mirror size	61
4.3.3.3	Non-destructive slit-island method	64
4.3.3.4	Hand calculations of fractal dimensional increment	70
4.3.3.5	Calculation of fractal dimensional increment by Image-Pro.....	73
4.3.3.6	Comparison of methods of measuring fractal imension.....	74
4.4	Structural Parameter a_0	75
4.4.1	Calculating a_0	75
4.4.2	Relationship of Fractal Dimensional Increment to a_0	76
4.4.3	Error Analysis of a_0	78
4.5	Results and Discussion	78
4.6	Conclusions.....	80
5	SILSESQUIOXANES: GROWTH, STRUCTURE, AND CHARACTERISTICS ..	82
5.1	Introduction.....	82
5.2	Polysilsesquioxane Synthesis and Processing	84
5.2.1	Polymer Synthesis	84
5.2.2	Polysilsesquioxane Monolith Synthesis	86
5.3	Experimental.....	87
5.3.1	Characterization of Polymer	87
5.3.1.1	Viscosity.....	87
5.3.1.2	Matrix assisted laser desorption ionization	90
5.3.1.3	Nuclear magnetic resonance.....	92
5.3.1.4	Fourier transform infrared spectroscopy	99
5.3.2	Condensation of Polysilsesquioxanes.....	100
5.3.3	Characterization of Nodular Microstructure	101
5.4	Polymethylsilsesquioxane.....	106
5.6	Conclusions.....	107
6	RESULTS, DISCUSSIONS, AND FUTURE WORK.....	109
6.1	Results and Discussion	109
6.1.1	Calculating Fractal Dimension with Optical Microscopy	109
6.1.2	Nodular Microstructure of Epoxies and Fractal Analysis of Failure	109
6.1.3	Synthesis and Characterization of Silsesquioxanes.....	110

6.2 Future Work.....	111
APPENDIX	
A ERROR ANALYSIS OF THE WEST MECHOLSKY PASSOJA THEORY	114
A.1 Introduction.....	114
A.2 Sources of Error.....	115
A.3 Error Analysis Equations.....	115
A.4 Error Analysis Graphs	116
B SILICON 29 NMR STUDY OF SILSESQUIOXANES.....	119
B.1 Introduction and Methodology.....	119
B.2 Si-29 NMR Spectra.....	119
C STUDY OF POLYSILSEQUIOXANES	126
D MEASUREMENTS OF EPOXY SAMPLES	128
LIST OF REFERENCES.....	137
BIOGRAPHICAL SKETCH	145

LIST OF TABLES

<u>Table</u>	<u>page</u>
2-1. Fractal Dimensional Increment for Common Families of Materials.....	17
3-1. GPC and MALDI Molecular Weights of Silsesquioxanes from Tecklenburg.....	37
4-1. Modulus and Percent Error of Epoxy Resins at Different Strain Rates	46
4-2. Student’s t-test Results of Modulus of Different Strain Rates	48
4-3. Failure Stress of Epoxy Resin at Different Strain Rates	49
4-4. Student’s t-test of Failure Stress of Epoxy Resins	49
4-5. Toughness of Epon 825 with 8ph DETA (MPa*m ^{1/2}).....	52
4-6. Toughness of Epon 825 with 10phr DETA (MPa*m ^{1/2})	52
4-7. Average Critical Crack Size for Epoxy Resins (µm)	54
4-8. Fractal Dimensional Increment by Flaw to Mirror Size for Epoxy Resins	62
4-9. Student’s T-test of Fractal Dimensional Increment of Epoxy Resins	63
4-10. Hand Measurements of Fractal Dimension	71
4-11. Hand Calculations of Fractal Dimension of Epoxy Resins	72
4-12. D* of Epoxy Resins Calculated With Image Pro	73
4-13. Comparison of Fractal Dimensional Increment D* Values for Different Methods.....	74
4-14. Calculated a ₀ values (µm) for Epoxy Resins.....	75
4-15. a ₀ Values (µm) calculated from the Slope of the Fractal Dimension vs. Toughness Plot	77
4-16. Cumulative Error Values for a ₀ Calculations for Epoxy Resins	78
4-17. Calculated a ₀ Values and Associated Error	79
5-1. Usage of Common Polysilsesquioxanes.....	83

5-2. Synthesized Polysilsesquioxanes and Structures.....	85
5-3. Total Hydroxide Content of Silsesquioxanes	95
5-4. Hydroxide Content of Trimethylsilylated Silsesquioxanes	97
5-5. Ratio of Network to Cage Structure of Silsesquioxanes from FTIR.....	100
6-1. a_0 and Error Values for Epoxy Resins by Strain Rate	110
C-1. Crosslinked Silsesquioxane Compositions	126
D-1. Modulus Values for Epoxy Samples	128
D-2. Failure Stress Values for Epoxy Samples.....	129
D-3. Flaw Size and Toughness Measurements for Epon 825 with 8phr DETA Strained at 0.1 mm/min	129
D-4. Flaw Size and Toughness Measurements for Epon 825 with 8phr DETA Strained at 10 mm/min	129
D-5. Flaw Size and Toughness Measurements for Epon 825 with 8phr DETA Strained at 100 mm/min	130
D-6. Flaw Size and Toughness Measurements for Epon 825 with 10phr DETA Strained at 0.1 mm/min	130
D-7. Flaw Size and Toughness Measurements for Epon 825 with 10phr DETA Strained at 10 mm/min	130
D-8. Flaw Size and Toughness Measurements for Epon 825 with 10phr DETA Strained at 100 mm/min	131
D-9. Mirror Measurements for Epon 825 with 8phr DETA Strained at 0.1mm/min	131
D-10. Mirror Measurements for Epon 825 with 8phr DETA Strained at 10mm/min	131
D-11. Mirror Measurements for Epon 825 with 8phr DETA Strained at 100mm/min	132
D-12. Mirror Measurements for Epon 825 with 10phr DETA Strained at 0.1mm/min	132
D-13. Mirror Measurements for Epon 825 with 10phr DETA Strained at 10mm/min	132
D-14. Mirror Measurements for Epon 825 with 8phr DETA Strained at 100mm/min	133
D-15. Image Pro Measurements for Fractal Dimensional Increment by Sample	133

LIST OF FIGURES

<u>Figure</u>	<u>page</u>
1-1. Mandelbrot Set, Generated with Fractal Explorer 2.02.....	3
1-2. Chemical Structure of Epoxy Resin Monomer and Crosslinking Agent.....	5
2-1. Koch Curve, Five Iterations. Generated with Fractal Explorer 2.02.....	8
2-2. IFS Fractal of Fern Leaf. Generated with Fractal Explorer 2.02.....	9
2-3. Perimeters of Nations by Richardson.....	11
2-4. Relationship of D^* to Mechanical Toughness.....	17
3-1. Polymerization Reactions between Epoxides and Amines.....	21
3-2. Schematic of an AFM Tip on Epoxy Surface.....	27
3-3. AFM of Fracture Surface.....	27
3-4. TEM of Epoxy Fracture Surface.	27
3-5. Fractal Structure of Fracture Surface of Epoxy.....	30
3-6. MALDI Molecular Weights of Silsesquioxane Fractions	37
4-1. Stress-Strain Curves of Epon 825 with 8 phr DETA)	47
4-2. Stress-Strain Curves of Epon 825 with 10 phr DETA.....	47
4-3. Example Critical Crack Size Produced through Slow Crack Growth.....	50
4-4. Flaw Size of Epon 825 with 8phr DETA at 100mm/min Strain Rate	50
4-5. Flaw Size of Epon 825 with 10 phr DETA strained at 10mm/min	51
4-6. Ln-Ln plot of Strain Rate vs. K_{Ic} for Epon 825 Resins	53
4-7. SEM Micrograph of Epon 825 with 8 phr DETA	56
4-8. SEM Micrograph of Epon 825 with 10 phr DETA	56
4-9. EDS Spectra of Epoxy Stained with Iodine for 5 minutes	59
4-10. EDS SEM Image of Iodine (Red) Stained Epoxy Surface	59
4-11. Flaw Size and Mirror for Epon 825 with 8 phr DETA strained at 0.1 mm/min.....	62
4-12. Fractal Dimension vs Toughness for Epoxy Resins.....	64

4-13. Slit-Island Method from Hill	65
4-14. 3-D Composite Image of Specimen.....	67
4-15. 2-D Image of Specimen.....	67
4-16. 0-50 Elevation Image Section.....	68
4-17. 0-100 Elevation Image Section.....	68
4-18. 0-150 Elevation Image Section.....	69
4-19. 50-255 Elevation Image Section.....	69
4-20. Magnification of Fracture Surface.....	70
4-21. Richardson Plot of Perimeter of Fracture Surface.....	71
4-22. Square Root of Fractal Dimension vs. Toughness Calculated by Hand from Slit Island Contours.....	72
4-23. Square Root of Fractal Dimension vs. Toughness Calculated by Image Pro from Slit Island Contours	74
4-24. Comparison of Fractal Dimension Increment to Toughness for Three Different Techniques of Measuring	77
5-1. Comparison of Silicone and Polysilsesquioxane Structures.....	82
5-2. Common Polysilsesquioxane Structures	83
5-3. Substrate Configurations.	86
5-4. Schematic of Ubbelohde Viscometer	87
5-5. Viscosity of Polymethylsilsesquioxane	89
5-6. Bruker Avance 600 Mhz Vertical Bore Spectrometer at MBI	94
5-7. NMR Spectra of Synthesized Silsesquioxanes	95
5-8. Bis(Trimethylsilyl)Acetamide Structure (BTMSAA)	96
5-9. NMR Spectra of Trimethylsilylated Silsesquioxanes.....	97
5-10. Total, Reactive, and Non-reactive Hydroxide Content of Silsesquioxanes	98
5-11. FTIR Spectra of Synthesized Silsesquioxanes	100

5-12. Polymethylsilsesquioxane Microstructure.....	103
5-13. Polyethylsilsesquioxane Microstructure.....	103
5-14. Polypropylsilsesquioxane Microstructure	104
5-15. Polybutylsilsesquioxane Microstructure.....	104
5-16. Polymethylsilsesquioxane Cluster Structure	105
5-17. Highlighted Two-Phase Image of Polypropylsilsesquioxane.....	105
5-18. Cao-Baney Route Polymethylsilsesquioxane.....	106
A-1. Effect of Variables on a_0	117
A-2. Effect of Variables on Error of a_0	118
B-1. Polymethylsilsesquioxane.....	120
B-2. Derivitized Polymethylsilsesquioxane.....	120
B-3. Polyethylsilsesquioxane.....	121
B-4. Derivitized Polyethylsilsesquioxane.....	121
B-5. Polypropylsilsesquioxane	122
B-6. Derivitized Polypropylsilsesquioxane	122
B-7. Polybutylsilsesquioxane.....	123
B-8. Derivitized Polybutylsilsesquioxane.....	123
B-9. Polyvinylsilsesquioxane.....	124
B-10. Derivitized Polyvinylsilsesquioxane.....	124
B-11. Polychloropropylsilsesquioxane	125
B-12. Derivitized Polychloropropylsilsesquioxane	125
D-1. Flaw Size of Epon 825 with 8phr DETA Strained at 0.1 mm/min.....	133
D-2. Flaw Size of Epon 825 with 8phr DETA Strained at 10 mm/min.....	134
D-3. Flaw Size of Epon 825 with 8phr DETA Strained at 100 mm/min.....	134
D-4. Flaw Size of Epon 825 with 8phr DETA Strained at 100 mm/min.....	134

D-5. Flaw Size of Epon 825 with 10phr DETA Strained at 10 mm/min.....135

D-6. Flaw Size of Epon 825 with 10phr DETA Strained at 100 mm/min.....135

Abstract of Dissertation Presented to the Graduate School
of the University of Florida in Partial Fulfillment of the
Requirements for the Degree of Doctor of Philosophy

AN INVESTIGATION OF THE NODULAR MICROSTRUCTURE OF SELECTED
SILSESQUIOXANE AND EPOXY THERMOSETTING RESINS

By

Kyle Kathan

December, 2005

Chair: Ronald H. Baney

Major Department: Materials Science and Engineering

The role of the nodular microstructure in the failure of thermosetting resins is unknown. The goal of the research presented here is to determine the mechanisms by which the nodular microstructure affects failure of thermosetting resins.

Epoxy samples were fractured in tension and characterized for fractal dimension, nodular size, and toughness. Samples of epoxy resins have been shown in this work to have a relationship between nodular size and toughness. Two compositions were chosen to study the effect of strain rate and nodule size on toughness and a structural parameter, a_0 . Additionally fractal dimensional increment was measured using two separate techniques, Flaw to Mirror ratio (F-M), and Slit-Island contours. The fractal dimensional increment for slit-island contours was calculated using two similar algorithms; by hand, and with the aid of software.

It was shown through the course of this work that nodule size does not directly relate to toughness. Additionally, it was also shown that the epoxy resins characterized

for this research are not structurally homogenous. It is believed that the inhomogeneities in the structure can be related to a_0 .

Silsesquioxanes were synthesized using a novel two phase reaction. Samples were characterized for molecular weight and structure using matrix assisted laser desorption and ionization (MALDI) and silicon-29 nuclear magnetic resonance (Si-29 NMR). Additionally samples were characterized during growth using an Ubbelohde viscometer to characterize the growth processes of the two phase reaction. It was found that as the temperature of the growth phase synthesis increases, the viscosity of the polymer decreases; this is contrary to what one would normally expect in polymer condensation reactions. This result is due to immiscible two phase nature of the reaction process.

Additional experiments were performed to inquire about the role of the organic group on nodular size. It was hypothesized that nodule size is dependent on the difference in surface energy between the nodule and the free energy of the solution. Organically different silsesquioxanes and different solvents were used to investigate this hypothesis.

CHAPTER 1 INTRODUCTION AND OVERVIEW OF CHAPTERS

1.1 Research Introduction

Thermosetting resins are polymeric materials that react or cure with the addition of heat or energy. Thermosetting resins are generally very brittle and do not melt after curing. Research has indicated that some thermosetting resins such as epoxies and silsesquioxanes do not have homogenous microstructures, as once thought.

Epoxies and other thermosetting resins have been shown to have a nodular microstructure. (Duchet et al. 2003) A nodular microstructure can be loosely described as one containing spherical features of uniform size in a randomly packed order. Nodules can range from tens of nanometers to a few micrometers, depending on the system investigated and the processing used in synthesis. It is of interest to understand how nodules influence the toughness and mechanical properties of epoxies and other thermosetting resins. Previous research has indicated that there is a possible correlation between nodular size and ultimate mechanical properties. (Baney et al. 1999) Using conventional thought, it is not entirely obvious as to what role nodular size plays in the toughness of thermoset resins. By applying a new philosophy of failure in brittle materials, this dissertation research has sought to find a better understanding of how nodules affect toughness.

Epoxies and other thermosets are unique in that they can be considered a hybrid between ceramics and plastics. They are polymeric in nature and have a low modulus compared to ceramics, yet they fail in a brittle manner, similar to glasses and crystalline

materials. Recently, researchers have shown that the toughness of brittle materials can be linked to a structural parameter, a_0 , by relating the fracture surface of a specimen to a fractal model. The WMP theory, developed by West, Mecholsky and Passoja, (Mecholsky et al. 2002), indicates that toughness of a brittle material can be determined from the following equation:

$$(1) K_{Ic} = E(a_0 D^*)^{1/2}$$

wherein K_{Ic} is the toughness, E is Young's Modulus, a_0 is a structural parameter, and D^* is the fractal dimensional increment.

This theorem will be reviewed in depth in Chapter 2. It was my hypothesis that this work could show a clear relationship between the nodular size and the structural parameter a_0 . Ideally this work would be used as a guide to help better understand what microstructural factors alter the toughness of thermosetting resins. By understanding exactly how nodule size affects the toughness of an epoxy, it should be possible to engineer a system with increased toughness. Additionally this work would serve to increase the body of knowledge to which the WMP theory has been applied.

1.2 Fractal Basics

Fractals are a class of complex geometric structures that are similar on all length scales. In other words, fractals show essentially the same structural features, regardless of magnification. While often very complex, fractals can often be described very simply. On the most fundamental level all fractals can be described using three terms, the initiator, the generator, and the rule. Basically the initiator is the structure that starts off a fractal, the generator is the change in the initiator with each successive iteration, and the rule is how the generator is applied to the initiator. Additionally, fractals can also be characterized by their non integer dimension, D . Fractals are not like normal geometric

structures. A simple geometric structure would have a topological dimension of 2 if it was a flat surface or 1 if it was a line. Fractals however, have dimensions greater than their topological dimension. An example would be the surface of an orange. Ideally one would say the surface area is equivalent to $4\pi r^2$ where the exponent, 2, is the topological dimension for a surface. However, upon closer inspection one would see that the surface of an orange is full of pits and valleys and exhibits a very irregular surface. The surface of an orange is in fact fractal and has a surface area equal to $4\pi r^D$, where D is the fractal dimension and is between 2 and 3. The fractal dimensional increment, D^* , as used in the WMP theory, is the decimal portion of the fractal dimension. The fractal dimension can be described as a quantification of the complexity of a given fractal structure and has been used to quantify everything from basic fractals to coastlines of nations. (Richardson 1961)

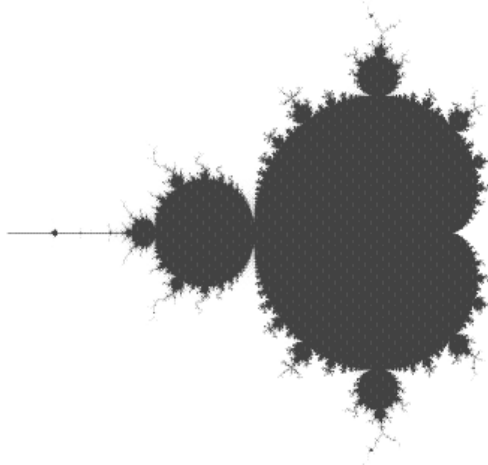


Figure 1-1 Mandelbrot Set, Generated with Fractal Explorer 2.02

Fractals have been applied to everything from art to science. Figure 1-1 is an example of a common fractal known as the Mandelbrot Set and was generated with Fractal Explorer 2.02. (Arthur 2005) Recent research has used fractals as a method of

quantifying the nature of brittle fracture in materials. It has long been established that the fracture surface of a material is self similar, which is much like a fractal. A great deal of research has been conducted defining the fracture surface in fractal terms. Researchers have applied fractal basics to fracture to determine the relationship of microstructure on toughness. (Borodich 1997; Borodich 1999) Current research into application of fractals to fracture toughness has focused on glasses and crystalline materials. In previous work it has been demonstrated that fractal dimension and toughness of a material are related by the structural parameter, a_0 . (West et al. 1999; Mecholsky et al. 2002) Values for a_0 are typically on the order of lattice parameters. This present work endeavors to expand on current knowledge by seeking out materials which should have a larger value of a_0 . For the purpose of this work, nodular materials have been investigated under the assumption that a_0 will be a function of the nodular size. Two separate materials have been investigated, epoxy and silsesquioxanes.

1.3 Materials Overview

Epoxy materials were originally thought to be homogenous. However work in the late 1970's and early 1980's, primarily by Koutsky and associates, demonstrated that epoxies are not homogenous. It was reported that epoxies have a nodular microstructure, in which the nodular size is very uniform and closely packed together. (Racich et al. 1976) Additionally, it was found that the size of nodules depends on the amount of crosslinking catalyst used and the curing schedule employed. (Mijovic et al. 1979) Also of note, it was found that the mechanical properties of said systems are dependent on nodular size. (Mijovic et al. 1979) Figure 1-2 is the chemical structure of the monomers employed in this research.

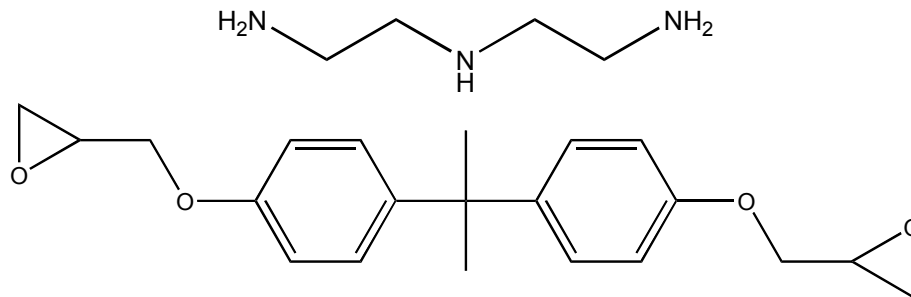


Figure 1-2. Chemical Structure of Epoxy Resin Monomer and Crosslinking Agent.

Top: Diethylenetriamine, Crosslinking Agent

Bottom: Diglycidyl Ethers Bisphenol-A (DGEBA), Epoxy Resin Monomer

Silsesquioxanes are a technologically important inorganic polymers. (Baney et al. 1995) Most work with silsesquioxanes has focused on developing materials to be applied to integrated circuits as a low-k dielectric interconnect layer. Silsesquioxanes are also used as fillers and thin films in other applications. Traditionally, silsesquioxanes are synthesized through a direct condensation reaction from chlorosilanes and water and generally have the chemical formula $\text{RSiO}_{3/2}$ where R is virtually any organic group. Depending on the nature of silsesquioxane monomer, many possible structures can be formed. Most commonly investigated silsesquioxanes have been reported to be a large network polymer, although ladders and polyhedral structures can also be found. These structures will be covered in Chapter 3. (Baney et al. 1995) Work presented here will focus on a novel process for synthesizing silsesquioxane polymers using two immiscible phases. (Kondo et al. 2000) It is postulated that hydrogen bonding organic solvents can be used to guide and control the structure by hydrogen bonding to the silanol groups of the growing polymer. In effect, this drives the polymer into the organic phase where

condensation reactions are slowed greatly, and the formation of small cage structures such as the cubical octomer is retarded.

1.4 Chapter Outline

Chapter 2 begins a critical review of the applications of fractals to fracture mechanics. An overall view of fractals and their applications in science is presented to illustrate the relevance to this work. This chapter includes a detailed review of the topical literature. Chapter 3 is a review of the materials used in this research. This incorporates topics ranging from characterizing nodularity in epoxies to the synthesis and characterization of silsesquioxanes. Chapter 4 highlights the relationship between nodular microstructure and toughness of epoxy resins. High purity diglycidyl ethers of bisphenol-A, DEGBA, (Epon 825) were cross-linked using diethylenetriamine (DETA). After samples were cured, tensile testing was performed at a variety of strain rates and test conditions. Chapter 5 focuses on the two-phase process for synthesizing silsesquioxanes. Viscosity studies were conducted to comprehend the nature of growth of the silsesquioxane polymers. Additionally, NMR was conducted to better understand the effects of the organic group on structure of the polymer. Finally, samples were cross-linked using tin octoate, a common catalyst in this technology, and different solvents to investigate the effects of solvent/polymer interaction on nodular growth. Additionally an appendix was prepared to discuss error analysis of the WMP theory.

CHAPTER 2 FRACTALS AND FRACTURE

2.1 Introduction to Fractals

The term fractal was coined by Mandelbrot to describe a set of objects with seemingly infinite detail. (Mandelbrot 1977) Fractals are complex geometric structures that can be related to many scientific and natural phenomena. Fractals are self-similar or self affine and scale invariant. Self-similar structures are the same in all directions in all magnifications. Self-affine structures very similar to self-similar, but differ in one scale in one direction. Scale invariant means that no matter what magnification or scale a fractal is being viewed at, the structure is for all intents and purposes the same. Visually fractals can look extremely complex; however they are often very simply described. Fractals are often said to possess an infinite level of detail, but are often generated by a simple iterative process.

All mathematical fractals can be described by three terms; initiator, generator, and rule. The initiator is the starting structure from which a fractal will be formed. The generator is how the structure changes with each successive step. The rule describes how the generator is applied to the structure. Figure 2-1 is an example of the Koch curve. The initiator in this case is a straight line; the generator is formed by two lines of equal length that connect at a 60 degree angle. The rule for the Koch curve states that each straight length of the curve is broken into three separate segments of equal length and the middle segment is replaced with the generator. The generator is scaled to the length of the segment it is replacing.

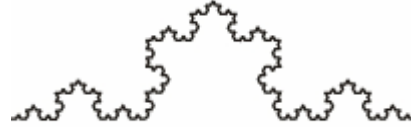


Figure 2-1. Koch Curve, Five Iterations. Generated with Fractal Explorer 2.02

Self-similar objects are ones that have been said to be invariant of scale. Self-affine objects are very similar to self-similar fractals, but are scaled differently in one dimension, x , y , or z . Fracture surfaces are considered self-affine because the perturbations which form the features of the fracture surface are the same from one region to another but are scaled differently. (Mecholsky et al. 2002)

2.2 Fractals in Nature

Fractal structures are commonly found in nature. Everything from trees and plant life to clouds and weather patterns to the distribution of stars and gasses in the cosmos can be described using fractals. (Bailey et al. 2004; Falgarone et al. 2004) Commonly, geological structures are defined using fractals. (Volland et al. 2004) Properties such as coastlines and erosion have been related to fractals. (Turcotte 1992; Carpinteri et al. 2004) Figure 2-2 is an example of an Iterative Functional System (IFS) fractal generated with Fractal Explorer Software. Figure 2-2 is auspiciously similar to a fern leaf and is an example of how natural structures can often be described with fractals.

Over the past two decades or so, fractals have been used extensively to characterize natural phenomenon. Researchers have looked extensively at applying fractal theories to failure, diffusion, and spread of disease and many more fields of research. Additionally, chaos theory has used fractals to mathematically describe the apparent random nature of the universe. (Gleick 1998)



Figure 2-2 IFS Fractal of Fern Leaf. Generated with Fractal Explorer 2.02

2.3 Fractal Dimension

In Mandelbrot's famous treatise the question was asked, how long is the coast of England? (Mandelbrot 1967) How long is the perimeter of any country? How long is the Koch Curve for that matter? A simple question on the surface, but depending on what scale is employed, the length is essentially infinite. The Koch curve begins as a straight line of a defined length from which a fractal is formed. The problem becomes what size ruler does one use to measure the length of the Koch curve? A smaller ruler will give a larger length because as one measures along the curve, the smaller ruler will see the smaller features that a larger ruler would not. An answer to Mandelbrot's question is that the length of the coast of England is relative, being determined by the person measuring it and the measuring stick they are using. Euclidean structures such as lines, disks, and spheres have dimensions of 1, 2, and 3 respectively; however fractals are not so simple. Effectively, fractals are non-Euclidean, as such the dimension must be different than in Euclidean geometry. For Euclidean geometry, the dimension of a line is 1, but in fractals, the dimension is a non-integer number.

The Hausdorff or fractal dimension is often used to characterize a fractal. The Hausdorff dimension is a measure of the number of repeated features in a structure with a decrease in scale or an application of an iteration of the generator to the initiator. The Hausdorff dimension can be derived from equation 2-1:

$$(2-1) N = \frac{C}{r^D}$$

Where N is the number of objects, r is the level of reduction and D is the Hausdorff or fractal dimension.

A relevant example would be the dimension of the Koch Curve. Upon inspection one would see there are 3 pieces to the Koch Curve, after applying an iteration, the middle piece is replaced with 2 new pieces making 4 pieces total. The fractal dimension of the Koch curve is 1.26. The fractal dimension can be thought of as a quantification of the tortuosity of a fractal. The fractal dimension is the unifying value for which structures or phenomena are characterized and related to a desired property.

Lewis Fry Richardson established that there is a linear relationship between the measured perimeter of a country and the length of the rule used to measure. (Richardson 1961) Figure 2-3 is a representation of Richardson's work. Richardson's work was originally intended to explain why nations of Europe went to war by comparing the differences reported by two nations in the length of their shared border. Richardson's work was later adapted for use in materials science and mathematics.

The Richardson method measures the perimeter of a complex object or fractal using different ruler lengths. As ruler length decreases, overall perimeter increases. This is because smaller rulers identify small features on the perimeter that a larger ruler

would not see. Richardson showed that the log of the ruler length versus the log of the perimeter gives a linear relationship. The Richardson equation is given by equation 2-2

$$(2-2) L(s) = s^D + c$$

Where s is the length, D is the fractal dimension and c is a constant

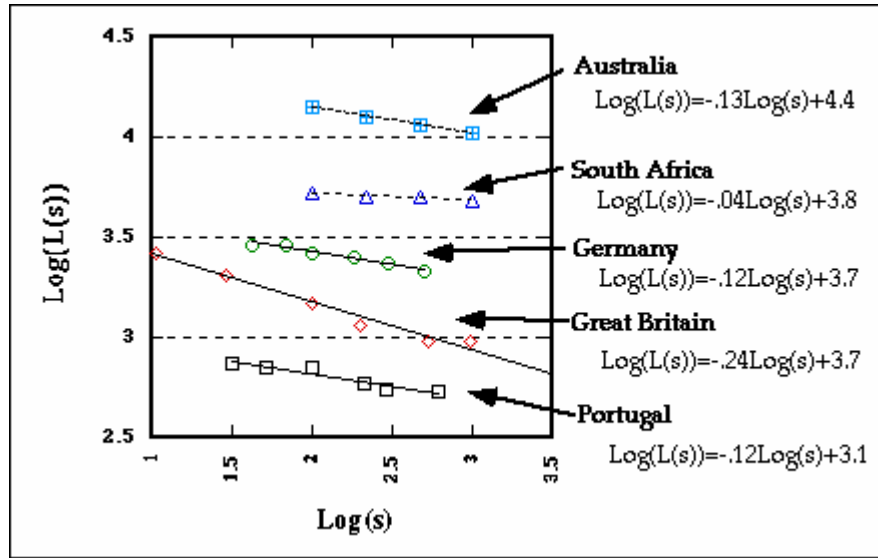


Figure 2-3 Perimeters of Nations by Richardson (Richardson 1961)

Later Mandelbrot would identify the slope of the Richardson work to be equivalent to $1-D$ where D is the fractal dimension. It should be noted that in this work the fractal dimension is between 1 and 2. For a line the fractal dimension is between 1 and 2, for a surface, the dimension is between 2 and 3. (Borodich 1999) Rulers were used in the case of Richardson's work; to calculate the fractal dimension of surfaces and bodies, a dimension appropriate measuring device must be used such as squares for surfaces.

The fractal dimension is a measure of the tortuosity of a fractal. (Chen et al. 1993) Commonly the fractal dimensional increment is reported. The fractal dimensional increment or D^* is the decimal portion of the fractal dimension. Fractal dimensional increment is reported to show correlation between different techniques. As previously

mentioned a line fractal has a dimension between 1 and 2, and a surface between 2 and 3. Fractal dimensional increment can allow one to compare line and surface fractals.

In recent years the fractal dimensional of a fracture surface has been related to the mechanical properties of a material. (Mandelbrot et al. 1984) As such it has become important to determine methods to measure the fractal dimension of a fracture surface. There are many different techniques for measuring the fractal dimension.

Mandelbrot pioneered the use of fractal dimension as a descriptive tool in analyzing fracture surfaces. It has been shown extensively that fracture surfaces for brittle and ductile materials are fractal. Many research groups have attempted to relate fractal dimension to mechanical properties. (Mecholsky et al. 1991; Chen et al. 1997; Charkaluk et al. 1998) There is some disagreement as to the relationship between fractal dimension and mechanical toughness. Bigerelle has attributed this disagreement to the different methods used to measure fractal dimension. (Bigerelle et al. 2004) Many different techniques have been used to measure fractal dimension; slit-island, vertical section, box counting, and projected area. These are just a few of the techniques that have been reported in the literature, each of these methods can result in a different fractal dimension for the same fracture surface.

Hill has reported a protocol for measuring fractal dimension using coast lines of polished fracture surfaces set in epoxy. (Hill et al. 2001) Further work of Hill and Della Bona using the same technique indicated that fractal dimension is dependent on the contour angle of the sample. (Della Bona et al. 2001). The protocol described by Hill can be called a slit-island method, which was first described by Mandelbrot. (Mandelbrot et al. 1984) Samples are set into epoxy and polished down until islands appear. The islands

are formed by removing the top of a rough section on the fracture surface. The perimeter of the islands is measured using several different ruler lengths in a fashion in accordance with the Richardson method.

The slit-island technique has been used extensively in the literature as a method of measuring fractal dimension for comparison to fracture properties. Bigerelle has laid out certain criteria that the concept of slit island was deduced from: (Bigerelle et al. 2004)

(i) When islands are derived from initial self-affine fractal surface of dimension D_s by sectioning with a plane, their coastlines are self-similar fractals with dimension $D = D_s - 1$.

(ii) The relation between perimeter and area is given by the equation:

$$(2-2) R(\eta) = \frac{[P(\eta)]^{1/D}}{\sqrt{A(\eta)}}$$

where $R(\eta)$ is a constant which depends on the choice of the yardstick length, h , used to measure the length along the walking path. This equation is only true for self-similar whose perimeter and area are measured in the same way.

(iii) When the graph of $\log(P)$ versus $\log(A)$ is rectilinear, the fractal dimension is deduced from the slope.

Bigerelle further finds that the slit-island method can be a statistically significant measure of the fractal dimension with proper choice of ordinates and abscissa. Additionally it was also shown that the slit-island method can produce artifacts when correlating the fractal dimension of a surface to a particular physical process or testing parameter.

It was additionally reported by Hill that fractal dimension was dependent on the technique employed. It was found that the slit-island technique gave fractal dimensional increment values between 0.08 and 0.28. The vertical profile technique and indentation technique also reported resulting in much lower values.

The slit-island techniques such as that reported by Hill, produce dimensions between 1 and 2. This method gives an approximation to the true fractal surface. Although generally accepted, these values are not true fractal dimensions for the surface. A surface fractal should have a dimension between two and three. Joseph and associates used atomic force microscopy to generate a three dimensional image of a fracture surface of epoxy samples. (Joseph et al. 1998) The values found by AFM are between 2 and 3 and can be considered to be the true fractal dimension of a surface. The drawback of AFM is that only very small regions are measured, generally less than $100 \mu\text{m}^2$. Conversely, the work of Xie used laser profilometry to generate a 3-D map over very large samples, several millimeters on a side. (Xie et al. 1998)

The algorithm used by the AFM in the work of Joseph uses a technique similar to the Richardson method for calculating dimension of a line. The AFM uses progressively smaller cubes to measure the volume. Conversely the Richardson method uses progressively smaller lines to measure a perimeter. The technique reported by Xie uses a projective covering method where the fracture surface is broken up into progressively smaller squares. The surface area of the fracture surface is found by measuring the surface area of the portion of the fracture surface projected in the square. The projective covering method has found much more use in the literature than AFM. (Stach et al. 2001; Stach et al. 2003; Stach et al. 2003; Stemp et al. 2003). It should be noted that samples characterized using surface projection techniques are often considered to be multifractal. A surface is considered multifractal if there are multiple fractal dimensions depending on scale length.

Dubac reported a technique for measuring fractal dimension using vertical profiles of fracture surfaces. The profile is laid against several grids of squares of different sizes. The number of squares for each size used to cover the entire trace of the profile is used to calculate the fractal dimension. (Dubuc et al. 1989) Hill has reported that using vertical profiles gives vastly different results than the slit-island technique. (Hill et al. 2001) Stach has argued that part of the discrepancy of profile techniques is that the amount of surface characterized is very low and can not be descriptive of the entire surface, especially for surfaces that are multifractal or self-affine. (Stach et al. 2003)

There is currently no standard method for measuring fractal dimension of a surface. In general the technique used to measure fractal dimension is dependent on the author's preference. Due to the disparity in techniques and thus dimension of measured surfaces, there is some debate in regards to the relationship of fractal dimension to mechanical properties of material.

2.4 Mechanical Properties

Fractal analysis has been used extensively in materials science to relate the geometry of the fracture surface to mechanical properties. (Mecholsky et al. 1991; Lyu et al. 1994; Balankin 1995; Charkaluk et al. 1998; Su et al. 2000; Issa et al. 2003) Many different properties of materials have been related to fractal dimension, including impact energy, fracture toughness, and crack propagation. (Bigerelle et al. 2004) The wide range of fractal dimension values, as measured using different techniques, has led some researchers to believe that fractal dimension is merely a universal value or parameter that has no correlation to mechanical properties. Some further argue that fractal dimension is a measure of the amount of plastic deformation associated with failure of a specimen.

Experimental data has indicated that there is a relationship between mechanical properties and fractal structures. (Borodich 1999) Researchers have related the parameter fractal dimension to the toughness and fracture surface of brittle and ductile materials. (Mandelbrot et al. 1984; West et al. 1999; Stach et al. 2001). Mandelbrot's early work pioneered the study of fractals on fracture surfaces. West et al. have shown that surface energy of formation of a fracture surface for brittle materials is directly related to the fractal dimensional increment of a surface. (West et al. 1999) This relationship is given by equation 2-3.

$$(2-3) \gamma = \frac{1}{2} E a_0 D^*$$

Where γ is the surface energy of formation, E is Young's modulus, a_0 is a structural parameter and D^* is the fractal dimensional increment.

Often fracture surfaces and fractals are quantified for the fractal dimension. Mecholsky has shown there to be a roughly linear relationship between fractal dimension and toughness for materials of the same family (glasses, ceramics, and crystals). (Hill et al. 2000) Figure 2-4 is a graph plotting the results of Mecholsky.

Table 2-1 is a table of fractal dimensional increment for common materials from West. (West et al. 1999) It should be noted that on small scales, fracture surfaces are purely fractal. However it has been reported that the disorder of long range structures gives rise to multifractal surfaces. (Xie et al. 1998; Xie et al. 1999; Babadagli et al. 2001; Stach et al. 2001; Carpinteri et al. 2002; Carpinteri et al. 2003; Stach et al. 2003; Stach et al. 2003) Multifractal surfaces are ones where there are more than one fractal dimensions for the same surface.

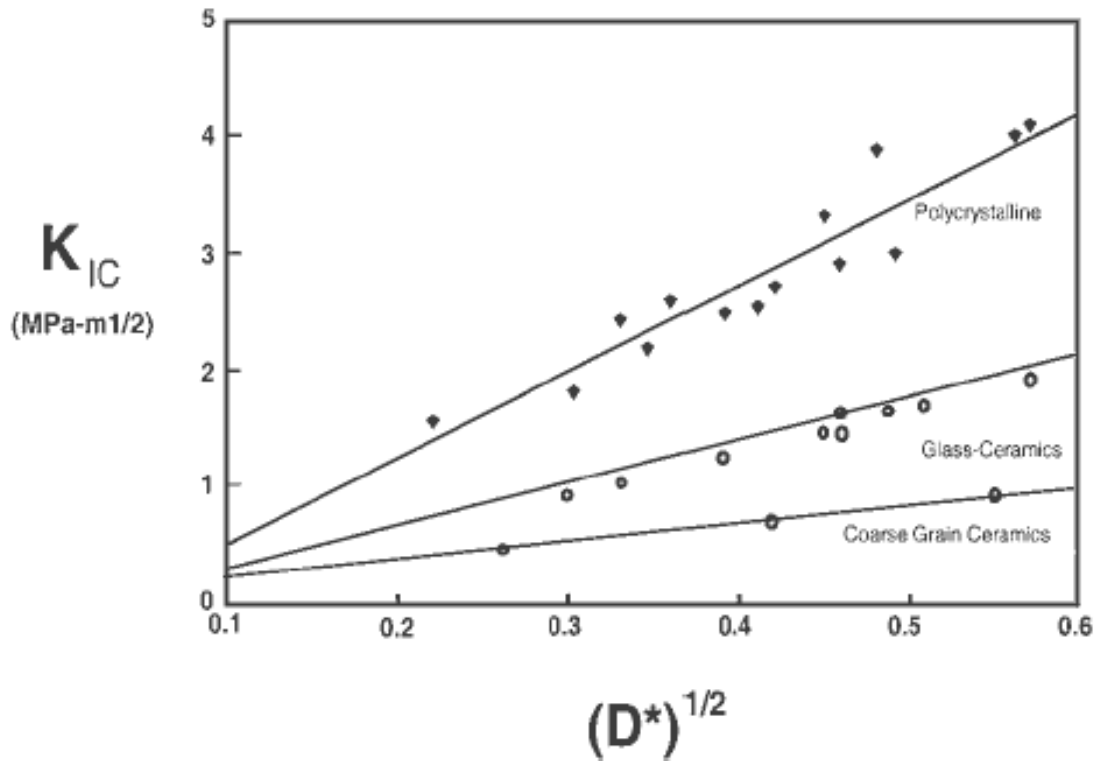


Figure 2-4 Relationship of D^* to Mechanical Toughness(Hill et al. 2000)

Table 2-1 Fractal Dimensional Increment for Common Families of Materials

Class	D^*
Single Crystals	0.07-0.12
Glasses	0.007-0.1
Glass-ceramics	0.06-0.3
Polycrystalline ceramics	0.06-0.35
Polymers	0.2-0.29

(West et al. 1999)

The fracture surface of a material can be viewed as being composed of perturbations that are deviations from a flat plane. These perturbations are formed by constructive and destructive addition of breaking atomic bonds along the crack plane. It has been shown by several research groups that fractal dimensional increment can be related to surface energy of a fracture surface and toughness. (Mandelbrot et al. 1984;

Issa et al. 2003) The toughness of a material can be related to fractal dimensional increment through the following equation:

$$(2-4) K_{Ic} = E(D^* a_0)^{1/2}$$

Where E is the Young's Modulus, D^* is the fractal dimensional increment, K_{Ic} is the plane strain mechanical toughness, and a_0 is a structural parameter.

The parameter a_0 has been extensively investigated by West, Mecholsky, and Passoja. (Mecholsky et al. 2002) They report the use of molecular dynamic calculations to calculate the fractal dimension of silica glasses and silicon crystals. They report that a_0 is a measure of the free volume that is formed by breaking bonds at the crack tip. Therefore a_0 can be described as the initiator of the fractal to the D^* generator.

Using the West Mecholsky Passoja Theory one can relate the fractal dimensional increment directly to the toughness of a material. However a_0 can not be directly measured and must be calculated from other measurements. It is of interest to understand the processing parameters that affect a_0 ; if one were able to control a_0 , one should be able to control toughness.

2.5 Conclusions

Fractals are complex geometric structures which have been shown to have a major role in nature. Many research groups have used fractals to describe the fracture surface of a material. Additionally there is significant evidence that the fractal dimensional increment is directly related to toughness. West, Mecholsky, and Passoja have shown that toughness can be related to fractal dimension by a structural parameter a_0 .

The fractal dimensional increment is a measure of the fractal nature of a fracture surface. There currently exist several different techniques for measuring fractal

dimensional increment such as slit-island, and projected area. Commonly the slit-island technique is the accepted method of measuring fractal dimensional increment of fracture surfaces.

CHAPTER 3 EPOXIES, SILSESQUIOXANES, AND NODULAR STRUCTURE REVIEW

3.1 Introduction

Two materials of commercial interest were investigated in this dissertation, epoxy resins and silsesquioxane resins. These materials were chosen because of their microstructure and extensive supportive literature. In this chapter a review of the relevant literature in regards to both materials and nodular microstructure.

3.2 Review of Nodular Epoxies

3.2.1 Introduction to Epoxies

Epoxies are organic polymers containing epoxide rings. An epoxide ring is a three member ether ring containing an oxygen and is under strain and thus very reactive. Epoxies are commonly used in composites and structural materials. Additionally epoxies are used as adhesives and electrical insulators. Epoxies are two-part thermosetting resins that require a catalyst to initiate polymerization. The addition of energy and catalyst cure an epoxide resin into a rigid three dimensional structure that does not melt upon reheating.

Frequently, amine or anhydride catalysts are used to crosslink epoxy resins. Figure 3-1 is a figure of common crosslinking reactions between epoxide and amine groups. Due to their complexity the microstructure of epoxy resins is not very well understood. Some groups have claimed that epoxies have a nodular microstructure, while others claim that any asserted proof is purely circumstantial.

this does not explain why the bulk has the same nodule size as the surface. Their work used completely different substrates ranging from copper to various plastics to change the free energy of the surface.

Samples were prepared from Epon 825 resin and Diethylenetriamine. Nodule size was determined using Transmission Electron Microscopy. Koutsky and Racich drew eight distinct conclusions initially quoted below: (Racich et al. 1976)

1. There is a definite nodular formation through the bulk of the epoxy resins studied
2. The nodules have sizes ranging from 10 to 60 nm
3. At times, the nodules appear to align and form networks either at interfaces or in the bulk
4. Nodules are observed to agglomerate into larger supernodules
5. Teflon and silicone rubber contact with epoxy inhibits the appearance of nodules while copper and glass induce large nodules or increase packing density of small nodules
6. No consistent relation has been found among composition or cure, nodule size, and nodule density
7. Slightly cured, soft epoxy resins show what may be interpreted as nodule precursors
8. Some individual nodules surprisingly show a very subtle ridge-like fine structure on both fracture and free surfaces

What is not clear from that work, however, is if it is truly the surface energy of the mold that affects nodule formation, or if another surface phenomenon such as crystal structure or difference in physical properties of the various substrates such as porosity is responsible.

A better study would have been to use silicone molds. The silicone could be easily modified with any one of numerous agents to change the surface energy. Doing this would result in molds or substrates that are similar to one another in terms of structure, porosity and other physical properties, but have different surface energies. To date no one has investigated the effects of surface energy modified silicone molds on nodule size.

Additional experiments by Koutsky and other researchers focused on the impact of chemical composition on nodule size. (Vanlandingham et al. 1999) Results indicate that an increase in cross-linking catalyst results in smaller nodule sizes. This would seem to suggest that nodules form from nucleation events, similar to crystals precipitating from a melt. A higher content of cross-linker would produce more nucleation events in a given volume of resin. The difference between nodules and crystallization is that the nodules seem to all be the same size and shape, and they are connected with a similar material as the nodule itself. However crystallization of a melt can result in a large distribution of grains and irregular shapes. Additionally, the grains impinge upon one another and there is no additional material connecting them together as in the epoxies. It is unclear from this analogy as to why nodules are so perfectly spherical and of constant size. Many of the detractors of the nodule microstructure of epoxies cite the fact that no conclusive proof of a difference between the interstitial material and the nodule, which they believe illustrates that the microscopic evidence for nodules are artifacts of either the imaging system or the manner in which the sample was prepared. (Oberlin et al. 1982; Duchet et al. 2003) Although Pollard confirms this observation by relating the gelation of epoxy to the Avrami theory of phase change. (Pollard et al. 1987) The Avrami theory appears to hold true until at least the gel point of the resin.

Another variable investigated for its influence on nodule size of epoxy resins is the processing parameter. Mijovic and Wu have independently shown that mixing and processing conditions has an effect on nodular size of the final product. (Mijovic et al. 1985; Wu 1991) Epoxy resins are thermosetting and generally need heat to initiate curing. The temperature and length of curing can greatly shape the final properties of a

resin, including the nodule size. Mijovic found that by adjusting the curing schedule, one was able to adjust the presence of nodules. Proper control of curing resulted in a resin with no nodular structure, but a rougher fracture surface.

Wu, on the other hand, studied the consequences of stirring on nodule size. His work found that greater care in stirring resulted in smaller nodule sizes, but the mechanical toughness did not change. This is an interesting result. One could infer from this work that a higher rate of stirring mixes the resin and catalyst better, forming a more homogenous starting material. Using the crystallization analogy from earlier, a more homogenous mixture would result in more nucleation events and thus more nodules. The reasoning as to why the toughness remains the same is that while the microstructure changes the total cross-link density remains the same. From this, one could infer that nodule growth and size is related to the solubility of the nodule in the resin/catalyst solution. (Wu et al. 1985) As nodules grow their solubility decreases, which determines the future growth capacity of nodules.

The exact nature of nodule growth is unknown however. Researchers have related the growth of an epoxy network to a fractal structure. (Kozlov et al. 2004) Fractals are complex geometric structures that are finding tremendous use in characterization of polymerization reactions and growth kinetics. (Schaefer et al. 1986)

3.2.3 Observations of Nodule Size

Many researchers believe that epoxy resins are inhomogeneous and have a nodular microstructure; conversely numerous others believe that the observed structure is merely an artifact. Duchet lists three reasons as to why nodules are not real: (Duchet et al. 2003)

1. Epoxy networks cured with various amine curing agents, having stoichiometric and nonstoichiometric compositions, have been studied. From electron microscopy observations, no correlation between the nodular structure and the crosslinking

density has been obtained. Moreover, etched uncross-linked polymers such as poly(methylmethacrylate) can present a nodular structure similar to that of epoxy networks. Oberlin et al. analyzed more deeply epoxy resin morphology by transmission electron microscopy and found that cured epoxy networks based on DGEBA and diamine were homogeneous and remained stable while under study in a clean vacuum. (Oberlin et al. 1982) However, in a poorer vacuum, electron irradiation etches the sample. Progressively, nodules about 100 nm in size appear. These investigations show that this nodular structure is not linked to inhomogeneous cross-linking, and the authors have ascribed the nodular structure to the interactions of etching agents with the sample surface (linear or crosslinked).

2. Fluctuations in cross-linking densities should be put into evidence by scattering methods. Dusek and coworkers (Dusek et al. 1978) observed no difference between scattering curves realized on linear and amorphous thermoplastics and curves realized on cured epoxy networks. Epoxy-amine networks exhibit only one sharp and well-defined relaxation peak related to the glass-transition temperature (T_g). Therefore, there is no physical proof of structural inhomogeneity.

3. Moreover, if inhomogeneities are formed during the curing process, the kinetics, the evolution of the distribution of i -mers, the gel point conversion, and so forth should be affected. However, these parameters for a nodular structure are quite well described by equations determined by statistical calculation if a single reaction mechanism and quite homogeneous curing are assumed. This perfect agreement is proof of the epoxy network homogeneity.

Many researchers have tried to prove the existence of nodules and investigate the nature of the interstitial or connective material. Most have focused on two separate methods; microscopy such as scanning electron microscopy (SEM) and transmission electron microscopy (TEM), and scattering methods such as Light Scattering and Small-angle X-Ray Scattering (SAXS).

Electron microscopy techniques have often confirmed the existence of nodules. Works of Koutsky and Mijovic have all used SEM and TEM to show conclusively that epoxies have a nodular microstructure. (Mijovic et al. 1977; Mijovic et al. 1979; Mijovic et al. 1979) However, work of Koutsky and Uhlmann using SAXS did not show any structure at the length scale which nodules have been observed. (Matyi et al. 1980) This has led many researchers to believe they are nonexistent and are surface artifacts of

sample processing. Conversely, the work of Gupta argues that the electron beam can etch the surface of epoxy samples and is thus the origin of the nodular structure observed by other groups. (Gupta et al. 1985).

Stevens used Light Scattering to show that as epoxy cures, two phases principally form. Stevens studied two epoxy systems and found different primary phase sizes depending on the system. Because the exact indexes of refraction of the solid and solvent phases were unknown, true size and distribution could not be calculated. It was, however, estimated that the difference in indices in refraction was as low as 1%. One could infer that cross-link density and thus modulus is proportional to index of refraction. Using this, one could further infer that the difference in modulus between nodule and connective material is very low. (Stevens et al. 1982)

Dusek provided an in-depth review of the formation of epoxy networks and potential sources of inhomogeneities. (Dusek 1986) He cited evidence claiming results found in light scattering are due to inhomogeneities of the epoxy resin without any cross-linking catalyst added and are often larger than nodules observed with electron microscopy. Dusek goes on further to state that epoxies are homogenous and not nodular due to the closeness of gel point of a resin to the predicted value, as determined kinetically. Many researchers have used atomic force microscopy (AFM) to study the fracture surfaces of epoxies. AFM is a projection of the surface and does not give exact nuances on the underlying structure. Figure 3-2 is a schematic of an AFM tip on the surface of a nodular material. (Duchet et al. 2003) Figure 3-3 is an AFM image of an epoxy resin as reported by Akari. (Araki et al. 2002). Conversely Figure 3-4 is a TEM image generated by Koutsky of a fracture surface. (Mijovic et al. 1979)

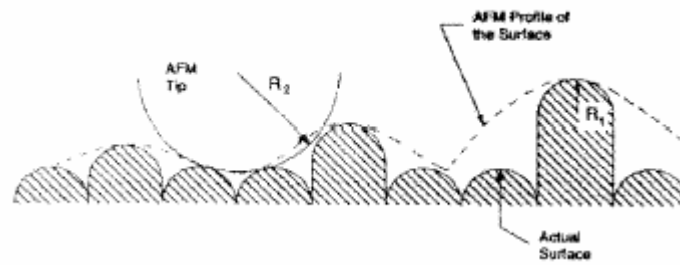


Figure 3-2. Schematic of an AFM Tip on Epoxy Surface. (Duchet et al. 2003)

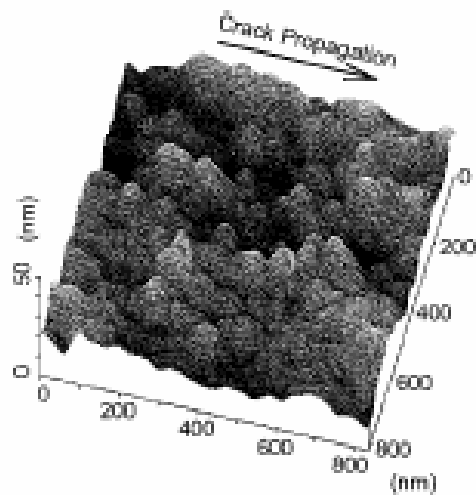


Figure 3-3. AFM of Fracture Surface. (Araki et al. 2002)

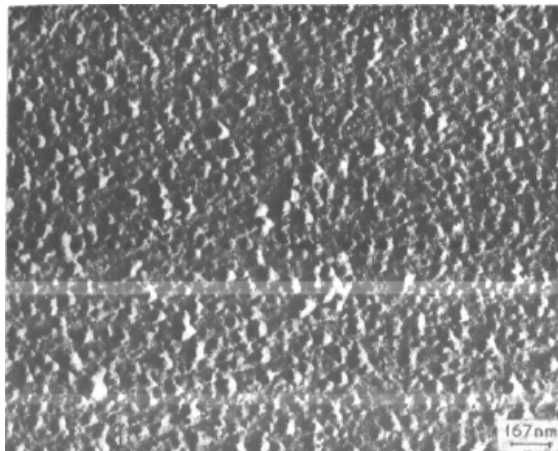


Figure 3-4. TEM of Epoxy Fracture Surface. (Mijovic et al. 1979)

From Figure 3-2 one can see how an AFM can “miss” data as the tip traverses across the surface. By comparing Figure 3-4 to Figure 3-3 one can clearly see nodules in

the surface; however Akari has reported that those are not nodules, but merely a complex surface structure. (Araki et al. 2002) AFM has often been used to disprove the existence of nodular microstructure. With proper preparation of a sample surface and test parameters, it has been shown that AFM can be used to map compositional differences on the surface of a material. Researchers have used these techniques to investigate the surface of epoxy fracture surfaces for differences in modulus between nodule and connective material.

Duchet used AFM to explore the nature of the interstitial material and to measure differences in modulus between the two phases. He reports that the AFM gives a homogenous surface and therefore there are no differences between nodules and interstitial material; this nodules are artifacts of other imaging techniques. (Duchet et al. 2003) Additionally, work by Bai using Small Angle Neutron Scattering (SANS) to investigate cross-link density indicates that the cross-link density is homogenous throughout the structure. (Bai 1985).

The arguments presented by Duchet above are invalid because they assume that the nodule and the connective or interstitial materials are inherently dissimilar. Currently no one has proven conclusively that the nodule and connective material are significantly different from one another. Many of the techniques which can be used to investigate the differences in density or modulus of the two phases may not be sensitive enough to see the differences, if any exist.

3.2.4 Mechanical Properties of Nodular Epoxy Resins

In general, the toughness of epoxy resins is between 0.4 and 1.8 MPa*m^{1/2}. (Plangsammas et al. 1999; Araki et al. 2002) Epoxies are generally thought to be brittle in nature, although at temperatures above the glass transition temperature, there can be

significant plastic deformation at the crack tip. Studies have shown that epoxies age slightly after initial curing and post curing. (Jo et al. 1991) The consequences of aging can result in changes to the mechanical and thermal properties. The nature of the change depends on how close the formulation is to the stoichiometric ratio.

Many works have observed that a failure crack in an epoxy resin propagates through the connective material as opposed to through the nodule. (Mijovic et al. 1981; Woo et al. 1991; Wu 1991; Vanlandingham et al. 1999). It is unclear, however, how nodules affect toughness. It has been shown that samples with the same glass transition temperature (T_g) but different nodule sizes have the same toughness. This indicates that it is the cross-link density, (which is proportional to T_g) that is the determining factor of toughness not the nodule size. (Mijovic et al. 1985) However it has also been shown that nodule size does affect toughness, but in similar manner to how cross-link density shapes toughness. (Mijovic et al. 1979; Mijovic et al. 1981)

Properties are generally at a maximum when the ratio of amine to epoxide is stoichiometric. However as noted by Vanlandingham, amine molecules can aggregate at the surface and result in a localized region that is not at the stoichiometric point and thus has different properties than the bulk. (Vanlandingham et al. 1999) Mijovic has shown a correlation between toughness and dynamic mechanical properties of nodular epoxy resins. (Mijovic et al. 1979; Mijovic et al. 1981) However it should be noted that mechanical properties do not follow a linear relationship to nodular size. Instead properties follow a parabolic relationship, first increasing with nodular size and amine content and then decreasing. Peak values are found to be around the stoichiometric point.

Like brittle ceramics, when epoxy samples are loaded until failure, a fractal structure forms on the fracture surface. This fractal structure is characterized by three distinct regions on the fracture surface; mirror, mist, and hackle. Figure 3-5, adapted from Plangsangmas, is a schematic of an epoxy fracture surface. (Plangsangmas et al. 1999)

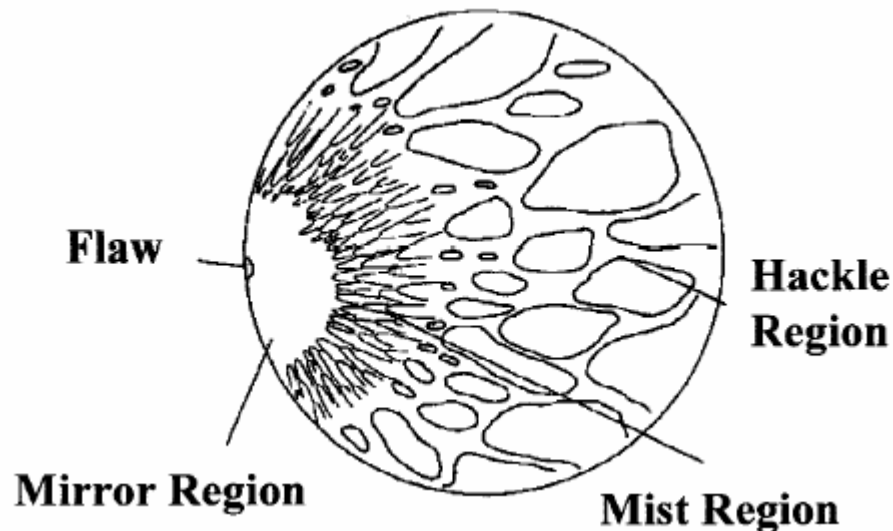


Figure 3-5. Fractal Structure of Fracture Surface of Epoxy. (Plangsangmas et al. 1999)

Fractal structures are often characterized for fractal dimension. Fractal dimension is a measure of the tortuosity of a fracture surface. Joseph et al. has shown that AFM can be used to calculate the fractal dimension of epoxy fracture surfaces. (Joseph et al. 1998) Their work has shown that epoxies have a fractal dimension of approximately 0.26 for all fracture regions (mirror, mist, and hackle); this indicates that fracture surfaces are self-similar. It is unclear at this point how fractal dimension relates to nodule size and epoxy resins, but it has been shown that fractal dimension can be related to toughness. An in-depth review of fractal dimension can be found in Chapter 2.

Additional materials have been shown to have nodular microstructures. Examples of other nodular materials are silsesquioxanes and certain polymer blends. (Lopez et al. 2002; Auad et al. 2003) Nodular microstructures in polymer blends are attributed to the insolubility of one phase in another. Silsesquioxanes, however, are similar to epoxies in structure and are also considered to be thermosetting polymers; it is unknown as to why they form nodular structures.

3.3 Review of Silsesquioxanes

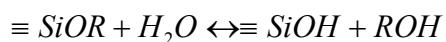
3.3.1 Introduction to Silsesquioxanes

Silsesquioxane materials are hybrid inorganic-organic materials combining key properties of both ceramic materials and polymeric materials. Silsesquioxanes are silicon based materials defined as having three bridging oxygens and a fourth organic group. The classification and ultimate properties of silsesquioxane are dependent on the fourth group attached to the central silicon. There are virtually limitless possible organic units that can be attached to the central silicon atom. This research will focus on the properties of novel polymethylsilsesquioxanes synthesized from methyltrimethoxysilane and the relationship between microstructure and fractal failure.

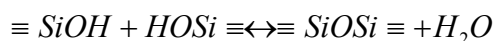
Polymethylsilsesquioxane (PMSQ) has a nodular microstructure. The microstructure is similar to that of epoxy resins. (Racich et al. 1976) It will be postulated by Dr. Baney that the scale of the nodular microstructure determines the ultimate mechanical properties of the material.

Silsesquioxanes are synthesized by sol-gel like reactions. Traditionally, silica sol-gel reactions use acids or bases to promote hydrolysis and condensation reactions in precursors. (Brinker et al. 1989) Monomers condense to form very small colloidal particles which then connect together to form the gel network. The two chemical

reactions that typify most sol-gel systems are an alkoxy hydrolysis reaction and a hydrolytic condensation reaction. The typical reactions for silica sol-gel are:



and



Studies have shown the pure silica sol-gel, derived from tetramethoxysilane or similar compounds can have an inherently fractal nature on the colloidal scale. (Schaefer et al. 1986) The clusters have a mass fractal; essentially the mass of the cluster is proportional to r^{dm} where dm is the mass fractal constant. Mass fractal values are easily measured using Small Angle X-ray Scattering (SAXS). (Orcel et al. 1986) This value is not to be confused with D^* , a brittle fracture fractal constant used in the WMP Theory. Traditionally sol-gel reactions have very large volumes of solvents that must be removed from the final body. The result is an extremely porous network. The combined effects of Ostwald ripening and sintering to remove the porosity eliminates virtually all of the microstructural evidence of a cluster microstructure. The techniques used to synthesize the polymethylsilsesquioxane that will be studied in this research result in a dense body with zero porosity. As a result the samples do not have to be heat-treated and the desired structure is not lost.

It has been previously established that silsesquioxane resins have a nodular microstructure. (Baney et al. 1999) The structure of the resin is a result of both intramolecular condensation, where the molecule folds back on itself creating a closed cluster, and intermolecular condensation, where two large silsesquioxane clusters connect to form a larger network. The degree of inter- versus intramolecular condensation is dependent on the size and charge distribution of the organic group and the processing parameters. A larger more steric organic group will lead to more intramolecular

condensation and a smaller group will result in more intermolecular condensation. Unique to methylsilsesquioxanes, the very small organic group (methyl) can lead to an extremely high degree of intramolecular condensation under certain reaction conditions. This structure is commonly called the T₈ cubical octomer, which consists of a silica cube with methyl groups on each corner. Several novel techniques have been developed to prevent the formation of cubical octomer and force the structure to form an open network. Many of these techniques focus on complex solvent interactions that serve to control the organic/inorganic nature of the resin, or unique hydrolysis condensation routes. (Bourget et al. 1999; Takamura et al. 1999; Kondo et al. 2000; Crouzet et al. 2003) The research in this work focuses on a non-catalytic route, foregoing the traditional use of acid or base in sol-gel chemistry.

In addition to the cubical octomer and the random network, a third possible structure can be found in silsesquioxane materials. First identified in phenyl silsesquioxanes, a ladder structure can be formed upon hydrolysis. (Baney et al. 1995) The presence of a ladder structure is characterized via x-ray diffraction (XRD). When a silsesquioxane resin is examined with XRD, two broad halos are formed. One halo corresponds to the size of the silica tetrahedron. The second halo occurs at smaller 2θ values, corresponding to the spacing across the width of the ladder or the X-Si-O-Si-X length. For polymethylsilsesquioxane, this spacing corresponds to approximately 8.14Å.

Computer modeling has long been used in sol-gel reactions to model how clusters form and approximate sizes of the clusters. It should be noted that clusters are not nodules. Generally clusters are less than 1 nm in diameter, nodules, conversely, are generally 10 nm to 1 μm in diameter. It is convenient to think of clusters as the building

blocks of nodules. The model most commonly used is called the Eden model and assumes that monomers will add randomly to available sites on the cluster. A modification of the Eden model, called the Poisoned Eden model, uses model monomers that have been poisoned, or not completely hydrolyzed, blocking growth along particular sites in the cluster. This is very similar to the monomers used to synthesize silsesquioxanes in that they are permanently poisoned with only three available reaction sites. The results of this research indicate that high levels of poisoning increase cluster size for the same number of monomers. (Schaefer et al. 1986) The clusters in these studies and in most sol-gel reactions are not to be confused with the nodules which are the focus of this research. Early work on polymethylsilsesquioxane has shown nodules to have a radius around 200 nm. It is unknown however, what the substructure of the nodules is at this time, whether it is composed of small spherical clusters creating a hierarchy of structure, or if polymethylsilsesquioxane nodules are homogenous and grow continuously from solution to their observed size. It is the belief of the author that when the inherently poisoned methyltrimethoxysilane is reacted in non-catalytic environments, it will result in different structures, which are not necessarily cluster-like, on the nanoscale. This fact will ultimately affect the mesoscale nodules.

3.3.2 Applications of Silsesquioxanes

Silsesquioxane materials have nearly as wide a variety of uses as possible organic groups that can be attached to the silica network. In recent years, the drive for smaller, faster electronic devices has helped pushed research into silsesquioxanes. (Wang et al. 1999; Yang et al. 2001) From a materials science aspect, the most crucial element to making faster, smaller electronics is the interconnect material. This material must have a low dielectric constant, which is necessary to prevent cross talk between neighboring

wires and increase signal propagation speed. Most of the work in low-k materials revolves around creating controlled porosity films. Using the rule of mixtures, the dielectric constant of the film is a function of the dielectric constant of the material and the porosity. Higher porosity materials have lower dielectric constants because air has a constant slightly above unity. The silsesquioxane organic groups help increase porosity and have an inherently lower dielectric constant.

In addition to having a low dielectric constant, silsesquioxanes are also very thermally resistant in comparison to traditional carbon based polymers. Depending on the organic group, silsesquioxanes can have decomposition temperatures in excess of 550 C°. (Fan et al. 2001) This property is desired in a variety of applications; in particular it is extremely important in the case of electronic devices, where the entire package is subjected to multiple high heat treatments during processing.

Silsesquioxane resins can also be used as ceramic precursors. Upon pyrolyzation in a non-oxidizing atmosphere, silsesquioxanes convert into silicon oxycarbide (SiOC). (Babonneau et al. 1994; Bujalski et al. 1998; Eguchi et al. 1998) Silicon oxycarbide is a high temperature ceramic material that when derived from silsesquioxanes has properties in excess of traditional ceramic processing synthesis routes. Silicon oxycarbide synthesized from silsesquioxane is non-stoichiometric, having a variable carbon to silicon ratio. The properties can be engineered by controlling the amount of carbon present in the resin, which is a function of the organic group present in the silsesquioxane. Pre-ceramic precursors such as polymethylsilsesquioxane have found a niche in the synthesis of high temperature and toughness materials, and are a novel route to better ceramics through chemistry.

3.3.3 Characterization of Silsesquioxanes

The techniques used to characterize silsesquioxanes most commonly relate structure to a particular parameter. Generally silsesquioxanes are characterized for molecular structure or molecular weight and related to some physical property, whether it be dielectric constant or toughness and so forth.

Many different techniques can be used to measure molecular weight of polymers such as Gel Permutation Chromatography (GPC) and Matrix Assisted Laser Desorption Ionization Mass Spectroscopy (MALDI). However, it has been shown in the literature that GPC is not a viable technique for measuring the molecular weight of silsesquioxanes.

Tecklenburg has directly compared GPC and MALDI for measurements of a silsesquioxane based polymer. (Tecklenburg et al. 2001) The polymer synthesized by Tecklenburg was not a pure silsesquioxane, but contained some siloxane linkages; however the polymer was fundamentally a silsesquioxane. The synthesized polymer was fractionated using super-critical fluids into 21 distinct fractions. This was done to make measuring molecular weight easier by concentrating similar molecular weight species together.

The results of Tecklenburg are shown in Table 3-1 and show that as molecular weight increases, the validity of GPC decreases. He further cites the reason for this is that the disparity in molecular weight is due to the fact that the molecular radius of silsesquioxanes does not follow a normal curve used for calibration of GPC. This is further evidenced by Figure 3-6. Figure 3-6 plots the molecular weight of several fractions as found by MALDI.

Table 3-1. GPC and MALDI Molecular Weights of Silsesquioxanes from Tecklenburg

Fraction	GPC Mn	MALDI Mn
8	3415 g/mol	3778 g/mol
13	9070	12,087
18	24,130	45,434
20	43,770	100,995
21	56,160	124,847

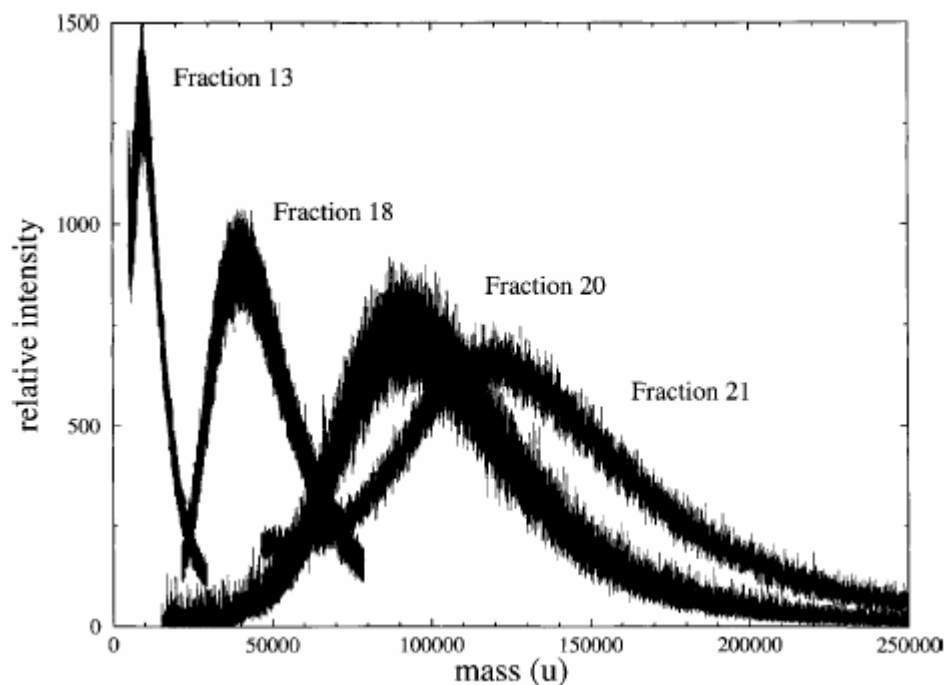


Figure 3-6. MALDI Molecular Weights of Silsesquioxane Fractions (Tecklenburg et al. 2001)

One can see in Figure 3-6 that the distribution of molecular weights from one fraction to another overlap one another. This is a byproduct of the fractionation method. As previously mentioned super-critical fluids were used to fractionate this particular polymer. Super-critical fractionation works by changing the solubility parameters of a super-critical fluid by adjusting the temperature or pressure. The changes in temperature or pressure allow one to fractionate a polymer roughly by molecular weight, which in general is the biggest factor determining the solubility of a polymer.

Silsesquioxanes differ in that there are nearly an infinite number of complex three dimensional structures. In many cases there are multiple isomeric conformations of the same molecular weight. Different structures of the same isomer have different solubilities, as evidenced by the molecular weight distributions in Figure 3-6. This can be further related to structure and the inaccuracies of GPC. Gel Permeation Chromatography assumes that every molecule of the same molecular weight will have the same hydrodynamic radius. However with some imagination one can visual a high molecular silsesquioxane molecule that is very condensed forming a small tight cluster or one that is very large forming a giant network. Although they have the same molecular weight, the GPC retention times would be vastly different.

Not all researchers have used fractionation when studying molecular weight. Mori et al have use MALDI to characterize synthesized silsesquioxane polymers. (Mori et al. 2004) However it should be noted that the polymer studied by Mori was shown to have a much lower molecular weight than that examined by Tecklenburg. Additional researchers have shown similar results when using MALDI to characterize low molecular weight silsesquioxanes. (Wallace et al. 1999) As such, fractionation was likely not required to increase sensitivity. (McEwen et al. 1997)

Matrix Assisted Laser Desorption Ionization is a very powerful tool for characterizing large molecular weight silsesquioxanes. However most of the research reported in the literature using MALDI for characterization of silsesquioxanes has focused on low molecular weight polyhedral oligomeric silsesquioxane structures (POSS). (Falkenhagen et al. 2003; dell'Erba et al. 2004; Anderson et al. 2005)

MALDI can also be used as a method of investigating structure. For low molecular weight polymers, there are generally one or very few isomers of an oligomer. Many research groups have developed software for calculating the structure of an oligomer from molecular weight. Wallace has used MALDI data for several low molecular weight silsesquioxanes to investigate the role the organic group has on intramolecular condensation. (Wallace et al. 2000) Overall it was shown that the nature of the R-group and the nature of the reaction process greatly affected the degree of intramolecular condensation.

Wallace contrasted the ability of NMR and FTIR to determine the structure of silsesquioxanes against that of MALDI. Using MALDI he was able to determine exact structures, and classified techniques commonly used to characterize the structure of silsesquioxanes, NMR and FTIR, as semi-quantitative at best.

Fourier Transform Infrared Spectroscopy (FTIR), while not able to interrogate the exact structure of a silsesquioxane polymer, can be used to investigate the nature of intramolecular binding. There are two IR active Si-O-Si peaks in silsesquioxanes. Lee has identified the two peaks as 1120 cm^{-1} and 1030 cm^{-1} . (Lee et al. 2002) Lee further states that these peaks are the cage and network structures respectively. Cage structures are generally molecules with high levels of intramolecular condensation on a short range order. An example would be the polymethylsilsesquioxane cubical octamer, which is an entirely cage structure.

It should be noted however, that not all research groups are convinced that the 1120 cm^{-1} and 1030 cm^{-1} peaks in a silsesquioxane FTIR spectra are separate structural entities. Oh states that absorbance peaks near 1133 cm^{-1} are from a Si-O stretch and absorbance

peaks near 1031 cm^{-1} are due to a Si-O-Si asymmetric stretch. (Oh et al. 2002) Conversely the work of both Oh and Lee indicates that the ratio of the two peaks changes with thermal curing of the investigated materials. This would lead one to believe that at elevated temperatures there is a structural rearrangement of the polymer which results in a change in peak absorbance of the aforementioned peaks.

Within limitations MALDI can be used to determine isomeric structure oligomers, and FTIR can be used to semi-quantitatively investigate physical structure; conversely, Nuclear Magnetic Resonance (NMR) can be used to determine chemical structure of silsesquioxane polymers.

Nuclear Magnetic Resonance is a powerful tool for quantifying the chemical nature of a desired atom in a sample. Silicon-29 NMR is commonly employed to investigate the silsesquioxanes. Arkles and Larson report in a detailed review Silicon-29 NMR peaks of many silicon compounds found in the Gelest Annual Catalog. (Arkles et al. 2004)

As previously mentioned, a silicon atom in a silsesquioxane molecule has one organic group and three oxygens bonded to it. Some of these oxygens are bridging oxygens in that they connect two silicon atoms together. Conversely some oxygen atoms are bound to hydrogen atoms forming hydroxide groups or silanols. The chemical shift of a silicon atom in a silsesquioxane is dependent on the number of silanols and bridging oxygens.

Kondo has used Silicon-29 NMR to investigate the structure of polymethylsilsesquioxane polymers. (Kondo et al. 2000) The polymethylsilsesquioxane synthesized by Kondo was characterized for the amount of hydroxide present in the

structure. Because silsesquioxanes are polymers, the peaks of the NMR spectra are broad peaks, not the sharp, narrow peaks commonly found in smaller structures. Kondo reported a range of peaks for each type of silicon in a silsesquioxane. (Kondo et al. 2000)

Nuclear Magnetic Resonance is a very powerful tool for determining the chemical structure of silsesquioxanes and silicon based materials. It has been used extensively to measure the hydroxide content of silsesquioxanes.

3.4 Conclusions

While there are dissenting views on the existence of nodules in epoxies, it is the author's opinion that they are in fact real. Two explanations exist as to why researchers come up with different results regarding nodular microstructures. It is very plausible that not all compositions result in a nodular microstructure. As reported above, chemical composition and processing parameters can greatly influence final nodule size of an epoxy. Conversely, it is possible that techniques used to investigate structure such as SAXS or AFM are not sensitive enough to pick up differences in structure. It is unknown at this time how nodules form or what their role is on mechanical properties.

Silsesquioxanes, on the other hand, are complex hybrid inorganic-organic polymers which have also been shown to form nodular structures. The structure of silsesquioxanes is very complex, however different silsesquioxanes are easy to synthesize. This should allow one to investigate the nature of the R-group and steric effects on nodule formation. There are many different techniques for characterizing silsesquioxanes, although some such as FTIR are not without controversy.

CHAPTER 4 FRACTURE PROPERTIES OF EPOXY RESIN

4.1 Introduction

Analyzing the effects of a nodular microstructure on the mechanical properties of epoxy resins is a novel application of the West Mecholsky Passoja theory (WMP). Should a relationship between nodular size and toughness be found, it would be possible to endeavor to engineer an epoxy with a different nodular size and thus different toughness.

Mechanical properties have been previously related to fractal relationships. (Mandelbrot et al. 1984) The fracture surface of many brittle materials is a self-similar pattern consisting of a mirror, mist, and hackle region. The WMP theory takes the fractal structures found in fracture surfaces one step further by relating the toughness of a sample to the fractal dimension of the fracture surface.

The West Mecholsky Passoja theory asserts that toughness is related to a fundamental structural parameter a_0 . (Mecholsky et al. 2002) The relationship between toughness and a_0 is given by the equation:

$$(4-1) K_{Ic} = E(a_0 D^*)^{1/2}$$

Where K_{Ic} is the toughness, E is the modulus, a_0 is the structural parameter, and D^* is the fractal dimensional increment. The fractal dimensional increment is the decimal portion of the fractal dimension. The fractal dimension and dimensional increment are reviewed in detail in Chapter 2.

We have postulated for this work that a_0 is proportional to the nodular size and might be akin to the size of the interstitial volume formed by the packing of nodules together. Scanning electron micrographs of nodular epoxies have revealed a randomly packed structure. Assuming a narrow distribution of nodule size, a randomly packed structure should be 63% nodules by volume, and 36% interstitial material. This brings up the question; What is the nature of the interstitial material in relationship to the nodule, and how does it affect the toughness of an epoxy resin?

There has been significant research on establishing a link between nodular size of epoxy systems and mechanical properties. (Mijovic et al. 1979; Mijovic et al. 1979) Additionally many researchers have investigated the nature of the nodular microstructure. (Errath et al. 1959) Not all researchers, however, are convinced that nodules do exist. (Duchet et al. 2003) It is possible that not all epoxy compositions studied are nodular. This would be one explanation of the discrepancies between multiple works of research. The epoxy composition investigated in this work has been confirmed to have a nodular microstructure and is derived from a method of preparation found in the literature. (Racich et al. 1976)

One possible explanation for nodule formation is that as the curing reaction begins minor inhomogeneities begin to form in the bulk of the epoxy resin-curing agent solution. This results in a cluster that has a slightly different chemical potential or solubility than the rest of the bulk. Initially this difference in chemical potential or solubility could be a function of the surface energy in the cluster in relation to the free energy of the uncured bulk. The difference in energies would drive the curing reaction at a faster rate at the

surface of the cluster than in the bulk of the solution. Eventually the nodule would reach a size where the surface energy has to decrease to a point where it no longer dominates the reaction process and nodule growth slows greatly, but does not stop altogether. This possible explanation would answer the question of why nodules are so uniform in size as reported by researchers in the literature.

Epoxy samples were characterized for their toughness, nodular size, modulus, and fractal dimension with the intent of fitting the data to the West Mecholsky Passoja theory. It was expected that the toughness of the epoxy samples will be proportional to the size of the nodules of the sample. It is the author's hypothesis that nodule size can be related to the size of the interstitial volume found between nodules. Additional experiments were performed to better understand the nature of the system being investigated and inquire about nodules and nodular formation.

4.2 Epoxy Synthesis and Processing

Samples were prepared from Epon 825 epoxy resin and cross-linked with Diethylenetriamine (DETA). Epon 825 is a high purity diglycidylether of bisphenol-A manufactured by Shell Chemical, and it has an equivalent mass of 176 grams. An equivalent is defined as the mass of a polymer corresponding to one mole of reactant group, in this case the epoxide group. Diethylenetriamine is a penta-functional amine curing agent with three amine groups; two primary and one secondary amine. DETA has an equivalent mass of 20.6 grams. The stoichiometric ratio of DETA to Epon 825 is 11.7 grams per hundred grams resin (phr).

Samples were cured in silicone molds with 8 or 10 phr of DETA, or a sub-stoichiometric ratio. These compositions were chosen to closely follow reported

literature. (Racich et al. 1976) The two compositions were chosen because they have been previously shown to be nodular and have different nodule sizes.

A sample of Epon 825 resin was weighed and manually mixed with DETA. The samples were then degassed for 30 minutes using a vacuum pump. After removing bubbles, the resin was poured into the molds.

Samples were cured at 50°C for 24 hrs and removed from the molds. The molds were fabricated from Dow Corning Silastic T-2 silicone. Samples were produced in a dog-bone shape that conforms to ASTM standard D638. This standard is primarily used for calculating the modulus of polymer resins. Samples were strained at three different strain rates, 0.1 mm/min, 10 mm/min, and 100 mm/min.

Ten samples were measured for each composition and strain rate. Samples were loaded until there was failure in tension. A laser extensometer was used to calculate displacement and modulus. Modulus was calculated as the slope of the stress-strain curve. Optical microscopy was used to calculate the flaw size of broken samples so that toughness could be calculated. Nodular size was determined using a scanning electron microscope. Additionally fractal dimensional increment was calculated using an optical microscopy technique and a derivation of the Richardson method. Additional techniques for measuring fractal dimension were used to corroborate data gathered by optical microscopy.

4.3 Methodology and Experimental

Methodology used for investigation can be broken into three distinct tasks; characterization of mechanical properties, characterization of nodule size, and characterization of fractal dimension. The following section will detail the methods used for each of these tasks and present a brief discussion on the results gathered in each task.

4.3.1 Characterization of Mechanical Properties of Epoxy Resins

4.3.1.1 Introduction

Tensile testing was used to break all samples investigated in this research. Tensile testing was selected because of ease of sample preparation and reproducibility of data. As previously mentioned, samples were prepared in accordance with ASTM standard D638. This standard describes a process of measuring the modulus of a polymeric resin. Samples were testing on an Instron 1122 frame with a 1000 lb load cell. Mechanical vice grips were used to secure the sample. An attached laser extensometer was used to gauge displacement. The nominal gauge length for samples investigated was 12.5 mm. Load was recorded for a given displacement. Failure stress and modulus was recorded from these experiments. Optical microscopy was used to determine flaw size. The flaw size combined with the failure stress was used to calculate toughness.

4.3.1.2 Modulus

As previously mentioned, two compositions and three strain rates were investigated. Modulus was calculated as the slope of the stress-strain curve. Ten samples were broken for each data point. Table 4-1 represents the average of all samples for each data point and the associated error of one standard deviation from the mean.

Table 4-1. Modulus and Percent Error of Epoxy Resins at Different Strain Rates

Strain Rate	8phr		10phr	
	E (GPa)	%Err	E (GPa)	%Err
0.1	1.41	4.9	1.41	3.9
10	1.45	4.8	1.42	3.3
100	1.51	9.2	1.44	1.5

The following figures are examples of the stress-strain curve generated by the tensile test. Figure 4-1 indicates three superimposed stress-strain curves for 8 phr DETA. Figure 4-2 indicates three superimposed stress strain curves for 10 phr DETA.

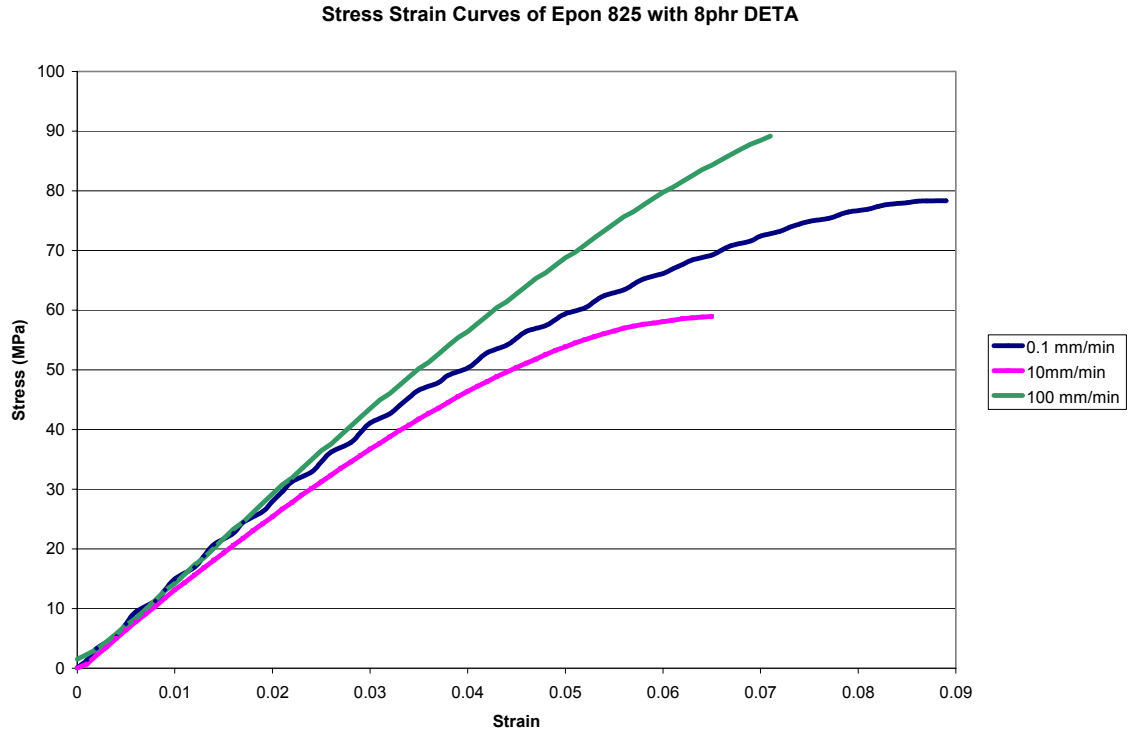


Figure 4-1 Stress-Strain Curves of Epon 825 with 8 phr DETA)

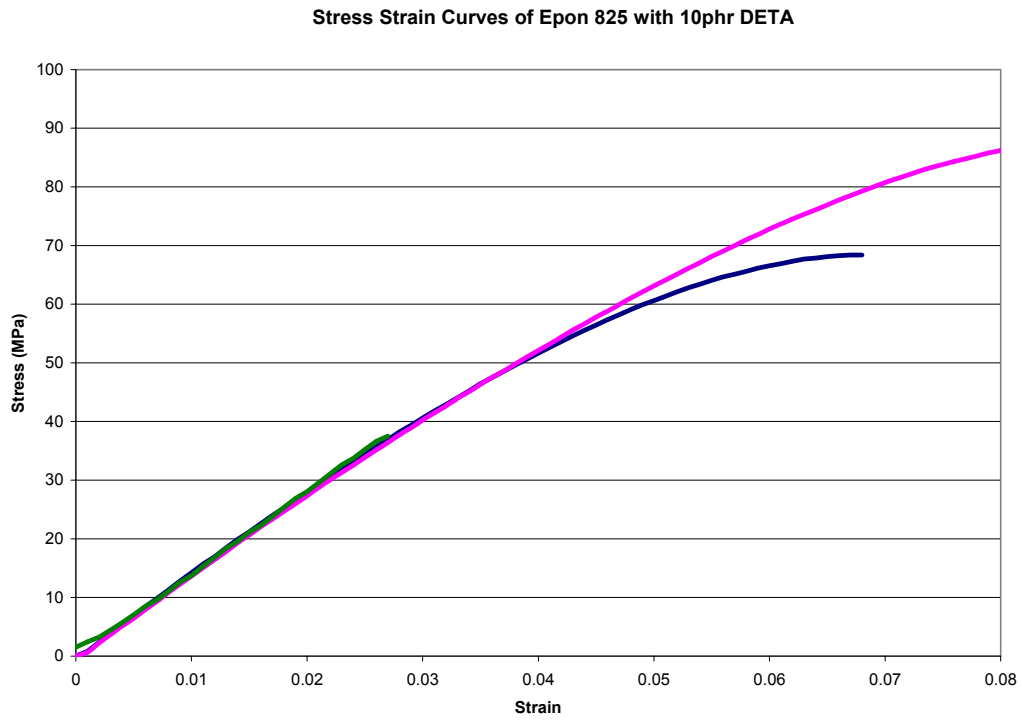


Figure 4-2 Stress-Strain Curves of Epon 825 with 10 phr DETA

The curves in the figures are for samples that were close to the mean of all the samples for that strain rate and composition. The values for each specimen measured can be found in Appendix D in Table D-1. The samples in Figure 4-1 are #8 for 0.1 mm/min, #6 for 10 mm/min and #3 for 100 mm/min. The samples in Figure 4-2 are #3, #6, and #9 for 0.1, 10, and 100 mm/min respectively.

A two-tailed Student's t-test was used to gauge if the moduli for each strain rate were different from one another. The results of this analysis can be found in Table 4-2. Columns 1 and 2 are the moduli being compared. The percentages listed in Column P of Table 4-2 indicate the probabilities that the modulus of one strain rate is equivalent to the modulus of another strain rate. It is clear from the data in Table 4-2 that for each composition, the moduli for each strain rate are sufficiently different from one another. It should be noted that a t-test comparing the modulus of 0.1 mm/min 8 phr to 0.1 mm/min 10 phr returns a very high probability that the moduli are the same. However, as strain rate increases the modulus changes is greater for the phr 8 than the phr 10 samples. This indicates that the compositions are different.

Table 4-2. Student's t-test Results of Modulus of Different Strain Rates

8 phr DETA			10 phr DETA		
1	2	P	1	2	P
0.1	100	3%	0.1	100	7%
0.1	10	15%	0.1	10	34%
10	100	11%	10	100	12%

It appears from the data in table 4-1 that the modulus, decreases with increasing strain rate for both compositions, which was to be expected. Epoxies are brittle polymers; while they fail in a manner similar to ceramics, they still have time and

temperature dependent properties. The change in modulus with strain rate is due to the ability of polymer chains to rearrange and accommodate strain.

4.3.1.3 Failure stress

Failure stress (σ_f) was recorded as part of the tensile test for each sample. Failure stress was defined as the load under which a sample would fail. Table 4-3 lists the average failure stress for all compositions and strain rates tested. Additionally Table D-2 in Appendix D lists the failure stress for each sample tested. Although the data listed in Table 4-3 are similar, a t-test implemented comparing each strain rate with a composition to one another indicates that the failure stresses are different. The results of the t-tests can be found in Table 4-4.

Table 4-3. Failure Stress of Epoxy Resin at Different Strain Rates

Strain Rate	8phr		10phr	
	σ_f (MPa)	%Err	σ_f (MPa)	%Err
0.1	60	3.9	69	4.3
10	74	10.5	75	17.4
100	74	27.7	64	24.4

Table 4-4 Student's t-test of Failure Stress of Epoxy Resins

8 phr DETA			10 phr DETA		
1	2	P	1	2	P
0.1	100	3%	0.1	100	20%
0.1	10	0%	0.1	10	9%
10	100	47%	10	100	6%

4.3.1.4 Flaw size

The flaw size for each sample was measured using optical microscopy. For the purpose of this work, a Zeiss Axioplan 2 Microscope retrofitted with a custom built LEI XYZ stage capable of 0.1 μm was used to image samples. Images were taken at 5x magnification. Images were processed using the bundled MCID Elite 6.0 Morphometric

Software package. The following figures are examples of flaws found in the samples tested.

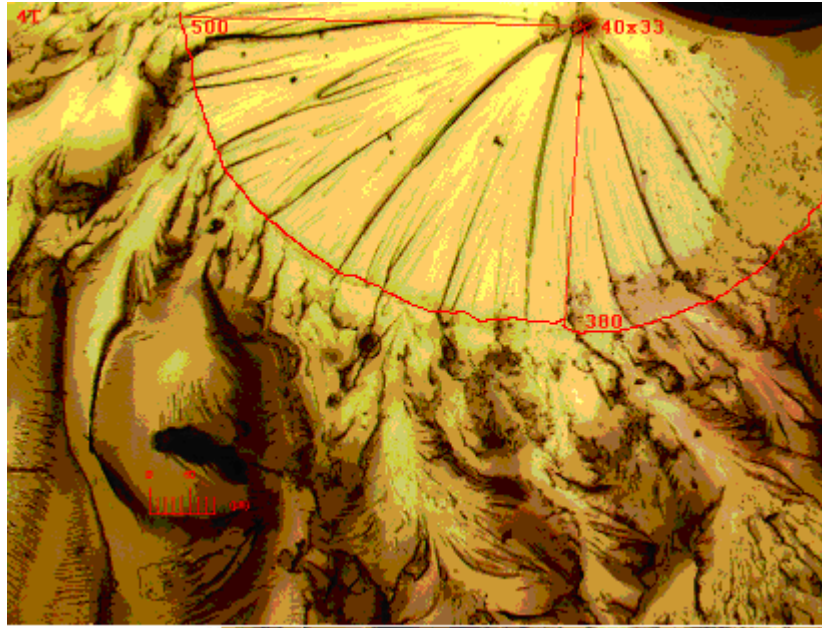


Figure 4-3 Example Critical Crack Size Produced through Slow Crack Growth

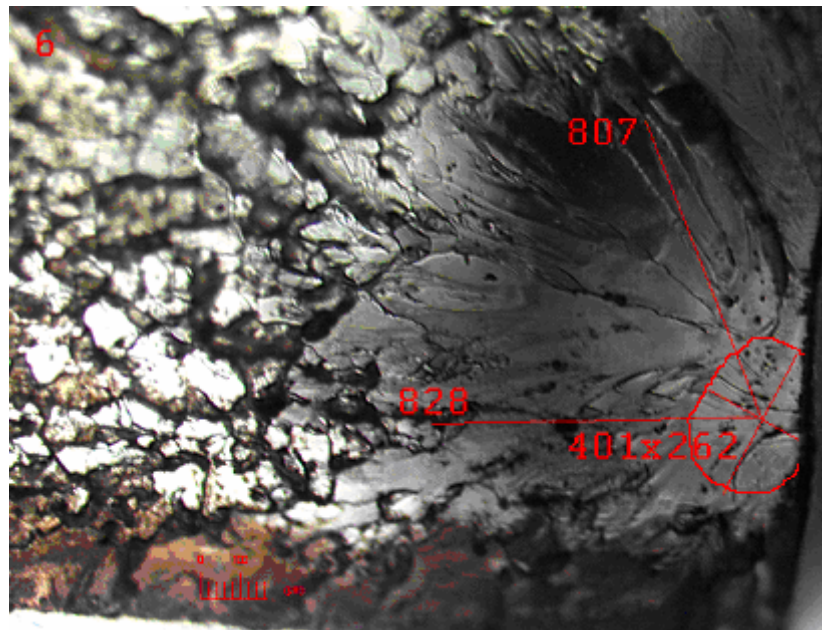


Figure 4-4 Flaw Size of Epon 825 with 8phr DETA at 100mm/min Strain Rate

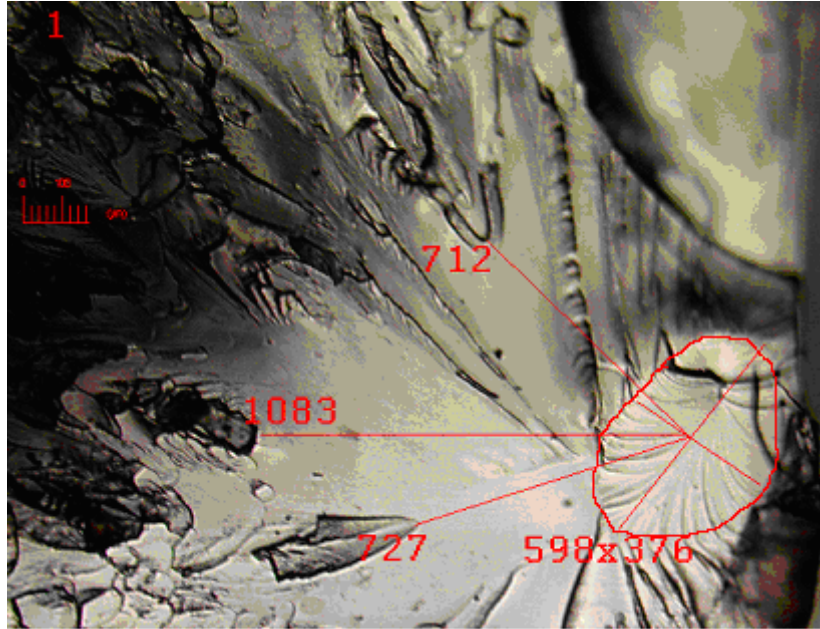


Figure 4-5 Flaw Size of Epon 825 with 10 phr DETA strained at 10mm/min

It was often found that the flaw was produced by slow crack growth. What this means is that the flaw starts out small from some initial defect in the structure and grows outward to a large size with an applied load. When the crack grows to a large enough size, fast brittle failure occurs, producing a mirror and hackle region. The region of slow crack growth can be seen close up in Figure 4-3 above. Note the size of the initial defect, 40 by 33 micrometers, and the growth of the flaw to a much larger size. The region of slow crack growth is visually similar to other polymers reported in the literature. (Kurtz et al. 1998)

It was found that the flaws were asymmetric. As such, an approximation was used to model the flaw as roughly circular. The size of the flaw can be found from the following equation:

$$(4-2) \ c = (ab)^{1/2}$$

Where a and b are one half the dimensions of the flaw and c is the effective radius of the flaw. Tables D-3 through D-8 in Appendix D list the flaw sizes of all samples measured in this research and the modeled radius.

4.3.1.5 Fracture mechanics and toughness

Toughness was calculated using the modeled flaw size (c) and the failure stress σ_f using the following equation:

$$(4-3) K_{Ic} = Y\sigma_f\sqrt{c}$$

Where K_{Ic} is the toughness, σ_f is the failure stress, c is the flaw size and Y is the stress intensity factor.

The value of Y depends on the shape of the flaw and location. A surface flaw has a greater Y value than a body flaw. As mentioned in the previous section, all flaws were modeled to be circular, as such, two Y values were used, 1.13 and 1.26. Surface flaws require an approximate 12% correction factor over body flaws. The location and Y value for each flaw for every sample can be found in the last columns of Tables D-3 through D-8 in Appendix D. Tables 4-5 and 4-6 are the toughness for all three strain rates for 8 phr DETA and 10 phr DETA respectively.

Table 4-5 Toughness of Epon 825 with 8ph DETA (MPa*m^{1/2})

	0.1mm	10mm	100mm
Average	1.34	1.09	1.06
Std Dev	0.28	0.28	0.23
Error	21%	26%	25%

Table 4-6 Toughness of Epon 825 with 10phr DETA (MPa*m^{1/2})

	0.1mm	10mm	100mm
Average	1.56	1.28	0.77
Std Dev	0.23	0.35	0.23
Error	15%	27%	29%

The accuracy of the data reported in the above tables can be checked by an Ln-Ln plot. An Ln-Ln plot is a component of the WLF theory. The WLF theory states that for a given temperature, the toughness of a material varies linearly with strain rate on a plot of the natural log of K_{Ic} vs. the natural log of strain rate. (Green 1998) Figure 4-6 shows the Ln-Ln plot of the strain rate and temperature for both compositions studied in this research.

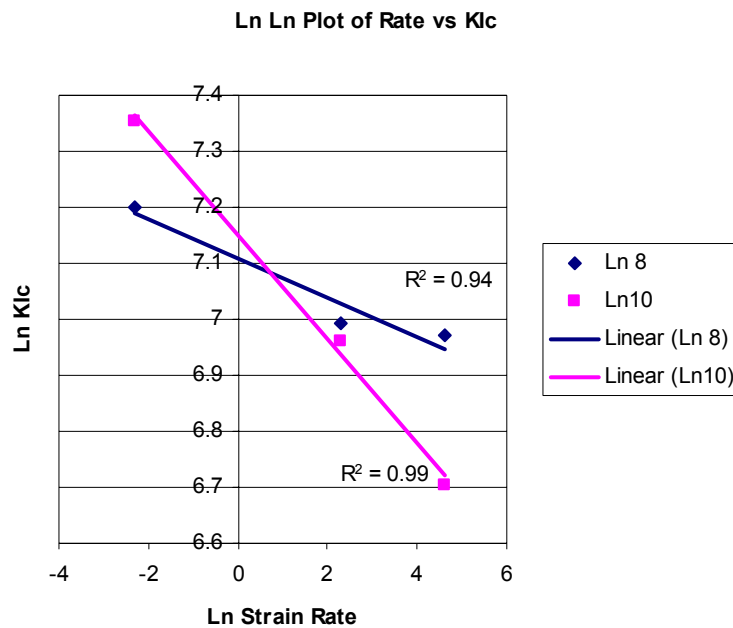


Figure 4-6 Ln-Ln plot of Strain Rate vs. K_{Ic} for Epon 825 Resins

The high R^2 values indicate that the toughness values calculated in this study closely match what would be predicted by the WLF theory.

It was mentioned in the previous section that the critical crack size is actually the by product of slow crack growth. The concept of slow crack growth presents an interesting problem. For both compositions, all samples characterized were made at the same time. As such it is safe to assume that the population of flaws from sample to sample for a particular composition is the same. Slow crack growth however, can result

in a change in critical crack size. The following table lists the average critical crack size weighted by stress intensity factor Y . Additionally, measurements of the initial flaw size revealed an average flaw radius of 20 μm . This can be seen in Figure 4-3.

Table 4-7 Average Critical Crack Size for Epoxy Resins (μm)

Strain Rate	8 phr DETA			10 phr DETA		
	0.1mm	10mm	100mm	0.1mm	10mm	100mm
Average	524	225	233	522	309	191
Std. Dev	191	100	118	141	126	89
Error	36%	45%	50%	27%	41%	47%

Utilization of Students t-test reveals that statistically, the critical flaw sizes for all three strain rates for 10 phr DETA are different from one another. However, for 8phr DETA 10 and 100mm/min were shown to be statistically similar. At higher strain rates, c is a smaller value; conversely, low strain rates result in large critical crack tip sizes. This would indicate that sub-critical crack growth is a strain rate dependent phenomenon.

4.3.2 Studies of Nodular Microstructure and Nodule Size

Epoxy samples were characterized for size and nature of nodules. Nodule size was measured with an SEM and the nature of the nodules was investigated using two different techniques. Three separate studies were performed; measurement of nodule size with SEM, extraction of nodules from resins with solvents, and mapping of iodine stain in relationship to nodular structure. The results of the studies presented here can be used to give insight into the nodular microstructure of epoxy resins.

4.3.2.1 Scanning electron microscopy

The nodular size of our epoxy samples was found with the aid of scanning electron microscopy (SEM). Samples were coated with a gold palladium alloy and images were taken at 10 KeV on a JEOL 6400 SEM. Several magnifications were used. In the

literature, Transmission Electron Microscopy (TEM) has been extensively used; SEM was selected for this research because of the ease of sample preparation.

Additionally, images were taken on both the fracture surface and exterior surfaces of the epoxy samples. It should be noted that initially a diamond blade saw was employed to investigate the nature of the nodule in the bulk of the sample. Cutting the epoxy with a diamond blade resulted in noticeable deformation of the nodules and was therefore not found to be a valid method of preparing surfaces for imaging.

Nodule size was determined with Image Pro Software. Multiple images from each composition were taken to ensure statistical significance. Samples were prepared by first washing the surface with acetone to remove excess organic matter. Previous work by Koutsky et. al. found that acetone can be used to etch the surface of epoxy and preferentially remove the interstitial material. (Mijovic et al. 1979) Care was taken to ensure that samples were not over-etched. Furthermore samples were exposed to iodine to stain the surface. This was done to increase the average atomic number of the surface. Higher atomic number coatings on SEM samples help to increase the signal-to-noise ratio of an image.

Figures 4-7 and 4-8 are typical SEM micrographs of Epon 825 with 8 and 10 phr of DETA respectively. Image Pro was utilized to determine an average value for nodule size. The images were loaded into the software and an algorithm was used to identify the nodules. The software allows the user to set threshold limits for upper and lower size. By setting the lower limit sufficiently high, it is possible to remove the embedded nodules from the count produced by the software. Judging visually, the nodule size in the

picture below was estimated to be on average around 100 nm for both compositions. As such a lower threshold for nodule size was chosen to be half or 50 nm.

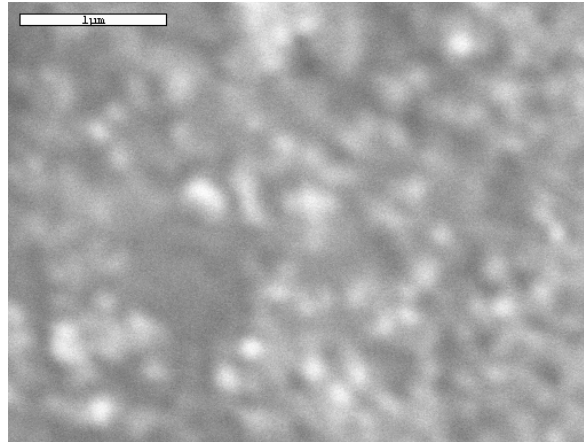


Figure 4-7 SEM Micrograph of Epon 825 with 8 phr DETA

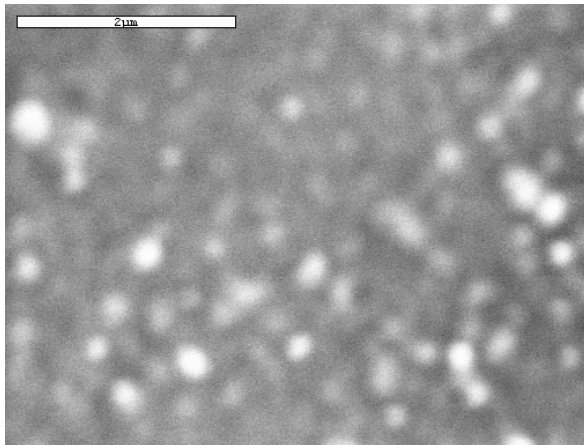


Figure 4-8 SEM Micrograph of Epon 825 with 10 phr DETA

The nodule sizes for the investigated resins appear to be approximately 75nm +/- 10nm and 100nm +/- 20nm for 8 and 10 phr respectively. These values are slightly larger than those found in the literature for similar composition. However, the differences can be explained by taking into account the roles different processing methods, cure schedules, and substrates.

4.3.2.2 Solvent extraction and particle size

As previously mentioned, acetone can be used to etch the surface of epoxies. Koutsky et al have shown that by exposing epoxy samples to acetone for long periods of

time nodules are actually etched. Additionally, evidence indicates that the acetone does not have a significant effect on the nodule, indicating that the acetone is more reactive with the interstitial material than with the nodule. This could indicate that the nodule is more highly cross-linked than the interstitial material.

Epoxy samples were treated with acetone for extended periods of time to separate the discontinuous material. It has been reported in the literature by Koutsky that acetone washing does not influence nodule size, but can instead, with extended exposure, wash nodules out from the gel network. (Mijovic et al. 1979) Samples were exposed to acetone for extended periods of time, 24 hrs, 48 hrs, and 2 weeks. The bulk epoxy was removed, leaving a mixture of acetone and particles. The resulting solution was concentrated by evaporating the acetone out at room temperature. This resulted in a white, viscous liquid with no visible nodules. This liquid is a mixture of nodules and unreacted resin monomers. Samples of the acetone-nodule solution were characterized using optical microscopy. No nodules were found using optical microscopy; instead there is featureless residue on the surface of the slide.

Recalling that the composition studied here is sub-stoichiometric, it appears that not only are nodules washed out, but so is a small portion of the resin. Further experiments using Soxhlet extraction confirmed the presence of unreacted monomer and low molecular weight oligomers. Soxhlet extraction was performed using a standard setup and acetone as the solvent. (Kim 2004) After running the extraction for 2 hours, the acetone was evaporated, leaving behind a viscous, white liquid.

The fact that nodules can be washed out of epoxies with a suitable solvent presents some interesting questions. Why do only some of the nodules wash out but not all? As

previously mentioned in the SEM study, nodules have a narrow distribution of sizes. It would appear that as nodules grow, the overall surface functionality density decreases. This reduction in functionality greatly slows down nodule growth. The ultimate size is a function of the ratio of epoxide to catalyst group (phr). This nodule size to catalyst relationship has been demonstrated previously in the literature. (Racich et al. 1976) Additionally it has been reported in the literature that failure occurs around nodules and not through nodules. This would indicate that nodules are only loosely bound to the surrounding structure.

4.3.2.3 Iodine staining of surfaces

One of the arguments against the existence of nodules is that some researchers have postulated that the nodule and interstitial material should have different densities. Small Angle X-Ray Scattering (SAXS) and Atomic Force Microscopy (AFM) have both failed to show any difference in density. In this study epoxy surfaces were stained with iodine in an attempt to elucidate the nature of the nodule and interstitial material. Three samples were investigated in this study, no staining, 5 minutes staining and 12 hours staining. Samples introduced to the confined iodine chamber quickly changed color, from transparent to a brownish color. The longer samples were exposed to iodine, the darker the sample would become. Washing the samples in acetone after staining would result in slight discoloration of the acetone from excess iodine washing off. It is postulated that the iodine forms a charged transfer complex with the carbon-oxygen-carbon bonds found in the diglycidyl ethers bisphenol-A (DGEBA) chain. This effectively forms a π - π bond that is stronger than hydrogen bonds but not as strong as covalent bonds.

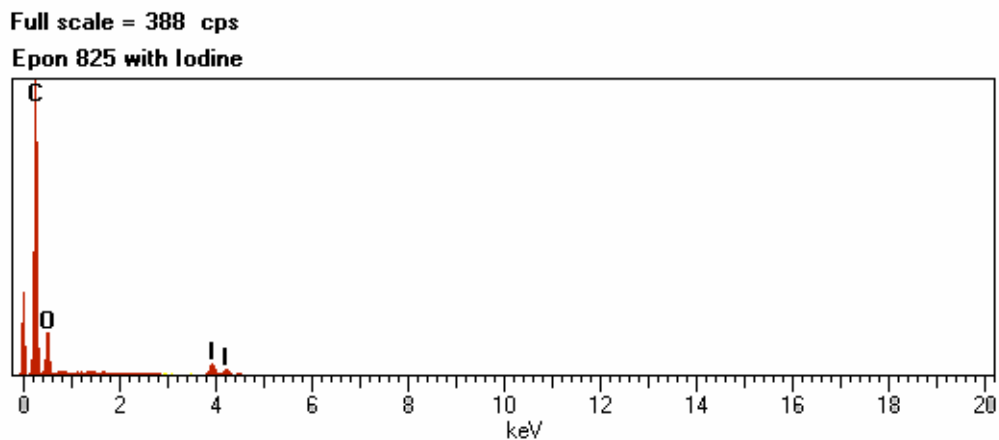


Figure 4-9. EDS Spectra of Epoxy Stained with Iodine for 5 minutes

Figure 4-9 is a representative EDS spectrum for an epoxy sample stained for 5 minutes. From the EDS spectra it is clear that there is, in fact, iodine present on the surface of the sample. EDS is not sensitive enough though, to give information about the local chemical structure of the iodine that would indicate whether or not the charged transfer complex hypothesis is correct. Additionally, it was noted that under normal secondary electron imaging, the epoxy sample stained for 12 hours appeared to degrade in real time from electron beam damage. This indicates that the sample may have been over-stained and the iodine may have in fact cleaved the C-O-C bonds.

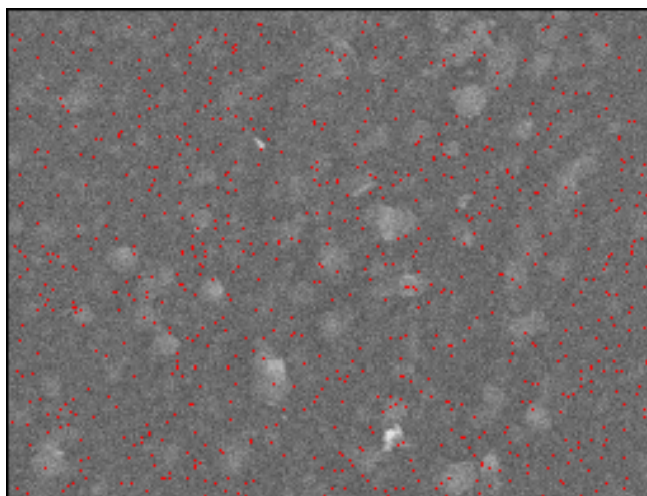


Figure 4-10. EDS SEM Image of Iodine (Red) Stained Epoxy Surface

The last figure in this section, Figure 4-10, is an EDS mapping of iodine on the surface of the specimen. The red areas in the image indicate the presence of iodine. There appears to be no evidence of preferential segregation of iodine in the nodular epoxy specimen.

The EDS spectra and mapping do indicate the presence of iodine in the epoxy sample. However there is no indication that the iodine prefers to reside in the nodule or interstitial material. It is possible that the iodine is too small of a molecule to observe any differences in density as it diffuses through the epoxy. Additionally it is also plausible that the difference in density between the nodule and the interstitial material is very small and therefore the difference in concentration of iodine is below the resolution limit of the microscope.

4.3.3 Investigation of Fractal Dimensional Increment

The fractal dimensional increment, D^* , is very important in the West Mecholsky Passoja theory. As previously stated the fractal dimension can be related to the tortuosity of the fracture surface. In Chapter 2 methods for calculating fractal dimension and D^* were described. These methods are time consuming and in some cases destroy the surfaces being characterized. This research has also focused on developing a technique that is comparable to other methods employed for calculating fractal dimension of fracture surfaces that is quick, simple, and non-destructive.

4.3.3.1 Introduction

The fractal dimensional increment was calculated using three separate techniques. Primarily a novel non-destructive slit-island method was used to generate images from which the fractal dimensional increment could be derived. The images were processed using Image-Pro software. The fractal dimension was calculated by hand using a small

selection of images and the Richardson method to confirm the validity of the Image-Pro software algorithm. Additionally the ratio of the mirror to the size of the flaw was used as a method to compare the values derived from the non-destructive slit-island method.

4.3.3.2 Flaw to mirror size

There are many different techniques for calculating fractal dimensional increment. Many of them are time consuming or require a great deal of sample preparation. Fractal dimensional increment can be quickly estimated by comparing the size of a flaw to the size of the mirror. When a sample fails in a brittle manner, three distinct regions are formed on the fracture surface; mirror, mist, and hackle. The ratio of the radii for each of the regions is constant regardless of size for any material. The size of these regions depends on the failure stress. For a given material, a sample that fails at a higher stress will have a smaller mirror than one that fails at a lower stress. Additionally the ratio of the mirror size to the size of the flaw can be used to quickly estimate fractal dimensional increment. Fractal dimensional increment can be found using the following equation:

$$(4-3) D^* = \frac{c}{r_m}$$

Where D^* is fractal dimensional increment, c is flaw size and r_m is the size of the mirror.

The mirror size was measured using optical microscopy. The size of the mirror was compared to the size of the flaw for a given sample as found in Section 4.3.2. Additionally, because the mirrors were often asymmetrical, the radius of the mirror was calculated as the average of two measurements using the same formula to calculate the size of the asymmetric flaws. Figure 4-11 is an example of the mirror and flaw for an epoxy sample where the flaw has the dimensions 239 by 166 micrometers and the mirror

has a radius from 719 to 664 micrometers. Additionally, example figures for each strain rate and composition can be found in Appendix D

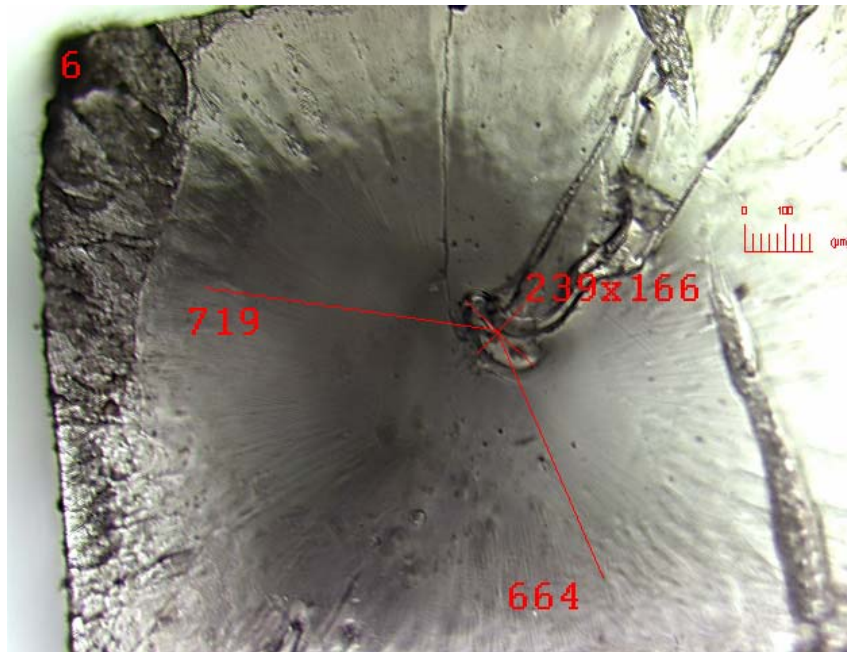


Figure 4-11 Flaw Size and Mirror for Epon 825 with 8 phr DETA strained at 0.1 mm/min

For each of the strain rates and compositions tested, three samples were measured for mirror size. Table 4-8 lists the average fractal dimensional increment for each of the compositions and strain rates investigated. Additionally Table 4-9 list the t-test results for comparing fractal dimensional increment distributions.

Table 4-8 Fractal Dimensional Increment by Flaw to Mirror Size for Epoxy Resins

	8 phr DETA			10 phr DETA		
	0.1mm	10mm	100mm	0.1mm	10mm	100mm
Average	0.23	0.15	0.15	0.24	0.22	0.11
Std Dev	0.06	0.06	0.04	0.07	0.05	0.05
Error	26%	40%	24%	28%	25%	45%

Table 4-9 Student's T-test of Fractal Dimensional Increment of Epoxy Resins

8 phr DETA			10 phr DETA		
1	2	P	1	2	P
0.1	100	0%	0.1	100	0%
0.1	10	1%	0.1	10	24%
10	100	97%	10	100	0%

The fractal dimensional increment seems to follow established trends in the literature. Tougher resins have slightly greater D^* values. However for the 8 phr DETA, the fractal dimensional increment appears to be the same for 10 and 100 mm/min strain rate. The Student's T-test comparing 10 and 100mm/min strain rate for 8phr DETA returns a 97% probability that the distributions are the same. The measurements of the mirror radii, flaw size, and examples of flaws and mirrors for each sample can be found in Appendix D in Tables D-9 through D-14 and in Figures D-1 through D-6.

It should be noted that this method is merely an estimate and cannot be used to solely describe the fractal dimension of a surface. The ratio of the flaw to mirror size can be shaped by residual stresses in the sample. It is unknown at this time if there are any residual stresses in the sample, however, it is unlikely. Additionally, operator error can play a large role in calculated values. Where the operator defines the start of the hackle region and sample geometry can affect final values. Additional experiments using different techniques should be conducted to confirm the results of Table 4-7.

Figure 4-12 plots the square root of the fractal dimensional increment versus the toughness of epoxy resins. This type of plot has been commonly used in the literature to show a relationship between fractal dimensional increment and toughness. The R^2 value is rather low, which could indicate that the flaw to mirror size ratio is not necessarily the best method for calculating fractal dimension.

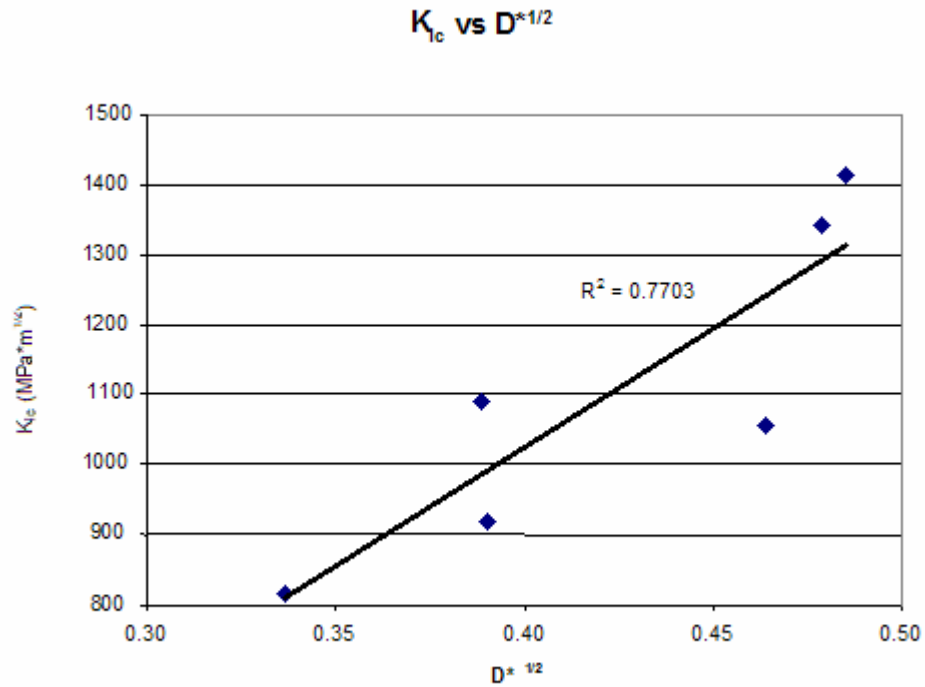


Figure 4-12. Fractal Dimension vs Toughness for Epoxy Resins

4.3.3.3 Non-destructive slit-island method

The non-destructive slit-island method is an adaptation of the commonly used slit-island method. The slit-island method calls for setting a specimen in an epoxy resin and polishing the surface to a fine grit to produce islands formed by the removal of the top of the fracture surface. This is shown in Figure 4-13.

The fractal dimension is then calculated by measuring the perimeter of the islands with different length rulers (Richardson method). This technique can be very time consuming, although it is acknowledged to be the best method for calculating fractal dimension and gives most accurate representation of the surface.

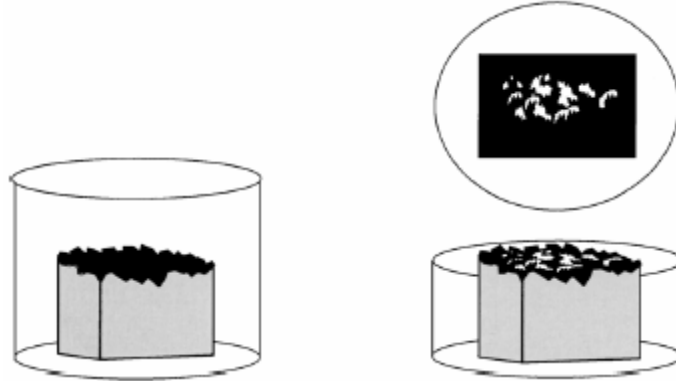


Figure 4-13. Slit-Island Method from Hill (Hill et al. 2001)

One of the drawbacks of the slit-island method is that it requires the sample, or in some cases a replica of the sample, to be polished, destroying the specimen or replica surface. One study of this research has focused on developing a suitable method of producing slit-island contours for a specimen without destroying the fracture surface. This was done by producing three dimensional images of a fracture surface using optical microscopy. This preserves the fracture surface should additional measurements become necessary.

The same microscope described in Section 4.3.2 to measure flaw size was used for this study. However, instead of focusing on the region surrounding the flaw, images were taken of the hackle region. The M3D package of the MCID Elite 6.0 Morphometric Software package was utilized for this study. This software package was used to generate 3D images from fifteen 2D “slices” taken at different focal planes with equivalent spacing. The 3D images were then manipulated using the software to produce digitally polished surfaces from which the fractal dimension can be calculated. The digitally polished images could then be characterized for fractal dimension using either hand calculations or software measurements.

This process is ideal for determining the fractal dimension of the hackle region of a fracture surface. As mentioned in Chapter 2, the hackle region is often characterized by the very large features on the fracture surface. This technique does not work well for the small features found in mirror region. This is because the perturbations found in the mirror region are often sub-micron in scale and cannot be properly imaged with an optical microscope.

Figure 4-13 is an example of a 3-D composite image generated using the MCID software. This image is taken down the z-axis of the composite. This is done to make image polishing easier and more compatible with other software. The accompanying figure, Figure 4-15, is a 2-D image of the same area of a sample as Figure 4-14. Figure 4-15 was generated using z-axis imaging. This is similar to the process used to generate the 3-D images, but does not result in a picture that can be digitally manipulated like the 3-D pictures. The 2-D pictures were used as a reference to ensure that the 3-D images were generated properly. The 2-D images are in color, whereas the 3-D images are in black and white.

Because each of the sections used to generate a 3-D image are often only a couple of microns apart, and the cross-sectional areas of each picture are often several hundred microns, 3-D data sets are very difficult to view at a perspective angle.

The process assigns a gray scale value to each pixel, from 0 to 255, where 0 is black and 255 is white. The higher the number, the higher the pixel is in the 3-D picture. From each specimen, several sections were digitally cut by specifying a range of gray scale values to display. Doing this, generates pictures similar to those used by Hill et al to calculate fractal dimension using a slit-island technique.(Hill et al. 2001) In most cases,

the higher elevations were removed; however, in some instances the lower sections were removed. Figures 4-16 through 4-19 are all sections taken from Figure 4-14. For each specimen at least 3 sections were generated along with a full height composite spectrum (Figure 4-14) and a 2-D real color composite image (Figure 4-15)



Figure 4-14 3-D Composite Image of Specimen



Figure 4-15 2-D Image of Specimen



Figure 4-16 0-50 Elevation Image Section

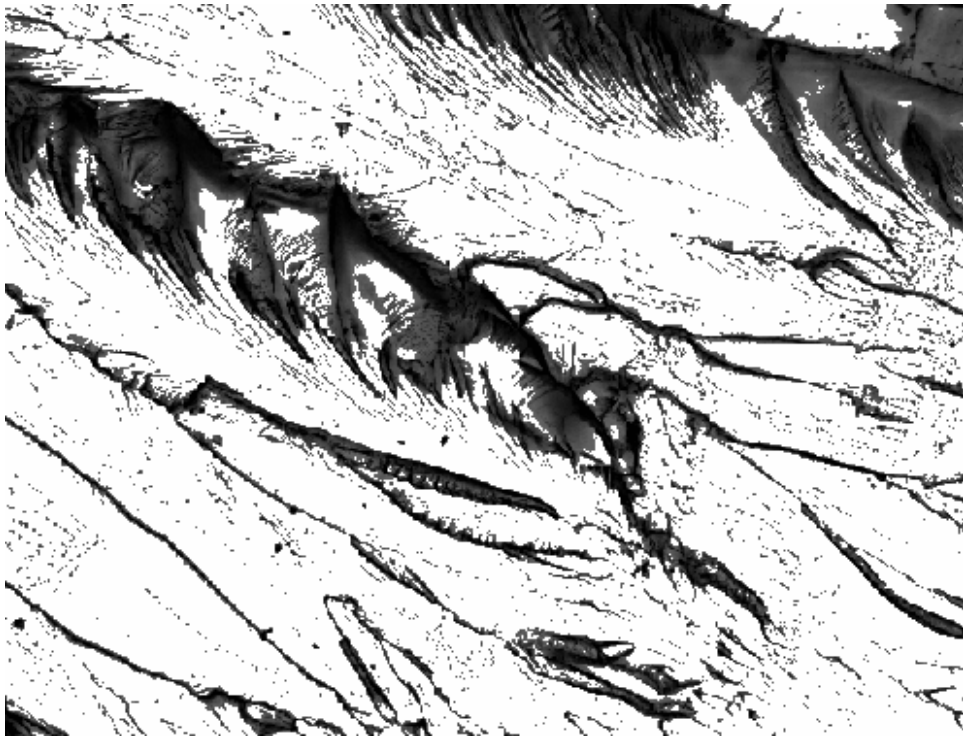


Figure 4-17 0-100 Elevation Image Section

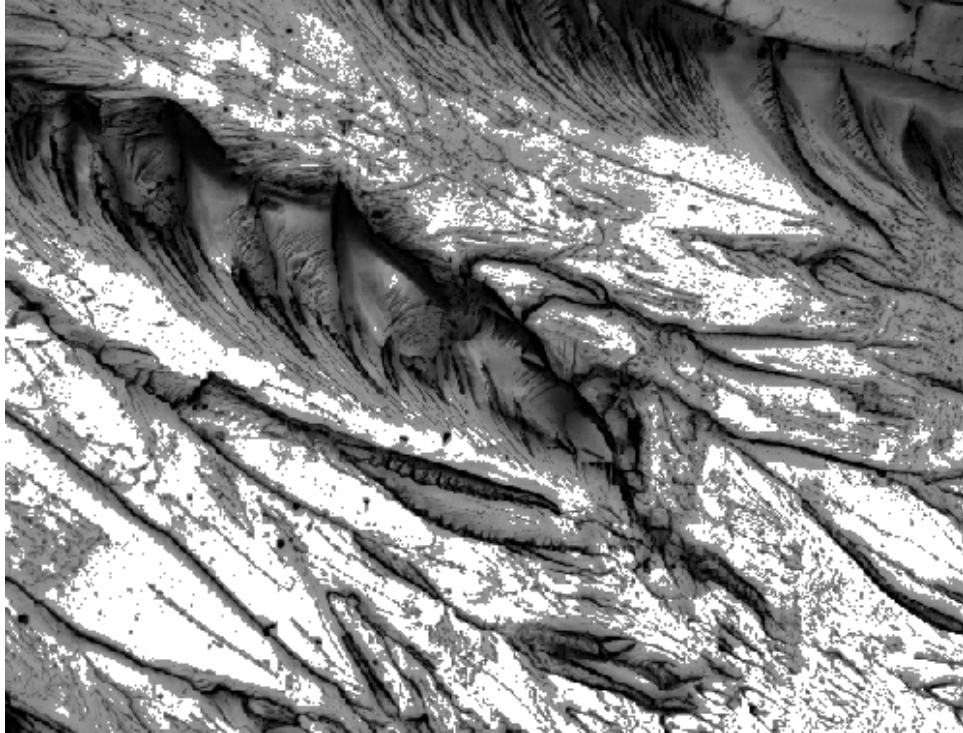


Figure 4-18 0-150 Elevation Image Section

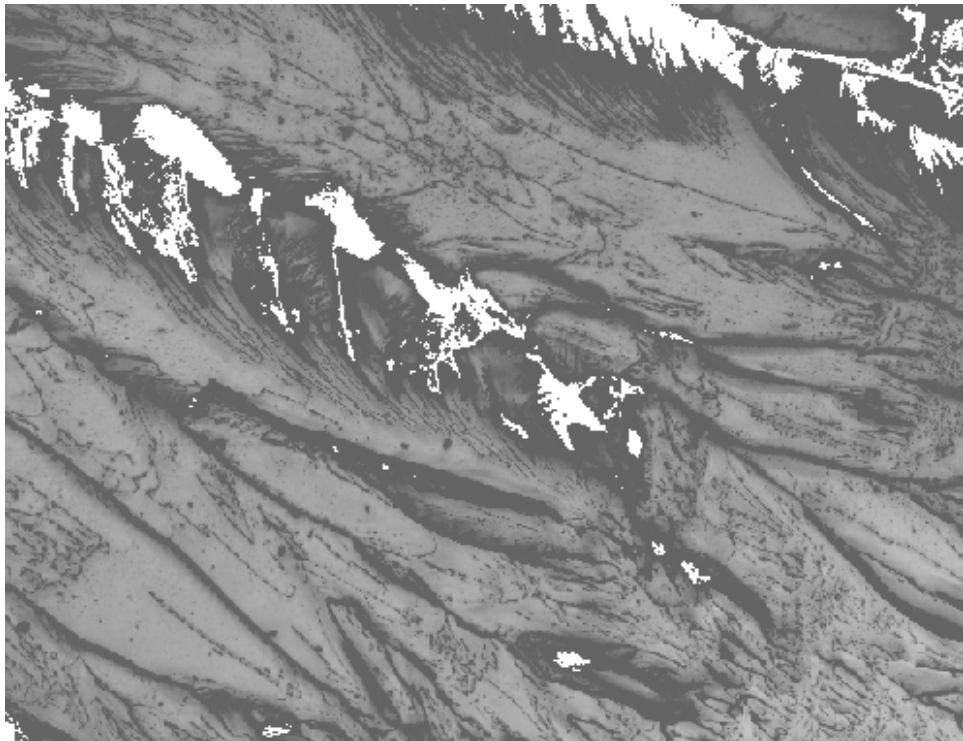


Figure 4-19 50-255 Elevation Image Section

4.3.3.4 Hand calculations of fractal dimensional increment

In order to confirm the data gathered using the Image-Pro software, a sample was characterized by hand using the Richardson Method. Figure 4-20 is a subsection of Figure 4-19. The contrast was enhanced and the section magnified to make hand measurements easier. Additionally the interior parts were removed to produce a more simple perimeter. The pixilation of the figure below is due to the fact that it is a very large magnification of a small section of Figure 4-19.

The image in Figure 4-19 was characterized for fractal dimension by hand. The image was magnified to a sufficiently large size and then printed. The perimeter of the white portion of the image was measured from four separate starting points, approximately 90 degrees apart. Table 4-10 is the data gathered in this process. Additionally Figure 4-21 is the plot of the natural log of the ruler length versus the natural log of the perimeter. The fractal dimension of this image can be determined from equation 4-4.

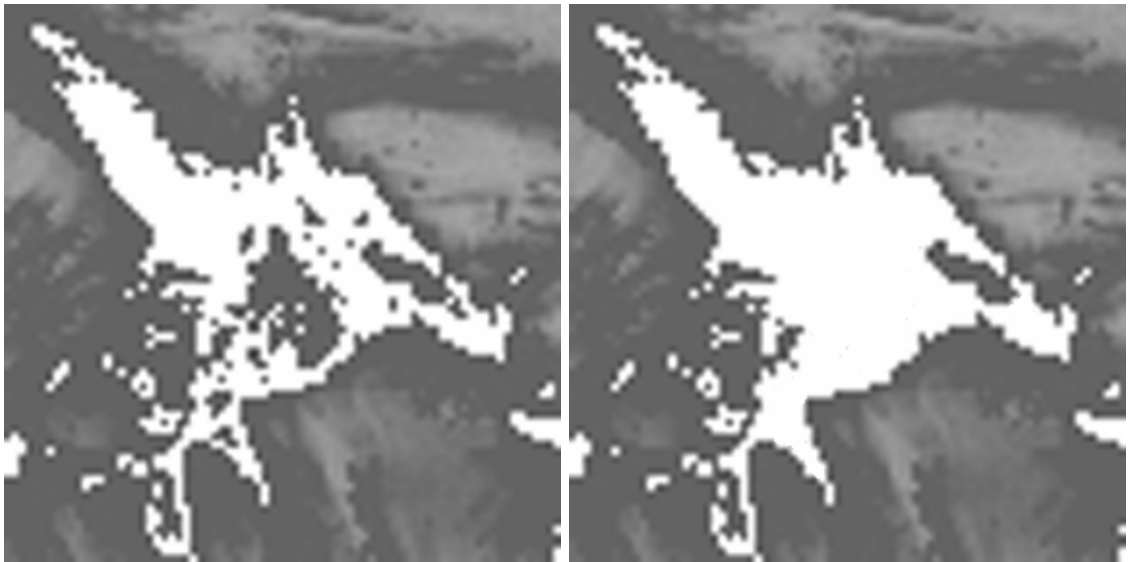


Figure 4-20 Magnification of Fracture Surface

$$(4-4) \ln(P) = (1-D)\ln(R) + C$$

Where R is the ruler length, P is the perimeter, D is the fractal dimension, and C is a constant.

Table 4-10 Hand Measurements of Fractal Dimension

Ruler	Number of Steps				Ave	Per	Ln R	Ln P
	1	2	3	4				
10	6	5	4	4	4.8	47.5	2.30	3.861
9	6	5	4	6	5.3	47.3	2.20	3.855
8	6	5	6	7	6.0	48.0	2.08	3.871
7	8	7	8	7	7.5	52.5	1.95	3.961
6	9	8	9	9	8.8	52.5	1.79	3.961
5	11	11	11	10	10.8	53.8	1.61	3.984
4	14	14	14	14	14.0	56.0	1.39	4.025
3	21	21	19	18	19.8	59.3	1.10	4.082
2	34	37	35	36	35.5	71.0	0.69	4.263
1	76	74	77	78	76.3	76.3	0	4.334

Fractal Dimension of Fracture Surface

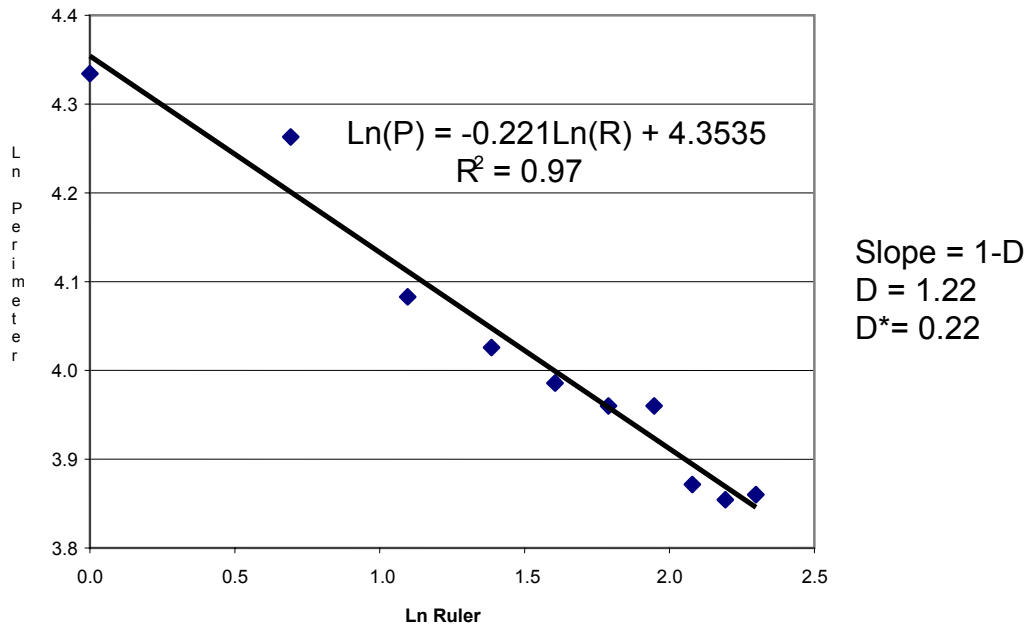


Figure 4-21. Richardson Plot of Perimeter of Fracture Surface

Three sub-sections for each of the six parameters tested in this research were measured for fractal dimensional increment using hand calculations on images generated

by the non-destructive slit-island method. These D^* values for each subsection, and the average and error for each composition and strain rate can be found in the Table 4-11.

Table 4-11. Hand Calculations of Fractal Dimension of Epoxy Resins

Section	8 phr DETA			10 phr DETA		
	0.1mm	10mm	100mm	0.1mm	10mm	100mm
1	0.23	0.21	0.15	0.20	0.18	0.15
2	0.21	0.18	0.19	0.21	0.15	0.12
3	0.22	0.15	0.16	0.25	0.16	0.12
Average	0.22	0.18	0.17	0.22	0.16	0.13
Error	5%	17%	12%	5%	9%	17%

The values in the above table are similar to those found previously when comparing the flaw to mirror size in Section 4.3.3.2. Fractal dimensional increment for all samples appears to be around 0.2. A plot of K_{Ic} vs. $D^{*1/2}$ for the fractal dimensions found by hand calculations can be found in Figure 4-22. Note the higher R^2 value for a linear regression in this plot versus Figure 4-12

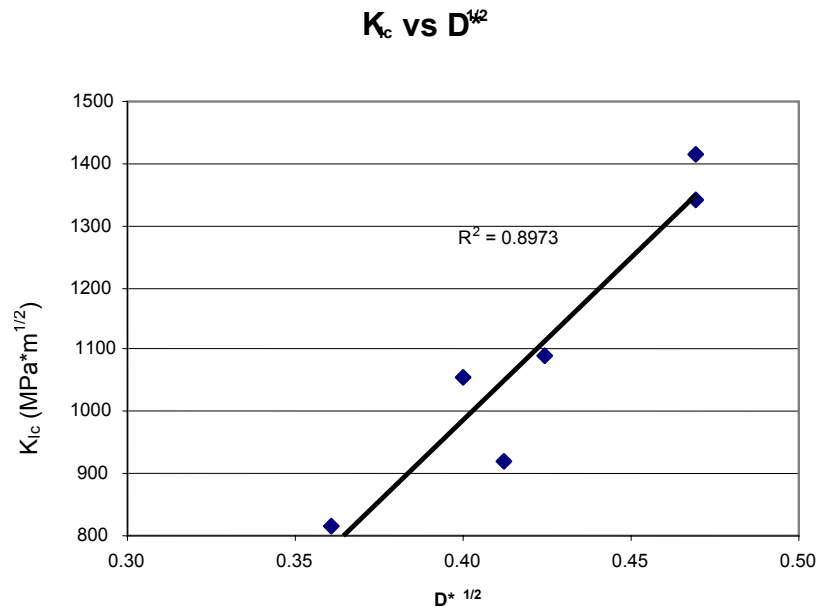


Figure 4-22 Square Root of Fractal Dimension vs. Toughness Calculated by Hand from Slit Island Contours

4.3.3.5 Calculation of fractal dimensional increment by Image-Pro

The hand calculations of fractal dimension can be extremely time-consuming and difficult. For that reason, software was employed to gather fractal dimension across large volumes of data. The fractal dimensional increment was calculated from images generated using the non-destructive slit-island method. “Image-Pro” software was used to calculate fractal dimension for all specimens for all samples. Image-Pro uses a derivation of the Richardson method to calculate fractal dimensional. Image-Pro first analyzes the image for light and dark regions to identify islands. Multiple ruler lengths are used to measure the perimeter in accordance with the Richardson method. Fractal dimension is calculated for regions with a perimeter larger than 30 pixels because the specific algorithm used by the software breaks down for very small features. The data was then tabulated and averaged together across all regions for a sample to produce a fractal dimension for a surface.

For each composition and strain rate, the images were used to obtain an average fractal dimension. Table 4-12 lists the average fractal dimension and error of each composition and strain rate for epoxy resins.

Table 4-12. D* of Epoxy Resins Calculated With Image Pro

Strain Rate	8 phr DETA		10 phr DETA	
	D*	%Error	D*	%Error
0.1	0.22	12%	0.23	13%
10	0.19	13%	0.17	17%
100	0.18	9%	0.16	11%

Finally, the square root of the fractal dimensional increment calculated with Image pro for images generated with optical microscopy was plotted versus the toughness of epoxy resins. This result can be found in Figure 4-23.

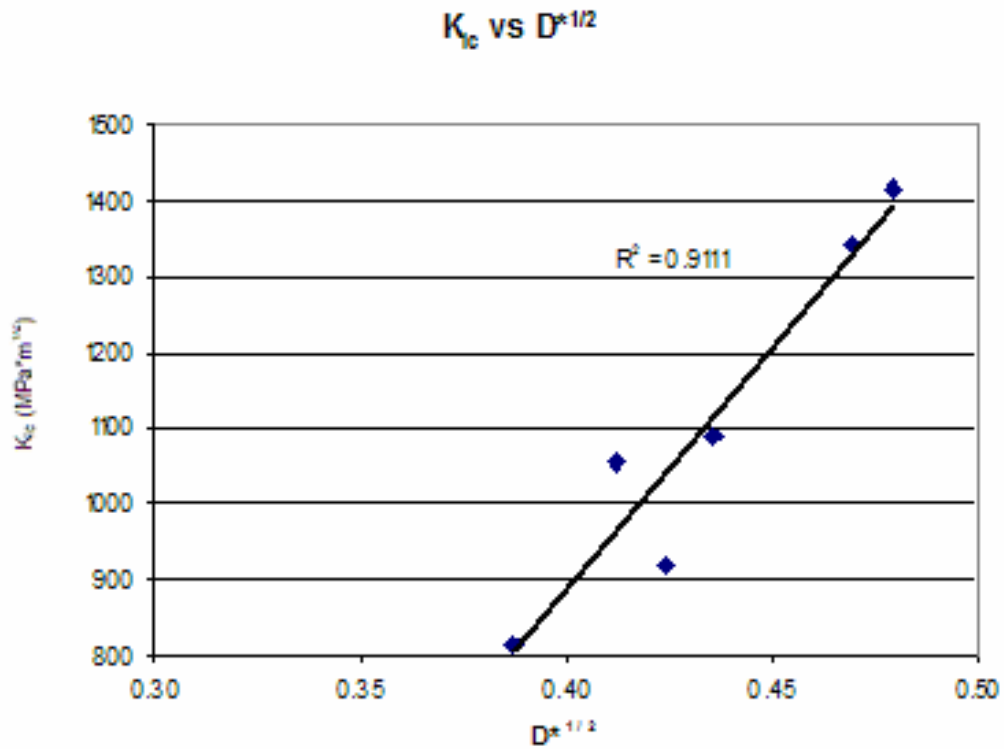


Figure 4-23 Square Root of Fractal Dimension vs. Toughness Calculated by Image Pro from Slit Island Contours

4.3.3.6 Comparison of methods of measuring fractal imension

Three separate methods were used to calculate fractal dimension for samples in this research; flaw to mirror ratio (F-M), hand calculations of slit island contours (Hand), and computer calculations of slit island contours (Computer. The results of these three methods are tabulated in table 4-13.

Table 4-13. Comparison of Fractal Dimensional Increment D^* Values for Different Methods

Methods	8 phr DETA			10 phr DETA		
	0.1mm	10mm	100mm	0.1mm	10mm	100mm
F-M	0.23	0.15	0.15	0.24	0.22	0.11
Hand	0.22	0.18	0.17	0.22	0.16	0.13
Computer	0.22	0.19	0.18	0.23	0.17	0.15

It can be seen in the above table that all three methods return similar values for each composition and strain rate.

4.4 Structural Parameter a_0

The goal of this research was to determine the nature of the relationship of nodular size and toughness. It was proposed that nodular size could be related to toughness through the West Mecholsky Passoja theory. Using the data presented above, it is possible to calculate the WMP structural parameter, a_0 , and the relationship to nodule size for epoxy resins investigated in this research.

4.4.1 Calculating a_0

The structural parameter of the West Mecholsky Passoja theory, a_0 , can be calculated from the modulus, fractal dimensional increment, and toughness using the following equation:

$$(4-5) \ a_0 = \left(\frac{K_{Ic}}{E} \right)^2 * \frac{1}{D^*}$$

Where K_{Ic} is the toughness, E is the modulus, and D^* is the fractal dimensional increment. The structure parameter for all three strain rates and each composition can be found in the following table:

Table 4-14. Calculated a_0 values (μm) for Epoxy Resins

Strain Rate (mm/min)	8phr DETA	10 phr DETA
0.1	4	5
10	4	4
100	3	3

The data used to calculate these results are the average values for a particular composition and strain rate. The fractal dimensional increment values used in this calculation come from calculations with Image Pro. These values were chosen because of

the low error for the measurements made. Because the error associated with a_0 is a function of the individual variables and not a direct summation, Appendix A has been prepared describing how the error was calculated. Additionally Section 4.4.3 describes statistical significance of these results.

4.4.2 Relationship of Fractal Dimensional Increment to a_0

Through the course of measuring fractal dimensional increment, several plots were derived that plotted the square root of D^* versus the toughness of epoxy resins. The figures are 4-12, 4-22, and 4-23. These types of graphs have been reported in the literature to show that for families of materials, such as glasses, or crystalline materials, the fractal dimensional increment follows a trend that as toughness increases so does D^* . Additionally, it has been hypothesized that these graphs would extrapolate through zero.

The data in Figures 4-12, 4-22, and 4-23 were extrapolated back through zero; these results can be found in Figure 4-24. The data in Figure 4-24 seems to indicate that the flaw to mirror size ratio is the best method of calculating D^* . Even though the error is very high compared to other methods, the flaw to mirror ratio best fits predicted models for fractal dimension to toughness. This argument is made based on the fact that when extrapolates the data for all three techniques through zero, the R^2 value for flaw to mirror ratios is the highest (0.7311), as evidenced on the next page.

The data in Figure 4-24 serves a second purpose, not only can it help to better understand where problems in measuring fractal dimension occur, but also the slope of the linear regression line can be used to calculate a_0 . The slope of a plot of $D^{*1/2}$ versus K_{Ic} should be equivalent to $Ea_0^{1/2}$. Table 4-15 lists the a_0 values calculated by comparing the slope of the regression line to the modulus of epoxy resins.

Comparison of Fractal Dimensional Increments

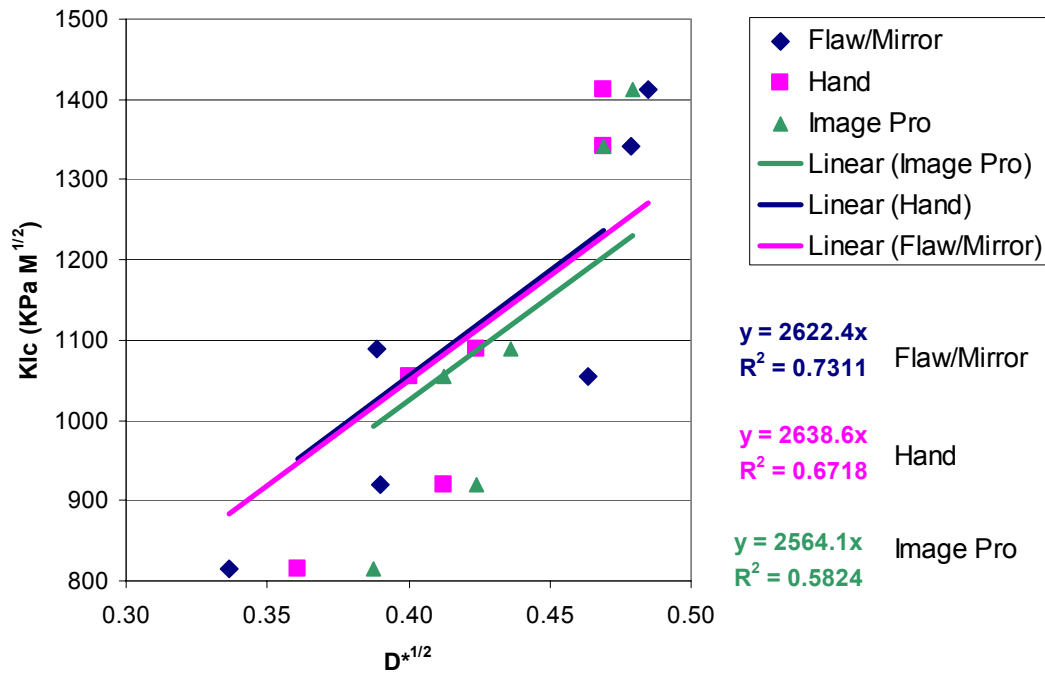


Figure 4-24 Comparison of Fractal Dimension Increment to Toughness for Three Different Techniques of Measuring

Table 4-15 a_0 Values (μm) calculated from the Slope of the Fractal Dimension vs. Toughness Plot

Strain Rate(mm/min)	8phr DETA	10 phr DETA
0.1	4	4
10	3	3
100	3	3

The values of a_0 are similar to those calculated from the data gathered in this research using equation 4-5. This would seem to further indicate that there is no strain rate component to a_0 . However, the calculated values of a_0 are still significantly higher than nodule size. As previously mentioned the nodule size for the investigated compositions ranges between 75 and 100 nm, the calculated values of a_0 are well over one order of magnitude larger. Additionally it should be noted that a_0 values are identical for both compositions, even though the nodule sizes are different.

4.4.3 Error Analysis of a_0

The West Mecholsky Passoja theory is a complex equation that requires several measurements to be made. Each measurement has its own error, which can be the result of many factors such as machine compliance and user specific error. As a result, the cumulative error for calculation of a_0 can not be calculated from directly summing the error of the individual measurements. The individual errors for each variable in the WMP theory must be weighed for their magnitude and power in the equation. As previously mentioned, Appendix A has been prepared to describe how error was calculated and also describes the individual contribution of each variable on the final value of toughness or a_0 . Table 4-16 list the error for each composition and strain rate tested in this research.

Table 4-16 Cumulative Error Values for a_0 Calculations for Epoxy Resins

Strain Rate	8phr DETA	10 phr DETA
0.1	53%	44%
10	68%	61%
100	44%	74%

The cumulative errors associated with calculated a_0 from the data presented are very large. As such, one can only make the judgment that there is no statistical difference between the a_0 values calculated for one strain rate to another. Additionally, it is also apparent that the error in the strain rate values for the two DETA compositions are the same. Each composition has a different strain rate, however this data would seem to indicate that a_0 is not a function of nodule size.

4.5 Results and Discussion

The data found in the various studies in this research is similar to what can be expected from the literature ($K_{Ic} \approx 1.5 \text{ MPa}\cdot\text{m}^{1/2}$, $E \approx 1.5 \text{ GPa}$, $D^* \approx 0.2$, Nodule Size $\approx 100 \text{ nm}$). The value of a_0 was found to be around $4 \mu\text{m}$, which is significantly larger than

nodule size. While the cumulative error of a_0 as listed in Table 4-16 may be very large, it should be noted that calculated values of a_0 are almost two orders of magnitude greater than nodule size, and would be almost three orders of magnitude larger than the interstitial formed by nodule packing. As such, it can be concluded that there is no direct relation between nodule size, nodule packing, and a_0 , which is contrary to our initial hypothesis.

Table 4-17. Calculated a_0 Values and Associated Error

Strain Rate	8 phr DETA		10 phr DETA	
	$a_0(\mu\text{m})$	%Error	$a_0(\mu\text{m})$	%Error
0.1	3.9	53%	5.2	44%
10	3.8	68%	3.8	61%
100	3.3	61%	2.6	74%

There are a few possible explanations for this result. First and foremost it could be that nodule size simply does not relate to toughness in any meaningful way. Literature has shown that as the nodule size changes cross-link density also changes, which has been shown extensively to relate to toughness for other polymeric systems.(Racich et al. 1976) It could be that toughness is only controlled by cross-link density. As previously mentioned, previous research has reported that nodules and interstitial material have the same density and modulus. Therefore, it could mean that nodules are merely an artifact of the polymerization reaction and do not positively or adversely affect toughness. Another possible explanation can be found from the results of the nodule extraction study.

As mentioned above and in the literature, acetone and other solvents can be used to swell the epoxy resin and wash nodules out of the structure. However not all nodules wash out of the structure, only a very small percentage. The structural parameter, a_0 can be linked to the weakest link theory of failure. When a body is stressed, failure occurs at

the weakest link; in the case of the WMP theory, the fracture tip propagates through the weakest links. One possible explanation for why a_0 is so large could stem from the fact that not all nodules are tightly bound to the structure. As the crack tip propagates through the sample, it paths along between weakly or unbound nodules in the bulk.

Additionally it should be noted that the sub critical crack growth found as part of the flaw size measurements has not been previously shown to occur in homogenous epoxy resins. This phenomenon is usually found in heterogeneous materials such as composites where R-curve behavior can occur. It is possible that individual nodules serve as points for crack tip deflection, the chief mechanism for toughening in composites.(Watchman 1996) This lends further credence to the belief that there are structural inhomogeneities such as free or loosely bound nodules that might contribute to the a_0 parameter.

4.6 Conclusions

The original hypothesis of this work was that a_0 can be related to nodule size, however the results indicate that there is no relation between these two values. While the hypothesis was shown not to be valid, this work has opened up some possible avenues to investigate further. It could be further postulated that a_0 may not be directly related to nodule size, but is a function of concentration of loosely bound nodules. Researchers have shown that there is a very low concentration of nodules that are not tightly bound to the resin and can be washed out of the structure with extended exposure to solvents. It is possible that a_0 is a function of the average distance between weakly or unbound nodules.

Additionally part of this research focused on developed a new adaptation of the slit island method for producing contours for calculating fractal dimension. Contours were produced using optical microscopy and characterized using hand and computer

calculations. The values calculated from the optical microscopy contours were compared to fractal dimensions derived from the ratio of mirror to flaw size of fracture surfaces. The values for both techniques were found to be similar to one another. This means that optical microscopy can be used to calculate fractal dimension of fracture surfaces.

CHAPTER 5
SILSESQUIOXANES: GROWTH, STRUCTURE, AND CHARACTERISTICS

5.1 Introduction

Silsesquioxanes are technologically important hybrid inorganic-organic polymers. Polysilsesquioxanes have been used in everything from microelectronics to scratch-resistant coatings. Chemically they are similar to polysiloxanes or silicone, with a backbone of silicon and oxygen and an organic side groups; they differ in that polysilsesquioxanes have one organic group while polysiloxanes have two. The general structures of a polysilsesquioxane and polysiloxane are compared in Figure 5-1.

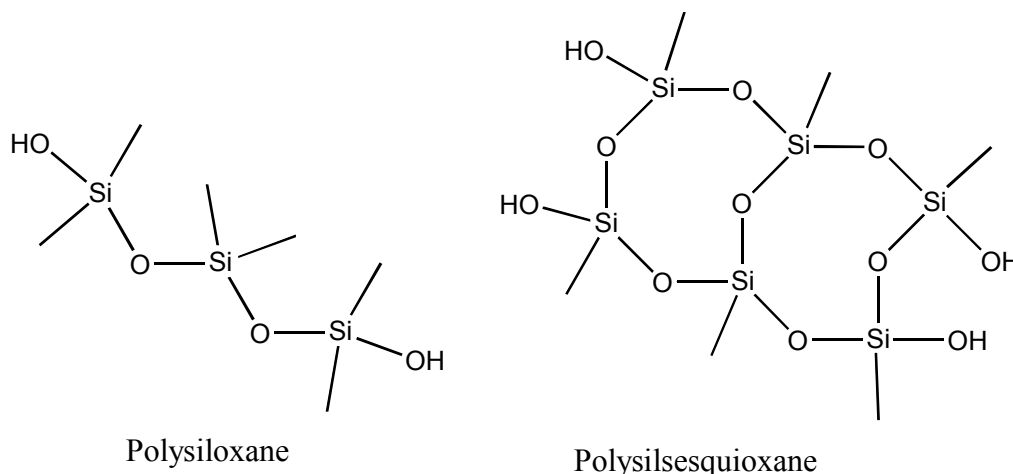


Figure 5-1. Comparison of Silicone and Polysilsesquioxane Structures

There are many different types of polysilsesquioxanes. Polysilsesquioxanes are classified by their organic group. A methyl polysilsesquioxane is one that contains a CH_3 group, a phenyl polysilsesquioxane contains a C_6H_5 group and so forth. The properties, uses, and structure of a polysilsesquioxane are dependent on the organic group. Table 5-

1 lists some of the more common polysilsesquioxanes and gives the common use and structure.

Table 5-1. Usage of Common Polysilsesquioxanes

Silsesquioxane	Usage
Hydrido	Interlayer Dielectrics
Methyl	Additive, Binder, Precursor
Phenyl	Coatings, Precursor

Silsesquioxanes are synthesized from trifunctional monomers. This results in a complex non-linear polymer. Many possible structures can be formed from polysilsesquioxanes. There are generally three classes of polysilsesquioxane structures: random network, cage, and ladder, as found in Figure 5-2. It should be noted, however, that the ladder structure has almost exclusively been shown to be only found in the phenyl polysilsesquioxane polymer.

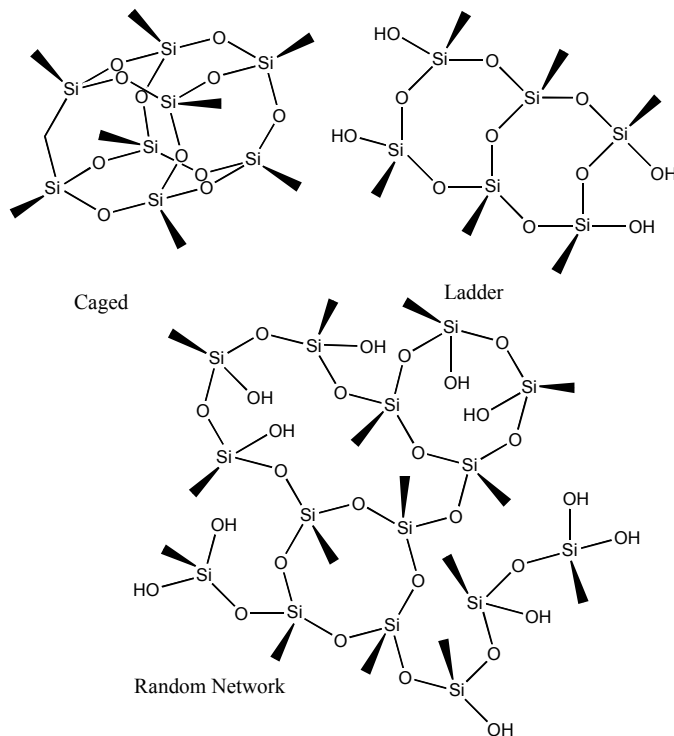


Figure 5-2. Common Polysilsesquioxane Structures

An independent study performed by Cao and Baney indicated that bulk polysilsesquioxanes have a nodular microstructure similar to what is found in epoxies. These results have not been reported or duplicated elsewhere, this is mostly due to the fact that polysilsesquioxanes are very rarely ever studied as bulk resins. Traditionally, polysilsesquioxanes are used as thin films or as fillers in other polymers. This research will build on the work of Cao and Baney by investigating what parameters influence the formation of nodules in polysilsesquioxanes.

This research was broken down into two distinct portions, characterization of the polymerization process, and characterization of cross-linked polysilsesquioxane monoliths. The polymerization process was investigated for effects on physical properties such as viscosity and molecular weight, and chemical properties such as structure. The cross-linked monoliths were investigated for nodular microstructure as seen in the epoxies and methods of formation.

5.2 Polysilsesquioxane Synthesis and Processing

5.2.1 Polymer Synthesis

Silsesquioxanes are synthesized using many different techniques. All polysilsesquioxanes studied in this research were synthesized in the same manner using a novel two phase reaction technique that has been reported in the literature.(Kondo et al. 2000) The Itoh method for synthesizing polysilsesquioxanes uses a hydrogen bonding solvent, such as a ketone, to direct the condensation reaction. The ketone used in the Itoh method hydrogen bonds to the hydroxide groups of the hydrolyzed monomer.

Silsesquioxanes were prepared using alkyltrichlorosilanes purchased from Gelest Inc. The ratio of silane to water was held constant for each polysilsesquioxane, 1.5 moles silane to 600 ml of water. A solution of 1.5 moles of silane and 75 ml of methyl isobutyl

ketone (MiBK) was dripped into a vigorously stirred mixture of 600ml of water and 450 ml of MiBK in a 2-liter, 3-necked round-bottomed flask. The water-MiBK mixture was held at 10°C while the alkyltrichlorosilane-MiBK mixture was added over the course of one hour. After the monomer was added, the solution was heated to a desired growth temperature, usually 50°C and stirred for 3 additional hours.

Table 5-2 Synthesized Polysilsesquioxanes and Structures

R-Group	Name	Polymer	Structure
-CH ₃	Methyl	PMSQ	
-C ₂ H ₅	Ethyl	PESQ	
-C ₃ H ₇	Propyl	PPSQ	
-C ₄ H ₉	Butyl	PBSQ	
-C ₂ H ₃	Vinyl	PVSQ	
-C ₃ H ₆ Cl	Chloropropyl	PCPSQ	

Upon completion of the growth phase, the ketone-water mixture was removed from the flask and separated. The ketone phase, containing the polysilsesquioxane polymer, was then washed repeatedly to neutral using deionized water, which was done to remove the large excess of hydrochloric acid that is a byproduct of the reaction process. Excess MiBK was removed using vacuum distillation. The purified polymer was then removed for characterization and further use. Six polysilsesquioxanes were synthesized in this research. Table 5-2 is a list of the polysilsesquioxanes synthesized in this research and the structure of each monomer used.

5.2.2 Polysilsesquioxane Monolith Synthesis

The polysilsesquioxanes synthesized in this research were cross linked to form freestanding monoliths. Tin octoate was used as a catalyst to cross-link the polysilsesquioxanes through a condensation reaction. Before cross-linking, the polysilsesquioxanes were diluted with a solvent, and the tin octoate was dissolved in a matching solvent. Solvents used in this portion of the research include chloroform, acetone, carbon tetrachloride, and hexane.

The ratio of polysilsesquioxane to solvent and the concentration of tin octoate were varied. Additionally the substrate upon which the polysilsesquioxane was cured was also investigated. Two substrates were investigated in two geometries, glass and Teflon in single and double sided configurations. These configurations are found in figure 5-3.

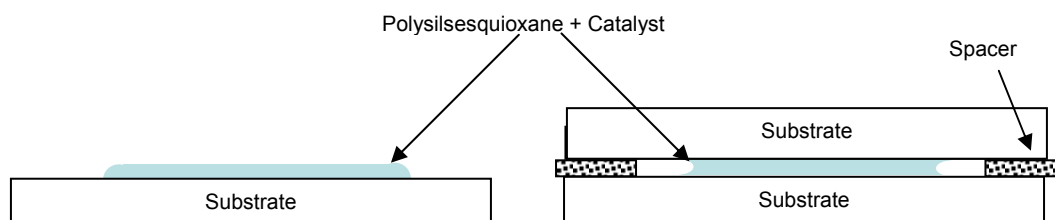


Figure 5-3 Substrate Configurations.

5.3 Experimental

5.3.1 Characterization of Polymer

5.3.1.1 Viscosity

Viscosity of polysilsesquioxane polymer in ketone was measured as the polymer was grown at elevated temperatures as part of the synthesis process. An Ubbelohde kinematic viscometer was used to collect viscosity data. Figure 5-4 is a representation of an Ubbelohde viscometer.

The viscometer is loaded by filling the lower chamber A, and then charged by applying a vacuum to tube D. The viscometer is fully charged when the liquid level is above line F. The vacuum is removed and the liquid is allowed to flow back down through chamber B and back into chamber A. Viscosity is calculated by taking the amount of time it takes for the liquid level to pass from Line F through Line G and multiplying the time by a constant inherent to the viscometer used. A type 1 viscometer was used; the constant for this model is 0.1 cSt/s.

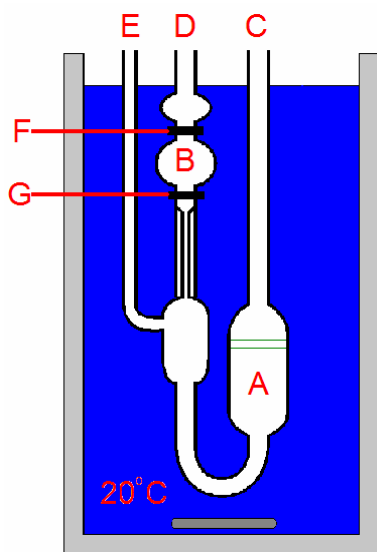


Figure 5-4 Schematic of Ubbelohde Viscometer

Samples were removed from the ketone-water-silsesquioxane material and cooled to room temperature. The water was removed from the sample and the viscosity of the organic phase was measured. Samples were taken every 30 minutes from the start of the drip of the silane into the water and ketone, and a total of 9 data points were taken for each polysilsesquioxane synthesized. Each sample was measured three times to average out an error.

Polymethylsilsesquioxane samples were characterized for viscosity. Viscosity has long been used to study polymerization reactions of linear polymers as a way to indirectly measure molecular weight. In this study, viscosity was used to gauge the effects of aging temperature on polysilsesquioxanes grown using the Itoh method. Figure 5-5 is the viscosity of polymethylsilsesquioxane. Three separate batches of polymethylsilsesquioxanes were synthesized with different aging temperatures, 40°C, 50°C and 60°C. The right portion of the graph is the initial addition phase, where the chlorosilane-ketone solution is dripped into the flask. All three samples have very similar viscosity measurements through the addition phase, which follows a linear trend. However, upon heating the sample to the growth temperature, the viscosity greatly changes from batch to batch. All three samples follow a logarithmic increase in viscosity with time. Normally one would expect the condensation rate of a sol-gel reaction like this in the Itoh method to increase with increasing temperatures.

The results in Figure 5-5 are somewhat surprising. It is apparent from the graph that increased growth temperature decreases viscosity, which is contrary to the popularly held belief that increasing temperature increases reaction rates. There are two possible explanations for this result.

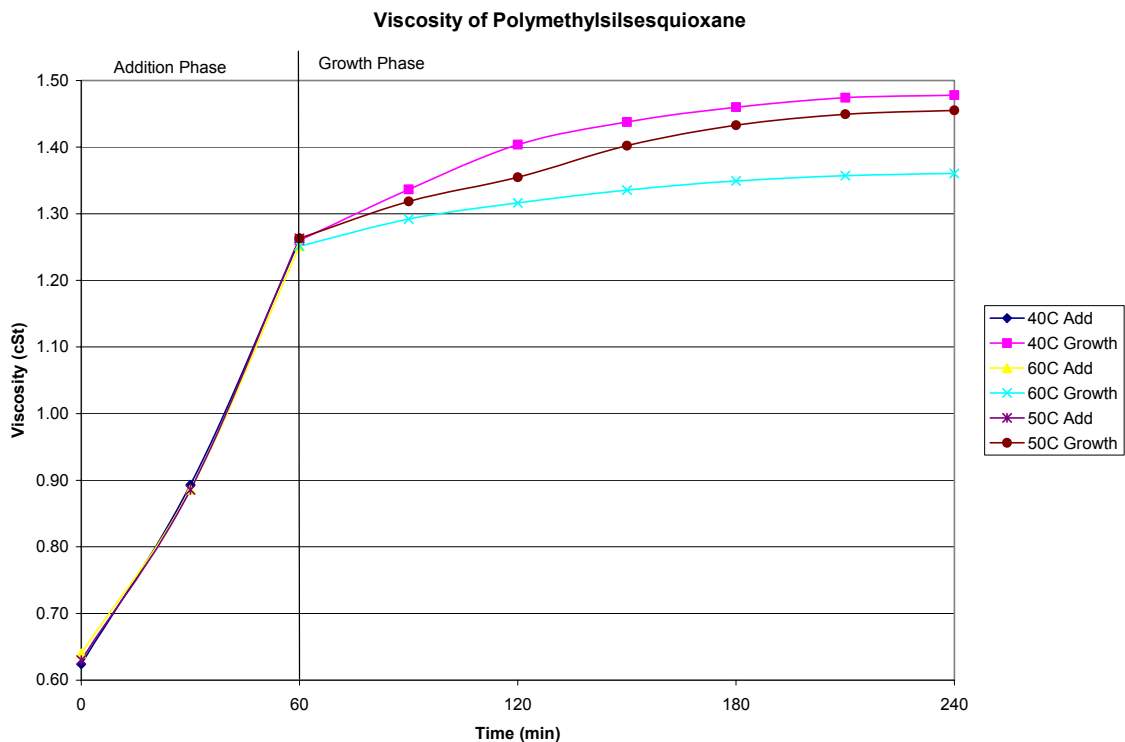


Figure 5-5. Viscosity of Polymethylsilsesquioxane

Because polysilsesquioxanes are network polymers, two different condensation reactions can occur; intermolecular condensation, where two separate molecules condense to become one, or intramolecular condensation, where two functional groups on one molecule condense. It is possible that at higher temperatures the polysilsesquioxane molecules have more mobility and the ability to bend back on themselves more easily, resulting in an increase in intramolecular condensation. With an increase in intramolecular condensation, one would expect a lower molecular weight. Additionally intramolecular condensation consumes hydroxide groups in the polymer, which should result in the polymer molecule becoming more hydrophobic and more soluble in the organic ketone phase. It has been postulated that the ketone phase mediates condensation reactions, removing the polymer from the water phase when the polymer becomes more

hydrophobic. In the ketone phase one would expect condensation reactions to be reduced by virtue of ketone hydrogen bonding to the hydroxides blocking reaction sites.

There is another possible explanation for the lower viscosity of polysilsesquioxanes with increasing temperature. At room temperature water is only slightly soluble in MiBK, however as temperature increases, the solubility of water in MiBK increases. Figure 5-6 is the solubility of water in MiBK with temperature. It serves that as water becomes more soluble in MiBK with higher temperatures, polysilsesquioxanes with high amounts of hydroxide would also become more soluble in the ketone. One could assume that the higher temperatures result in lower molecular weight hydroxide rich polysilsesquioxanes dissolving into the ketone phase more quickly, where the reaction slows down. The result of this would be that the viscosity of the polysilsesquioxane polymer would be decreased.

It is unclear from the viscosity measurements alone which of these concepts are the proper explanation of the unique results found in Figure 5-6. It is possible that both of these phenomena are occurring simultaneously. An investigation of the molecular weight and structure could give a better indication of what is happening for future research.

5.3.1.2 Matrix assisted laser desorption ionization

Matrix assisted laser desorption ionization (MALDI) is a relatively new technique for accurately measuring the molecular weight of high mass molecules. Traditionally this technique has been reserved for proteins and other bio-molecules. Recent research has used MALDI for various polymers, including polysilsesquioxanes.

MALDI functions by precipitating the material that is to be analyzed in a matrix. The sample is then irradiated with a laser, which is preferentially absorbed by the matrix

rather than the analyte. The energy absorbed from the laser causes the matrix to vaporize taking some of the analyte with it. Additionally at this point the matrix serves to ionize the analyte, usually by transferring a sodium ion to the material being studied. After desorption and ionization the analyte is then subjected to an electric field which accelerates the ion towards the detector. The amount of time it takes for the ion to reach the detector is proportional to the mass of the ion. The data from MALDI can be matched up exactly to various possible structures of the analyte, which makes it an extremely powerful tool for protein synthesis and polysilsesquioxanes.

The most difficult part of MALDI is proper selection of the matrix in which to disperse the sample. The matrix selected for this research was sinapic acid. Samples were prepared in a manner similar to that found in the literature. (Falkenhagen et al. 2003) A solution of sinapic acid in tetrahydrofuran (THF), 10 $\mu\text{g/ml}$, was added to an equivalent volume of a solution of polysilsesquioxane in THF, 1 $\mu\text{g/ml}$. 100 μl of the sample was placed drop-wise on the surface of the MALDI sample plate and allowed to dry. The samples were irradiated using a nitrogen laser ($\lambda = 337 \text{ nm}$) with a 20 kV acceleration voltage, 100 pulses were acquired for each spectrum.

Matrix Assisted Laser Desorption Ionization Time of Flight Mass Spectroscopy (MALDI-TOF MS) was used as a method to calculate molecular weight of synthesized polysilsesquioxanes. This technique was chosen over gel permeation chromatography due to its higher accuracy in calculating molecular weight for complex polymers and polysilsesquioxanes, as described in Chapter 3.

The matrix employed in this research is identical to the one described in the literature. (Falkenhagen et al. 2003) It was found that MALDI is not an applicable

technique for the polysilsesquioxanes synthesized here. The polysilsesquioxanes synthesized as part of this research have a vary large molecular weight distribution, similar to those studied by Tecklenberg. (Tecklenburg et al. 2001) However unlike Tecklenberg's work, the polysilsesquioxanes studied here were not fractionated. As such, the amount of signal from any one molecular weight species was too low in comparison to the background.

For this research, the molecular weight was not possible to determine. It should be noted, however, that most of the polysilsesquioxanes synthesized in this work were visually similar. In other words, they were transparent and free of particles. Polymethylsilsesquioxane was opaque, additionally after sitting, small white particles would settle on the bottom of the flask. Furthermore, distillation of the other polysilsesquioxanes resulted in high viscosity liquids, whereas the polymethylsilsesquioxane would form a solid mass upon cooling down.

5.3.1.3 Nuclear magnetic resonance

Nuclear magnetic resonance (NMR) was employed to determine the relative amounts of hydroxide functionalized silicon groups in each silsesquioxane. NMR has been extensively used in all fields of chemistry to characterize the nature of compounds and reactions. NMR is a chemically sensitive technique in that it can be used to determine the local chemical environment of a particular group or functionality of a sample.

NMR functions by aligning the nuclear spins of all the atoms in a sample using a very powerful magnet. With all the spins pointing in the same direction, a radio pulse is used to knock the spins over. As the nuclei return towards alignment with the magnetic field, a signal is given off that is indicative of the chemical nature of the particular atom.

The amount of shielding or de-shielding as a result of an atom being bound to another changes the chemical shift in an NMR Spectra.

Silicon 29 NMR was used to calculate the ratio of the T_2 group to the sum of the T_2 and T_3 peak in this research. For the purposes of this research and as a tradition in the field a T group is a silicon atom with 3 oxygens and one organic group bound to it. A T_2 group is one that has two bridging oxygens and one hydroxide, a T_3 group is one that has three bridging oxygens. Additionally a T_1 group and T_0 group are silicon atoms that have one or no bridging oxygen groups, respectively.

The NMR spectra were collected on a Bruker Avance 600 MHz Spectrometer with a 14.1 T/51mm Magnet and a 5mm BBO Probe non-spun at 27°C. The spectral width was 100ppm and ranged from -30ppm to -130ppm. A five microsecond pulse at 3dB was used to collect data at a frequency of resonant frequency 119.2 MHz. The acquisition time was 0.8585 seconds and the number of scans taken was 2048. A pulse acquire program was used with no decoupling on the hydrogen atom.

The samples were prepared using deuterated acetone as a solvent. Additionally some samples of silsesquioxanes were treated with bis-(Trimethylsilyl)acetamide (BTMSAA) to derivitize a portion of the hydroxide groups of the silsesquioxanes. Samples were treated with a ratio of 4-1 by volume of BTMSAA to silsesquioxanes.

All of the polysilsesquioxanes studied had two peaks, T_2 and T_3 . Because polysilsesquioxanes are polymeric materials, the NMR spectra are not simple neat spectra with sharp narrow lines. The NMR peaks in polysilsesquioxanes and other polymeric materials are often broad humps or collections of peaks. For the alkyl polysilsesquioxanes the T_2 peak was defined as the range of peaks between -52ppm and -

62ppm, and the T₃ peak was defined as the range of peaks between -62ppm and -72ppm. The T₂ and T₃ peaks for polyvinylsilsesquioxane were defined as -67ppm to -77ppm and -77ppm to -87ppm respectively.



Figure 5-6 Bruker Avance 600 Mhz Vertical Bore Spectrometer at MBI

Figure 5-7 is a composite image of all 6 silsesquioxanes characterized in this study. All spectra were gathered using the same conditions as described above. Additionally Table 5-3 is an accumulation of the integrated values for the T₂ and T₃ peaks. For all spectra the integral of the T₃ peak was set to one. The hydroxide content was found from the following formula:

$$(5-1) \%OH = \frac{[T_2]}{[T_2] + [T_3]} * 100$$

Assuming an inherent error of 5% in the processing of NMR spectra, the total hydroxide for ethyl through chloropropyl silsesquioxane can be taken to be nominally equivalent. Conversely, the hydroxide content for methyl silsesquioxane is significantly lower than the other five synthesized silsesquioxanes. This would indicate that there is a stearic component to the polymerization process. The methyl group is significantly smaller than the other five groups investigated. It is likely that the methyl silsesquioxane can condense and cross-link to a much higher degree than any of the other

silsesquioxanes due to the ease with which the smaller structure can form various intramolecular conformations.

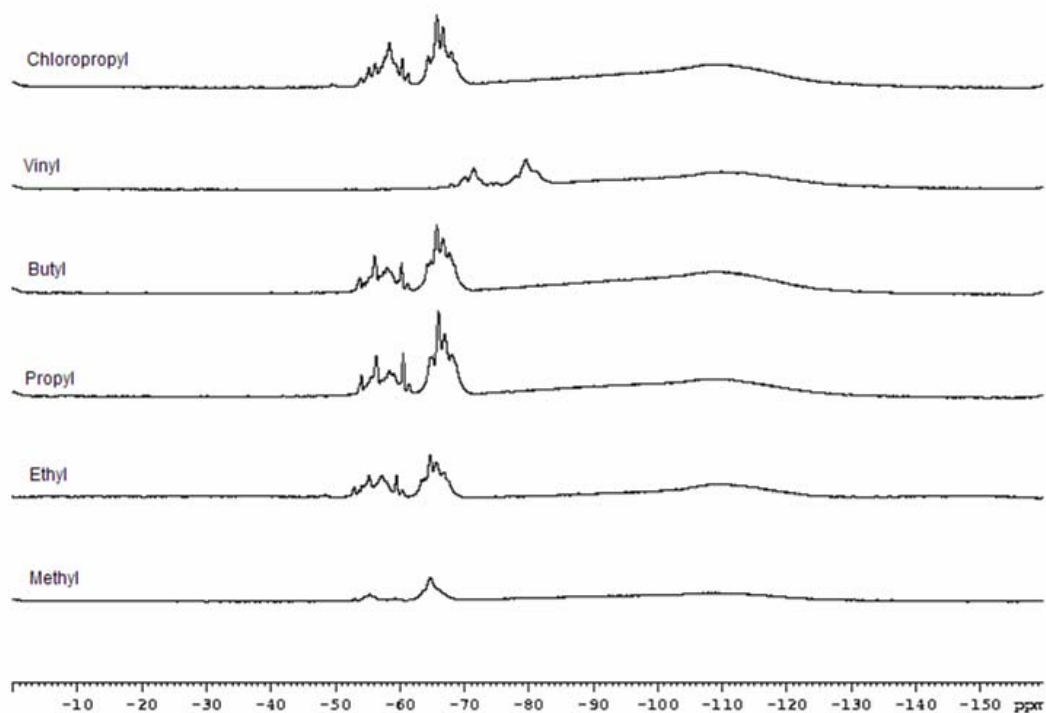


Figure 5-7. NMR Spectra of Synthesized Silsesquioxanes

Table 5-3. Total Hydroxide Content of Silsesquioxanes

PSQ	T ₂	T ₃	%OH
Methyl	0.271	1	21.32%
Ethyl	0.671	1	40.16%
Propyl	0.608	1	37.81%
Butyl	0.537	1	34.94%
Vinyl	0.614	1	38.04%
Chloropropyl	0.689	1	40.79%

A second set of NMR experiments were performed to investigate the structural nature of the hydroxide groups of the various silsesquioxanes studied. Silsesquioxanes were trimethylsilylated with bis(trimethylsilyl)acetamide (BTMSAA). Derivatization

attaches a trimethylsilyl group to a hydroxide group on a target molecule. Figure 5-8 is the structure of BTMSAA.

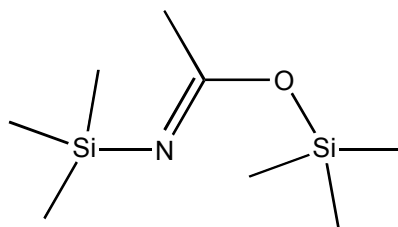


Figure 5-8. Bis(Trimethylsilyl)Acetamide Structure (BTMSAA)

Samples in this research were trimethylsilylated to determine the amount of reactive hydroxide of the synthesized silsesquioxanes. As previously mentioned silsesquioxanes are very complex, large molecules. It would be unreasonable to assume that all of the hydroxides in a silsesquioxane molecule are capable of further condensation reactions, such as those used to cross-link the silsesquioxane polymer into a monolith. Derivatization allows one to characterize the amount of hydroxides that are reactive, those that can react further, and non-reactive hydroxides, those that are not able to react further. Non-reactive hydroxides are ones that are likely trapped in a large, complex molecule and are unable to maneuver or configure in such a fashion that would easily allow condensation.

Samples were treated with a large excess of BTMSAA to derivatize the reactive hydroxides. Figure 5-9 is a composite image of the 6 derivitized silsesquioxanes. In this figure the BTMSAA consumes a portion of the hydroxides in the T_2 peak. This portion consumed is the reactive hydroxide. The remaining portion is the non-reactive hydroxide. For the purpose of this research the non-reactive hydroxides are ones that are defined as being locked within the structure of the polymer molecule, or unavailable to the rather large BTMSAA molecule

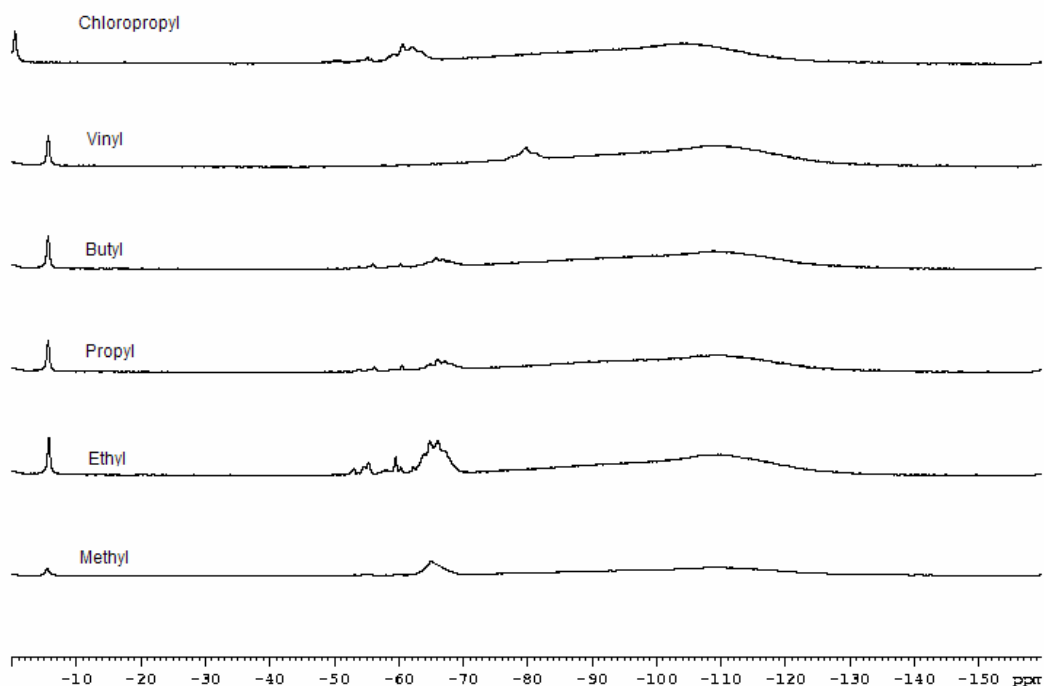


Figure 5-9. NMR Spectra of Trimethylsilylated Silsesquioxanes

The trimethylsilylated silsesquioxanes do not appear to follow any trends regarding reactive hydroxide content and R-group nature. Table 5-4 lists the reactive hydroxide content of each silsesquioxane.

Table 5-4. Hydroxide Content of Trimethylsilylated Silsesquioxanes

PSQ	T2	T3	%OH
Methyl	0.118	1	10.55%
Ethyl	0.244	1	19.61%
Propyl	0.363	1	26.63%
Butyl	0.347	1	25.76%
Vinyl	0.003	1	0.30%
Chloropropyl	0.129	1	11.43%

From these results it is very difficult to gauge what role the R group has on structure formation and guiding the ability of hydroxides to condense. Additionally

Figure 5-10 shows the percentage the total, reactive, and non-reactive silanol of each silsesquioxane.

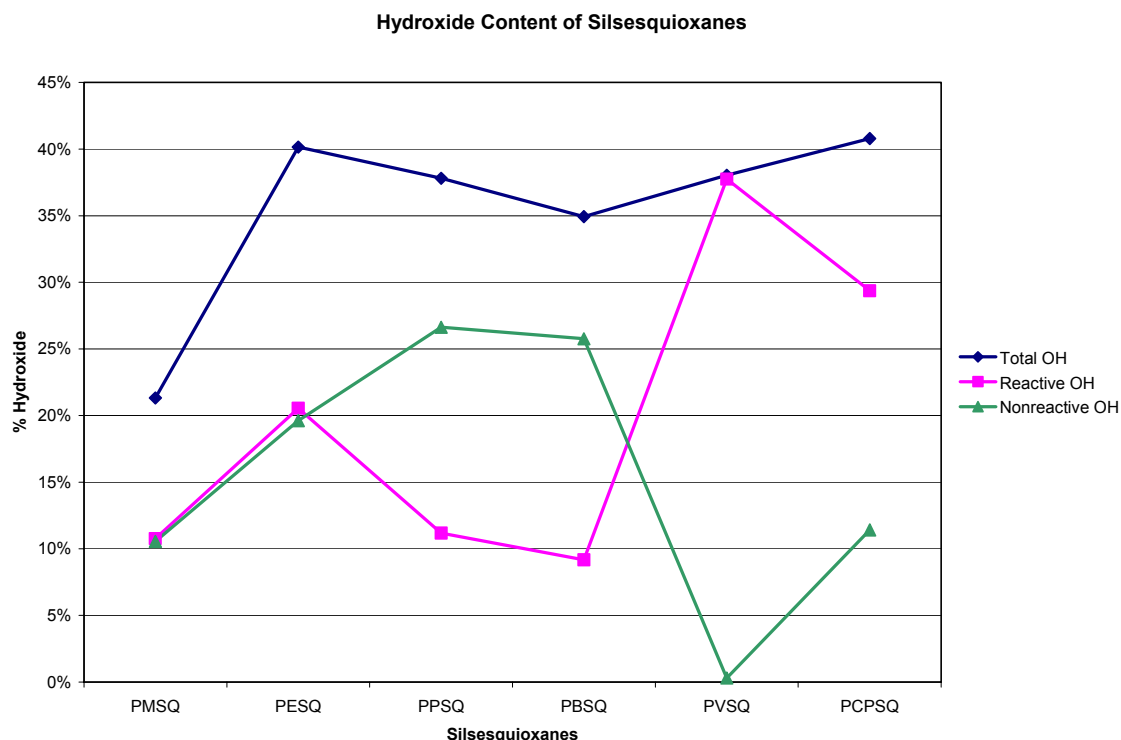


Figure 5-10. Total, Reactive, and Non-reactive Hydroxide Content of Silsesquioxanes

The figure above reveals no consistent trend in hydroxide content or nature among the synthesized silsesquioxanes. It is unknown at this time as to why that is the case. The most notable result of this investigation is the nature of the hydroxide of the polyvinylsilsesquioxane. It appears from the results that the hydroxide content of the vinyl silsesquioxane is entirely reactive, meaning the structure is very open. One possible explanation for this is that some form of long range order is present in the polymer, such as the previously described ladder structure found in polyphenylsilsesquioxane. The ladder structure does not trap hydroxides within the polymer molecule in the same fashion as a highly branched network structure would.

Appendix B is a compilation of the NMR study done for this research. In Appendix B, one can find individual spectra of all the samples run for this research and can compare the integral regions of each sample.

5.3.1.4 Fourier transform infrared spectroscopy

Fourier transform infrared spectroscopy (FT-IR) was used to gather information in regards to the structure of the silsesquioxanes. Literature has shown that there are two Si-O-Si bands found in FT-IR spectra of silsesquioxanes.(Lee et al. 2002) These bands have been correlated to the cage and network structure respectively. Transmission mode FT-IR was used to collect spectra. One drop of sample was placed between two salt windows. Spectra were compared for ratio of the cage and network structure to the organic group, which was used as a reference peak.

Fourier Transform Infrared Spectroscopy was employed in this research to quantify the structural nature of the synthesized silsesquioxanes. As reported in Chapter 3, there are two IR active peaks in silsesquioxanes which can be used to characterize the structure, 1120 cm^{-1} and 1030 cm^{-1} . These peaks represent the cage and network structures respectively. Figure 5-11 is a figure of the FTIR Spectra of the six silsesquioxanes studied in this research. Table 5-5 is the measured intensities of FTIR spectra of the silsesquioxanes studied in this research. One can see that polymethylsilsesquioxane and polyethylsilsesquioxane have similar ratios of network to cage. Additionally one can see that the rest of the silsesquioxanes also have similar ratios of network to cage. This would seem to indicate that R group has a limited influence on structure. Smaller R groups resulted in higher ratios of the two peaks, whereas larger groups resulted in smaller ratios. Polyvinylsilsesquioxane has an R group roughly the same size as polyethylsilsesquioxane but had a ratio lower than ethyl or methyl and

higher than the other three silsesquioxanes. It is possible that some sort of hydrogen bonding occurred between hydroxides and the vinyl groups resulting in the intermediate ratio of network to cage structure.

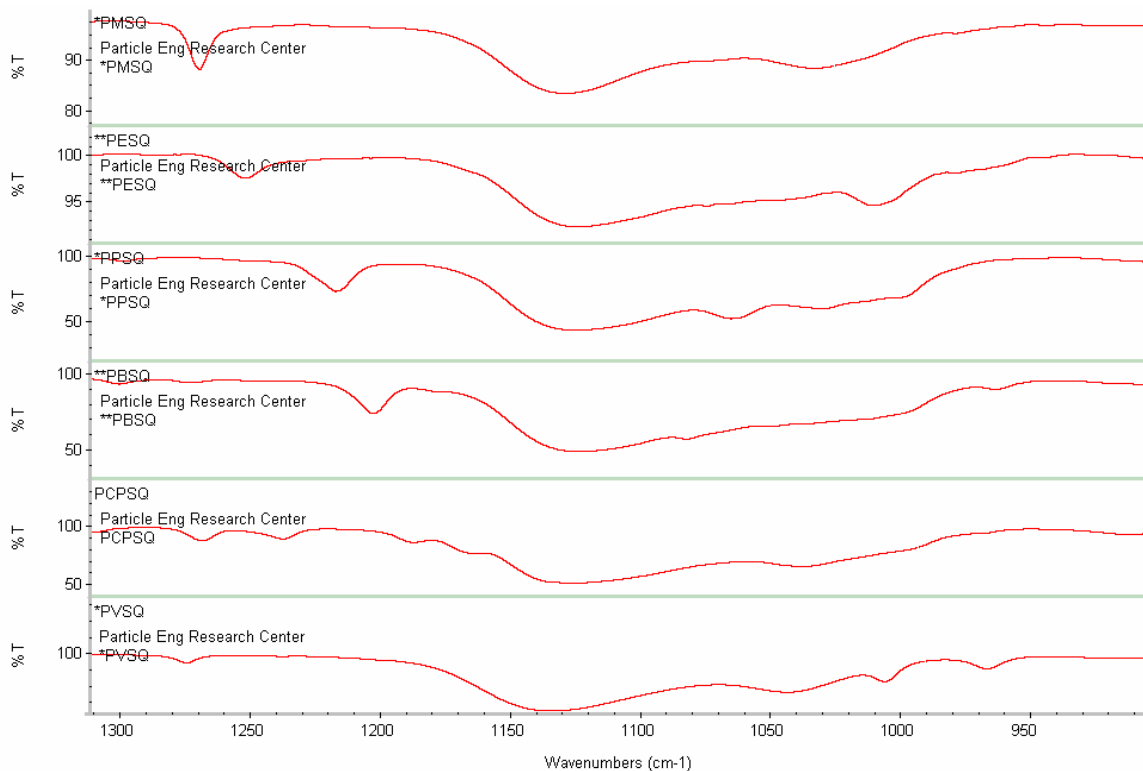


Figure 5-11 FTIR Spectra of Synthesized Silsesquioxanes

Table 5-5 Ratio of Network to Cage Structure of Silsesquioxanes from FTIR

PSQ	Cage	Network	Ratio N/C
Methyl	0.86	0.91	0.95
Ethyl	0.92	0.95	0.97
Propyl	0.48	0.62	0.77
Butyl	0.53	0.70	0.76
Vinyl	0.64	0.75	0.85
Chloropropyl	0.53	0.66	0.80

5.3.2 Condensation of Polysilsesquioxanes

Curing the synthesized silsesquioxanes presented a very difficult problem. Samples were cross-linked using tin octoate as a catalyst. Two separate solvents were

used, chloroform and carbon tetrachloride. These solvents were chosen because chloroform is a hydrogen bonding solvent and carbon tetrachloride is not. Additionally several different geometries and materials were employed to make the samples. Unlike the samples of epoxies, the silsesquioxanes could not be cast in a silicone mold because the solvent would swell the silicone and deform the mold.

Initially glass plates were used to cross-link the silsesquioxane. Two geometries were used, a single glass pane with the top surface exposed to air, and a double glass pane separated by a thin spacer. The double glass pane in all situations resulted in a resin that had very fine porosity which was a result of the evaporation of the solvent.

The single glass pane resulted in a material that was dense and non-porous, however, because one side was exposed to air and the other not, it resulted in an uneven curing process. After removal from the plate, the sample would slowly curl tighter. Experiments were performed to try and minimize this effect, such as allowing the sample to cure longer and at higher temperatures. This proved to be futile and either reduced the amount of curling, qualitatively measured, or did nothing at all.

Appendix C has been prepared as a list of tables of compositions of various silsesquioxanes studied in this work. Table C-1 in Appendix C is a list of the various compositions and configurations studied as part of this research.

5.3.3 Characterization of Nodular Microstructure

As previously mentioned, it has been reported that silsesquioxanes can form a nodular microstructure, as found in epoxies. The goal of this research was to investigate the nature of nodule formation by varying the properties of the polymer and polymer environment during curing. It was my hope that one could find a relationship between the R-group of the silsesquioxane and the nature of the solvent and nodule size. It was

my hypothesis that the nodules nucleated out of the solvent-polymer mixture, forming small nodules with high surface energy. The high surface energy would preferentially drive condensation reactions at the surface of the nodule. As the nodule grew, the difference in surface energy with the solution would begin to approach zero and slow down additional condensation at the surface. Originally it was intended that different R-groups on the silsesquioxanes and different solvents such as chloroform and carbon tetrachloride could be used to investigate this hypothesis.

It was found, however, that not all silsesquioxanes form truly nodular microstructures. In fact, it was found that only polymethylsilsesquioxane formed a nodular microstructure. The following pictures are SEM micrographs of methyl, ethyl, propyl, and butyl silsesquioxane. There does appear to be some structure in other silsesquioxanes, but not a nodular structure. Instead the structure appears to be two separate phases, an interconnected light and dark phase. This can be best seen in Figure 5-14 of polypropylsilsesquioxane. Figure 5-17 highlights the differences in phases.

From the pictures above some similarity may be viewed, but only the polymethylsilsesquioxane has a truly nodular microstructure. Figure 5-16 is a high magnification SEM micrograph of polymethylsilsesquioxane. One can see what appear to be very small nodules or clusters in this figure. One can estimate the size of these clusters to be approximately 20 nm in diameter. It is my assumption that these clusters are the primary building blocks of the nodules. The similar scale features can be found in the pictures of the other silsesquioxanes above. It is unknown at this time as to why only polymethylsilsesquioxane is nodular.

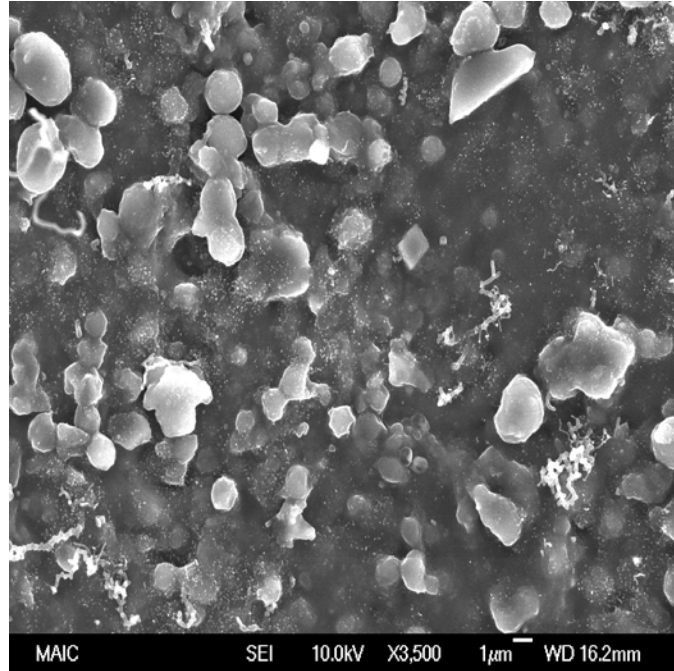


Figure 5-12 Polymethylsilsesquioxane Microstructure

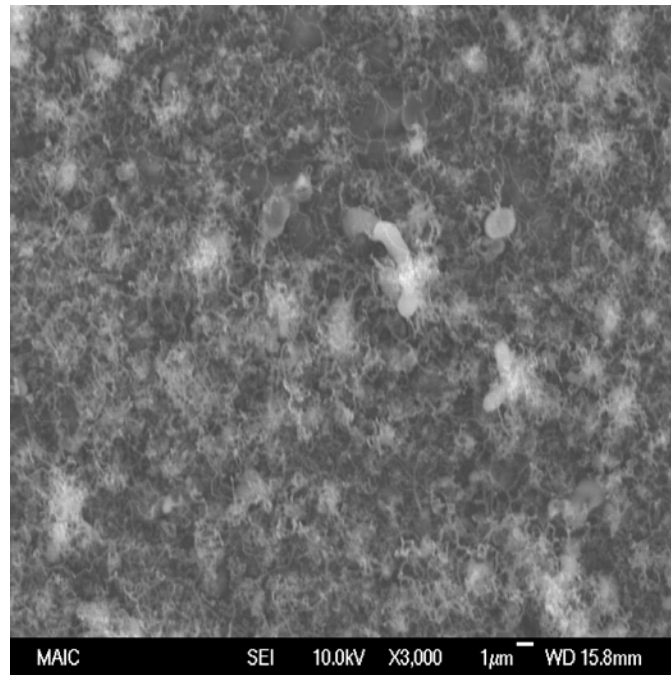


Figure 5-13 Polyethylsilsesquioxane Microstructure

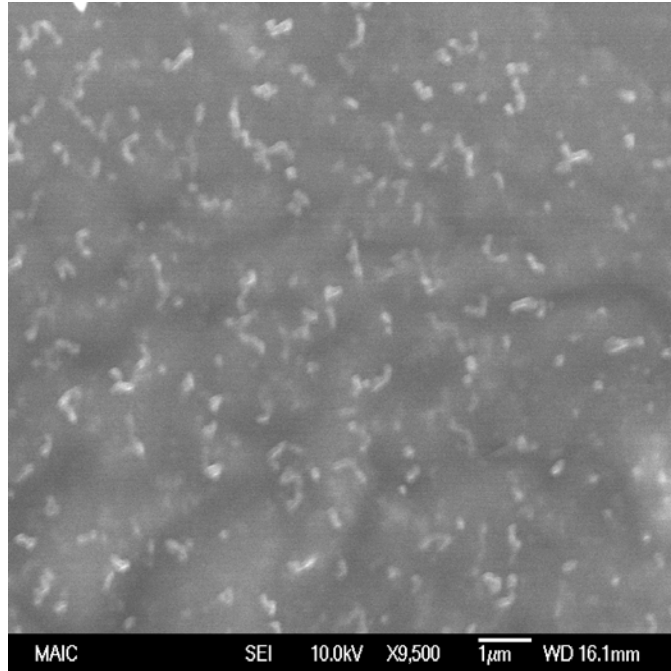


Figure 5-14 Polypropylsilsesquioxane Microstructure

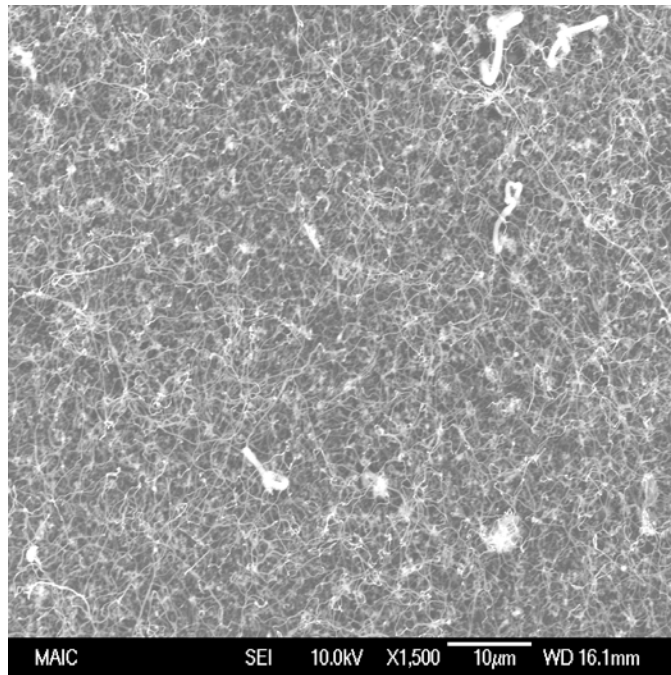


Figure 5-15 Polybutylsilsesquioxane Microstructure

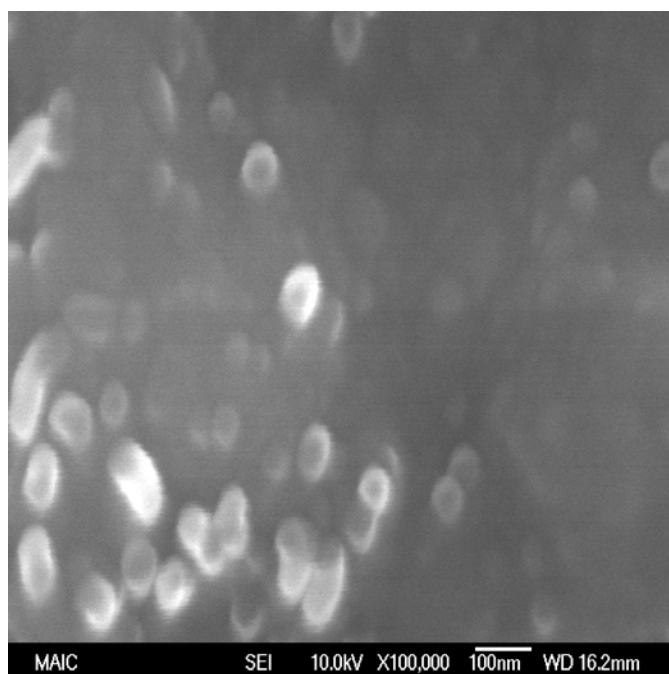


Figure 5-16 Polymethylsilsesquioxane Cluster Structure

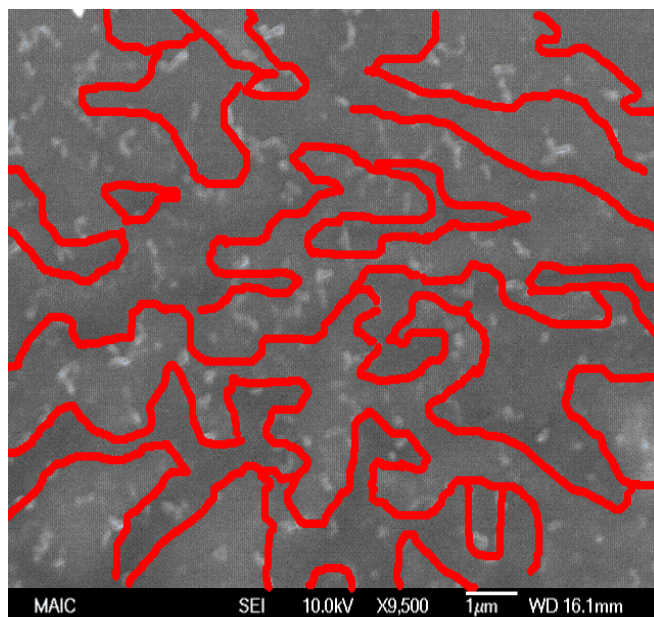


Figure 5-17 Highlighted Two-Phase Image of Polypropylsilsesquioxane

A possible explanation would be the small steric size of the methyl group allows for more possible configurations of a molecule and thus more intramolecular condensation. As a structure grows in the polymethylsilsesquioxane the polymer comes back around on itself, in other silsesquioxanes the larger groups would prevent the

molecule from bending back into the growing nodule and continue growth into a larger network.

5.4 Polymethylsilsesquioxane

It should be noted that prior to undertaking the main method of synthesis of polymethylsilsesquioxane described above, the author of this work experimented greatly with another route for synthesizing polymethylsilsesquioxane. The method used previously was originally described by Cao and Baney. (Baney et al. 1999) This technique used a mixture of methyltrimethoxysilane, methanol and a sub-stoichiometric amount of water which was then cast onto a polystyrene Petri dish. The solution was allowed to cure to a dense resin. Figure 5-18 is an SEM micrograph of a sample of polymethylsilsesquioxane generated with this technique. One can see in this picture that the Cao-Baney method of polymethylsilsesquioxane preparation also results in a nodular microstructure. This indicates that the formation of a nodular microstructure in polymethylsilsesquioxane is not dependent on a process.

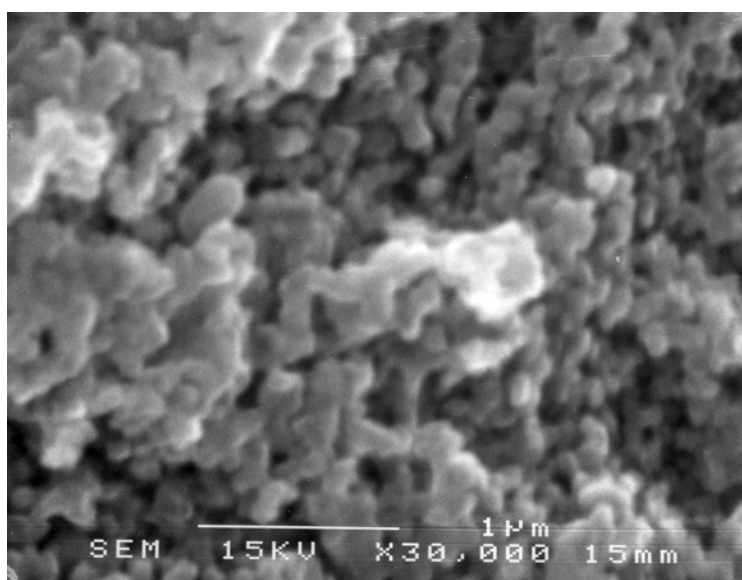


Figure 5-18 Cao-Baney Route Polymethylsilsesquioxane

5.6 Conclusions

The results found in this research have helped to better understand two-phase synthesis techniques for making silsesquioxanes. It was found that increasing temperature decreases viscosity. The decrease in viscosity is likely due to a lower molecular weight of the polymer. It is likely that at higher temperatures the silsesquioxanes experience a higher level of intramolecular condensation. It was not shown however that the increase in intramolecular condensation occurs on a short range order. That is, FTIR experiments do not indicate any increase in a short range cage structure versus a long range network structure.

Si-29 NMR was used to characterize the synthesized and derivitized silsesquioxane polymers. The larger R-group silsesquioxanes, ethyl, propyl, butyl, vinyl, and chloropropyl, appeared to have the same relative amounts of hydroxide, approximately 40%. Conversely, it was shown that the polymethylsilsesquioxane had approximately 20% hydroxide. Derivatization was used to determine the amount of reactive hydroxide present in the structure. It was shown that there is no trend between group size and reactive hydroxide content. Of note, it was found that the hydroxide content of polyvinylsilsesquioxane was totally reactive, and not locked within the structure of the molecule.

Originally it was hypothesized that silsesquioxane based resins could be used as a model for investigating the relationship between nodule size and toughness. It was shown by Cao and Baney that polymethylsilsesquioxane can form a nodular microstructure. In this research, five additional silsesquioxanes were synthesized, however, it was shown that only the polymethylsilsesquioxane forms a nodular structure. It is my hypothesis that this is due to the much lower content of hydroxide in the

methyilsilsesquioxanes than the other silsesquioxanes. As the polymethyilsilsesquioxane grows, the number of sites for additional condensation reactions greatly reduces. Additionally the tin-octoate acts as a catalyst for both intra- and intermolecular condensation. Since polymethyilsilsesquioxane already has a low content of hydroxide, it is possible that the catalyst enhanced intramolecular condensation greatly reduces the hydroxide sites for intermolecular condensation.

CHAPTER 6 RESULTS, DISCUSSIONS, AND FUTURE WORK

6.1 Results and Discussion

6.1.1 Calculating Fractal Dimension with Optical Microscopy

A new technique for calculating fractal dimension was developed for this work. This technique used optical microscopy to generate a three dimensional image of a fracture surface. The digital image was then sectioned using the software bundled with the microscope. The sectioned images were used to calculate fractal dimension. Fractal dimension was determined by using a Slit-Island technique popularized by Mandelbrot. (Mandelbrot et al. 1984)

It was shown through the course of this work that this technique returns fractal dimension values which are to be expected for the material studied. The results were compared to fractal dimension calculated for the same material using mirror to flaw size ratios. The algorithm used by the software was shown to be true by measuring the fractal dimension by hand using the compass-walk method.

6.1.2 Nodular Microstructure of Epoxies and Fractal Analysis of Failure

It was not shown conclusively that the size of the nodule in epoxy resins is directly related to the toughness through the West Mecholsky Passoja Theory. Table 6-1 lists the structural parameter a_0 values for the compositions and strain rates tested in this research. There seems to be some effect of strain rate on calculated a_0 values. At low strain rates a_0 was shown to be much higher.

Table 6-1 a_0 and Error Values for Epoxy Resins by Strain Rate

Strain Rate	8 phr DETA		10 phr DETA	
	$a_0(\mu\text{m})$	%Error	$a_0(\mu\text{m})$	%Error
0.1	4.1	53%	4.4	45%
10	3.0	68%	2.6	54%
100	2.1	68%	2.0	67%

The data in table 6-1 would seem to indicate that a_0 is not a static property but is affected by strain conditions. These results have led to another possible hypothesis for future work. It has been noted in the literature that a small percentage of the nodules in the microstructure are not bound to the microstructure. It can be hypothesized that a_0 is the distance between unbound nodules. At low strain rates, the structure can accommodate more strain before failure and thus the average distance between unbound nodule sites increases greatly. At high strain rates, the failure load and strain are smaller, therefore a_0 or the distance between unbound nodules remains low.

6.1.3 Synthesis and Characterization of Silsesquioxanes

Six different silsesquioxanes were synthesized for this research; methyl, ethyl, butyl, propyl, vinyl and chloropropyl. Originally, it was proposed that the silsesquioxanes could be used as a model for thermosetting resins. It had been previously shown that polymethylsilsesquioxane forms a nodular resin. Unfortunately for the purpose of this research it was found that only the polymethylsilsesquioxane forms a nodular microstructure. Additionally it was found that the techniques used to synthesize the silsesquioxane resins did not produce samples from which mechanical properties could be determined or that were statistically similar in structure.

Silsesquioxanes were extensively characterized for structure using Silicon 29-NMR and FTIR. It was found that the polymethylsilsesquioxane contained significantly less

hydroxide then the other silsesquioxanes. It was also found that methyl, ethyl and vinyl silsesquioxane had similar ratios of cage to network structure which were found to be lower than the other three silsesquioxanes studied. Also it was found empirically that the molecular weight of the polymethylsilsesquioxane was significantly higher than any of the other polymers.

From the Silicon 29-NMR, FTIR, and molecular weight data, one could theorize the reason as to why the polymethylsilsesquioxane forms nodules but none of the other silsesquioxanes do. It is possible the reason PMSQ forms a nodular microstructure is because of the reduced functionality due to high molecular weight and shown with NMR. As the synthesized polymer molecules begin to condense in the presence of catalyst, the amount of functionality decreases further resulting in fewer sites for more condensation. Eventually the nodule grows to a size where the surface functionality is effectively zero, which greatly hampers additional nodule growth. This does not occur in the other silsesquioxanes because there is a much greater initial concentration of hydroxides, due in part to the lower molecular weight.

6.2 Future Work

While the work presented here does seem to indicate a relationship between nodule sizes, nodule packing, and mechanical properties, more work should be done to further back this conclusion. To date, it is not entirely known as to why nodules form, or what parameter control nodule size. Additional work should be done to control nodule size. As mentioned in chapter 2, Koutsky has shown that surface energy may be a deciding factor in nodule size. It would be of interest to modify the silicone molds with various agents to change the surface energy. By using the same composition and different surface energy overall the bulk properties should remain the same such as modulus and

cross link density. These experiments would go a long way to showing if surface energy of a mold or substrate has a significant effect on nodule size.

It is still unknown how nodules differ from interstitial material. Techniques such as SAXS and AFM have not shown any difference between nodule and interstitial material, this has lead some groups to believe that nodules are artifacts of the imaging process and are not real. As mentioned in chapter 4, soaking a nodular epoxy resin in acetone for long periods of time results in some of the nodules diffusing out of the bulk. This would seem to indicate that the nodules are not well bound with the connective phase and would indicate that the functionality of the surface of a nodule is very low. It would be of interest to quantify the surfaces of nodules for functionality. Also it was postulated from the results that a_0 could be a function of the distance between nodules that are loosely connected to the matrix. Additional experiments could be used to investigate what portion of the nodules in the resin can be extracted from the body and then modeled to find average distance between nodules. It would be of interest to see if the distance between unbound nodules was proportional to a_0 .

Additional experiments should also be preformed to understand if the size of a_0 is specific to nodular epoxies or all epoxies. Further experiments could include calculating a_0 for epoxy resins that do not have any nodular microstructure. If similar a_0 values to what were found in this research were found for a non nodular epoxy resin that would seem to indicate that there is no direct correlation between nodule size, unbound nodules, and toughness. Additionally it was postulated in chapter 4 that the nodules could server a mechanism for crack tip deflection toughening. Experiments could be preformed measuring the toughness of two resins one nodular, and one non-nodular that have the

same crosslink density. These experiments would serve to not only show if nodules are a toughening mechanism but could also be used to compare a_0 values.

Lastly further experiments should be performed with silsesquioxanes to understand the formation of nodules in silsesquioxanes. Through the course of this research only the polymethylsilsesquioxane was shown to form a nodular microstructure. Larger R-Groups did not form nodular structures. It is not known why the larger R groups did not form nodular microstructures. It would be of interest to look at co-polymers of various silsesquioxanes with different R-Groups. By synthesizing silsesquioxane polymers with various ratios of precursors one should be able to empirically control molecular weight, hydroxide content, and structure. From there one could form a phase diagram of sort showing what regions form nodular structures.

There is still a large amount of work to be done for understanding how nodules form in both epoxies and silsesquioxanes. Assuming the distance between loosely or unbound nodules are the origin of a_0 , a better understanding of how nodules form and why they are more akin to inhomogeneities could lead to engineering a tougher thermoset resin.

APPENDIX A
ERROR ANALYSIS OF THE WEST MECHOLSKY PASSOJA THEORY

A.1 Introduction

Error analysis of an equation is a crucial step in understanding the effects of each variable on the output of an equation and how the associated error in measuring each variable affects the overall result. This appendix will serve as a thought exercise in understanding error in measurements and results and the effect on the West Mecholsky Passoja Theory.

The WMP Theory identifies three key variables that must be measured using any of a variety of techniques. These variables are the toughness, K_{Ic} , the fractal dimension D^* , and the modulus, E . Each of these variables introduces error into the final product. Because the equations investigated in the research are not simple linear addition equations, the cumulative error in a_0 is not a simple summation of the error of the variables. The cumulative error of an equation is defined as the square root of the sum of the squares of the partial derivative of the equation with respect to a variable times the error of the variable. The cumulative for any equation can be found from equation A-1

$$(A-1) \Delta E_T = \sqrt{\sum_{i=1}^j \left(\frac{\partial E_T}{\partial E_i} \Delta E_i \right)^2}$$

Where ΔE_T is the magnitude of the cumulative error for equation E_T , $\partial E_T / \partial E_i$ is the partial derivative of E_T with respect to variable i , and ΔE_i is the magnitude of the error of variable i .

A.2 Sources of Error

With any characterization process there are two sources of error, intrinsic and extrinsic. Intrinsic errors are generally those defined as independent of the test conditions. These are errors that are inherent to the testing process and are often extremely difficult to remove. Extrinsic errors are often errors introduced into the system or measurement by the user or an outside source. Extrinsic errors can be minimized by repeating the same experiment multiple times and averaging the results.

A.3 Error Analysis Equations

The WMP equation is defined in equation A-2. Equation A-3 is the WMP equation rearranged to solve for the structural parameter a_0 . Equation A-8 is the cumulative error associated with calculating a_0 and measuring the parameters K_{Ic} , D^* , and E . Equations A-4 through A-7 are the equations used to derive equation A-8.

$$(A-2) \quad K_{Ic} = E(a_0 D^*)^{1/2}$$

$$(A-3) \quad a_0 = \left(\frac{K_{Ic}^2}{E^2 D^*} \right)$$

$$(A-4) \quad \Delta a_0 = \sqrt{\left(\frac{\partial a_0}{\partial D^*} \Delta D \right)^2 + \left(\frac{\partial a_0}{\partial K_{Ic}} \Delta K_{Ic} \right)^2 + \left(\frac{\partial a_0}{\partial E} \Delta E \right)^2}$$

$$(A-5) \quad \frac{\partial a_0}{\partial D^*} = - \left(\frac{K_{Ic}^2}{E^2 D^{*2}} \right)$$

$$(A-6) \quad \frac{\partial a_0}{\partial K_{Ic}} = \left(\frac{2K_{Ic}}{E^2 D^*} \right)$$

$$(A-7) \quad \frac{\partial a_0}{\partial E} = \left(\frac{-2K_{Ic}^2}{E^3 D^*} \right)$$

$$(A-8) \Delta a_0 = \sqrt{\left(\left(\frac{K_{Ic}^2}{E^2 D^{*2}}\right)\Delta D\right)^2 + \left(\left(\frac{2K_{Ic}}{E^2 D^*}\right)\Delta K_{Ic}\right)^2 + \left(\left(\frac{-2K_{Ic}^2}{E^3 D^*}\right)\Delta E\right)^2}$$

Where K_{Ic} is the Toughness, ΔK_{Ic} is the magnitude of the error of K_{Ic} , E is the Modulus, ΔE is the magnitude of the error of E , D^* is fractal dimensional increment and ΔD^* is the magnitude of the error of D^* .

A.4 Error Analysis Graphs

Using equations A-3, A-8 were used to determine the effects of variables and error on the WMP theory. For each graph there are 3 separate sets of data plotted. Each data set represents the effect of a particular variable on the WMP theory or on the cumulative error. For each data set only the variable investigated was changed while the others remained constant, the values of which can be found in the figures. The values chosen are proportional to value measured in this research.

Effect of Variable on a_0

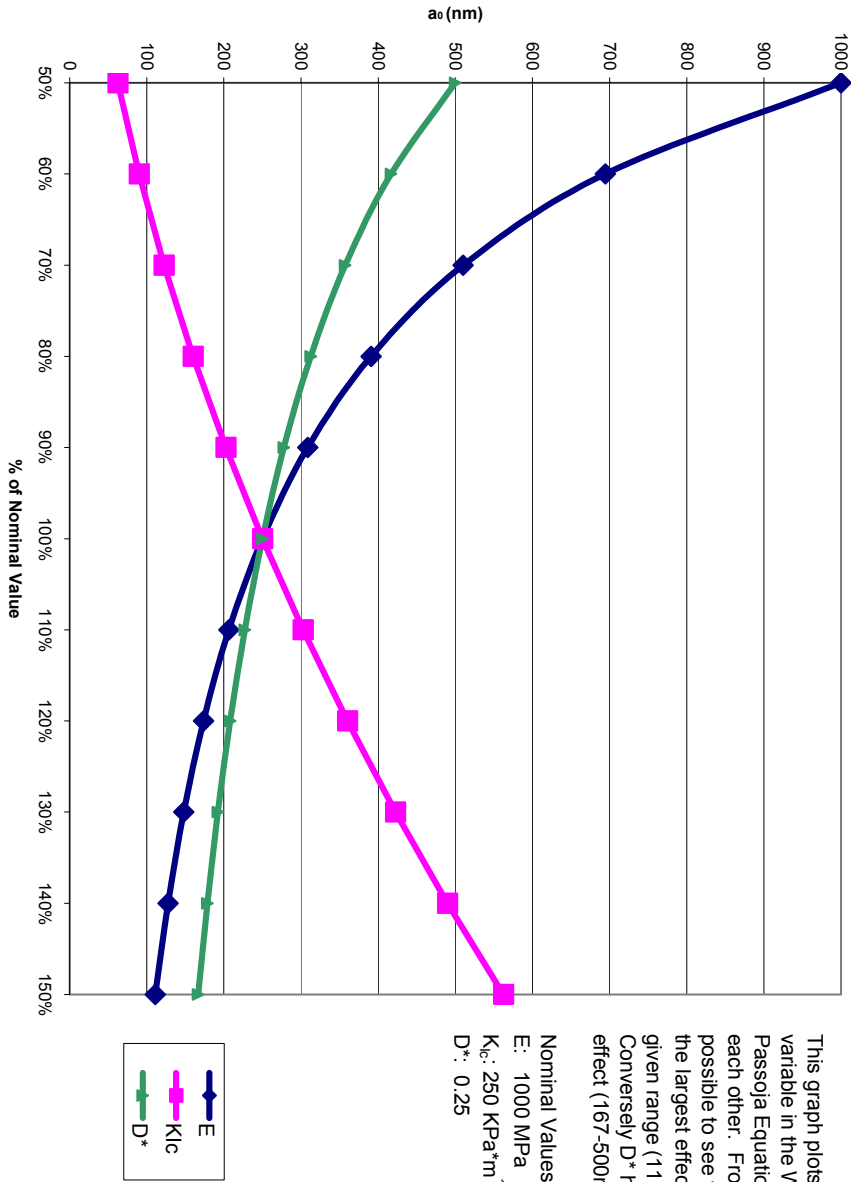


Figure A-1 Effect of Variables on a_0

This graph plots the effect of each variable in the West Mecholsky Passoja Equation with respect to each other. From this graph it is possible to see that modulus has the largest effect on a_0 over a given range (111-1000nm). Conversely D^* has the lowest net effect (167-500nm).

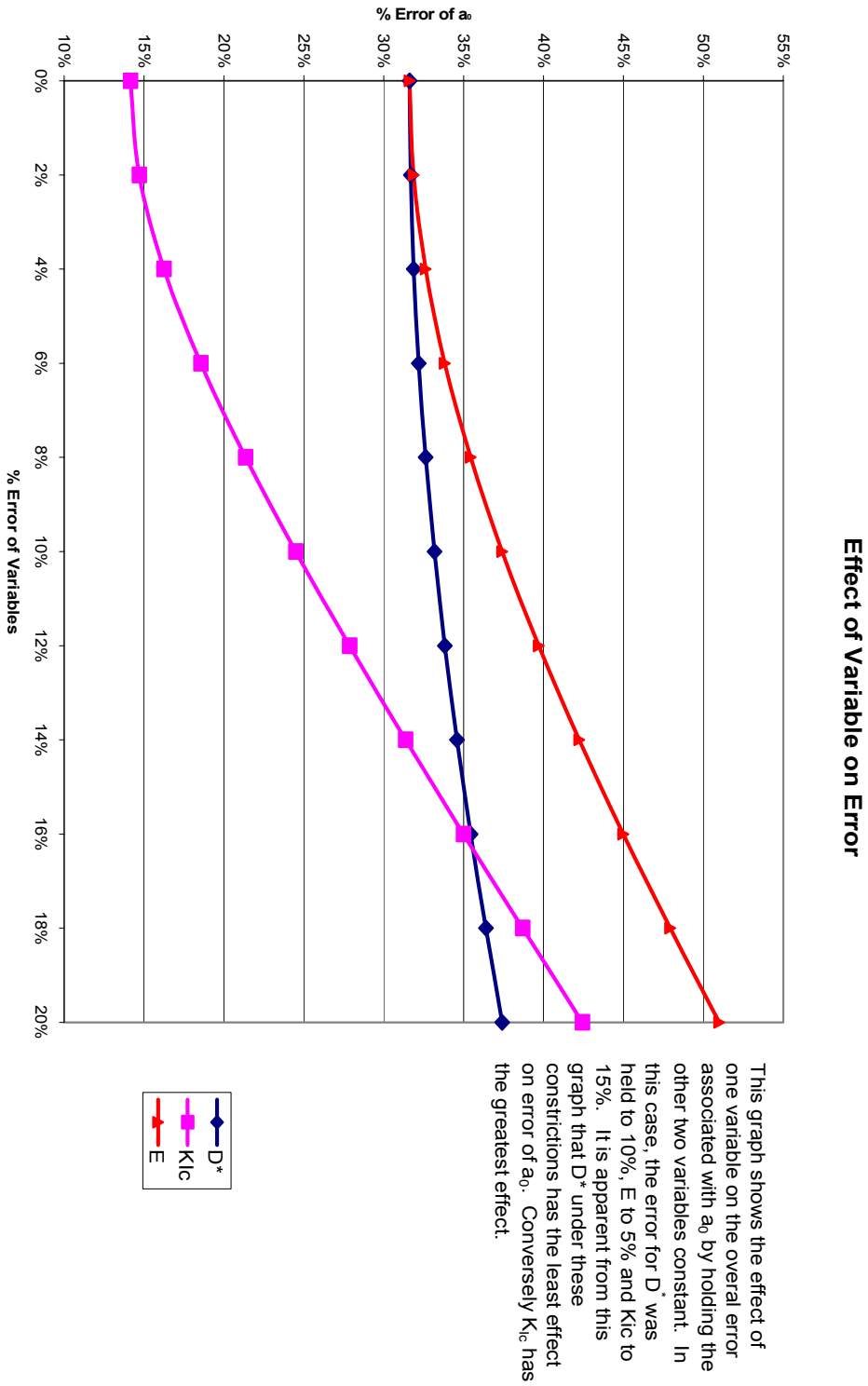


Figure A-2 Effect of Variables on Error of a_0

APPENDIX B
SILICON 29 NMR STUDY OF SILSESQUIOXANES

B.1 Introduction and Methodology

Silicon 29 NMR was used to characterize the amount of hydroxide present in synthesized silsesquioxane polymers. Additionally the silsesquioxane polymers were derivitized to determine the amount of reactive hydroxide present in the structure.

Samples were run on an Bruker Avance 600 MHz spectrometer tuned to the silicon 29 resonant frequency, for this particular machine the resonant frequency is approximately 119.23 MHz. Samples were dissolved in deuterated acetone to obtain a proper lock. Spectra were acquired for four hours or 5120 scans. Spectra were collected between zero and -130 ppm, with tetramethylsilane as the reference. Samples were run in high purity glass tubes. This resulted in a large SiO_4 peak which was removed through careful integration of peaks. The relevant peaks are found in chapter 5 and in the literature.(Kondo et al. 2000)

B.2 Si-29 NMR Spectra

The following figures are the NMR spectra gathered for this research. Present in each figure are the integrals used to find the concentration of each peak. The total hydroxide and reactive hydroxide content is tabulated in chapter 5.

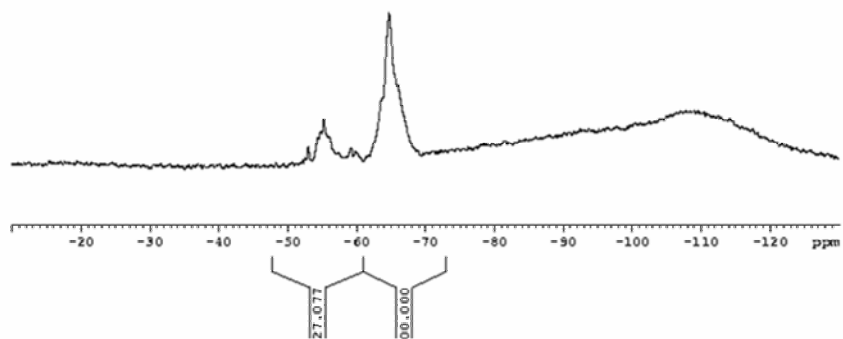


Figure B-1 Polymethylsilsequioxane

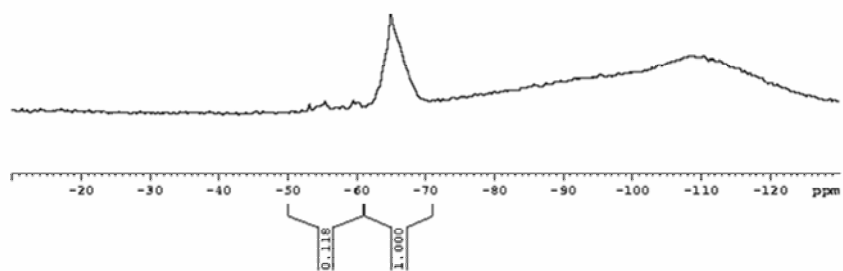


Figure B-2. Derivatized Polymethylsilsequioxane

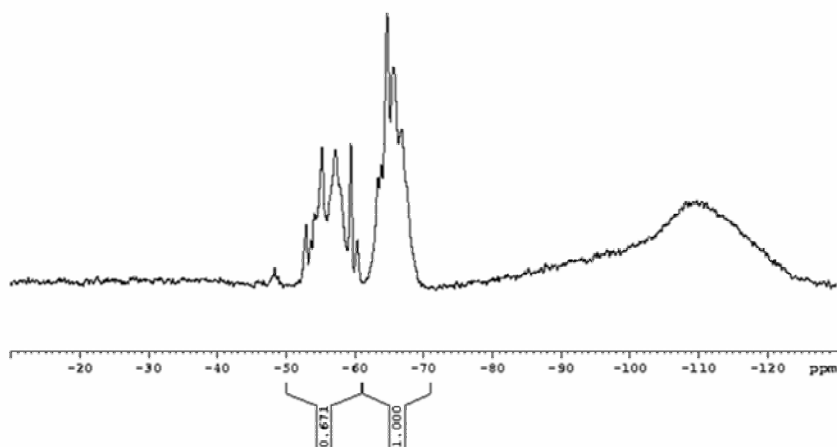


Figure B-3 Polyethylsilsesquioxane

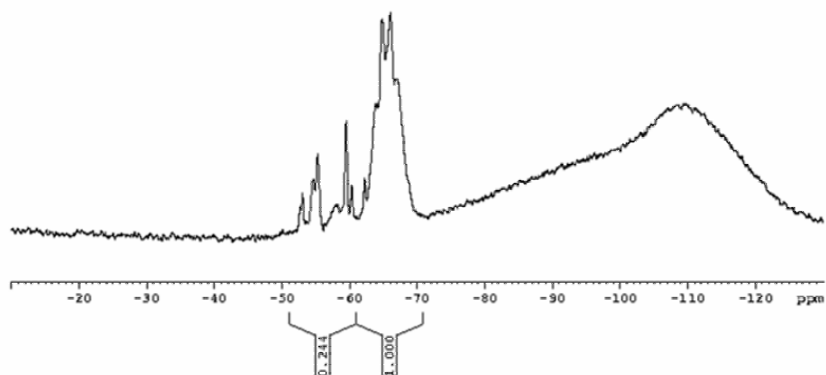


Figure B-4 Derivatized Polyethylsilsesquioxane

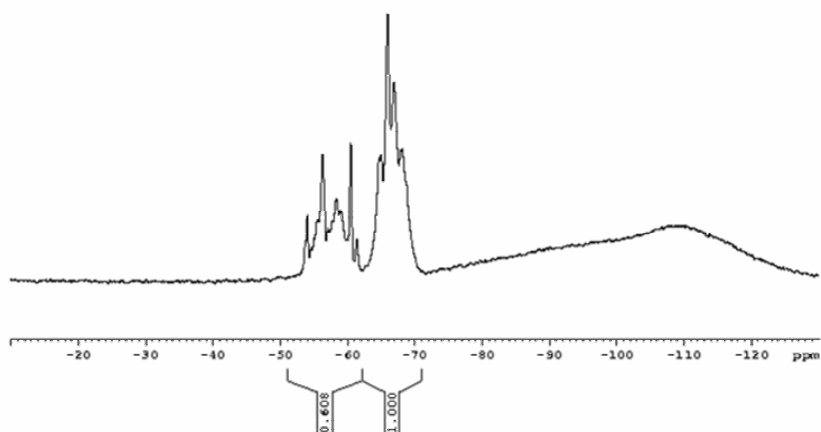


Figure B-5 Polypropylsilsesquioxane

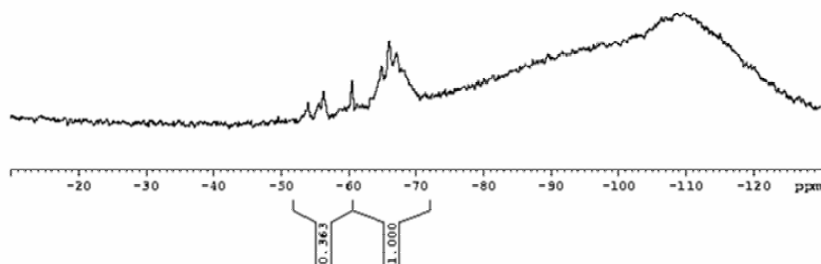


Figure B-6 Derivatized Polypropylsilsesquioxane

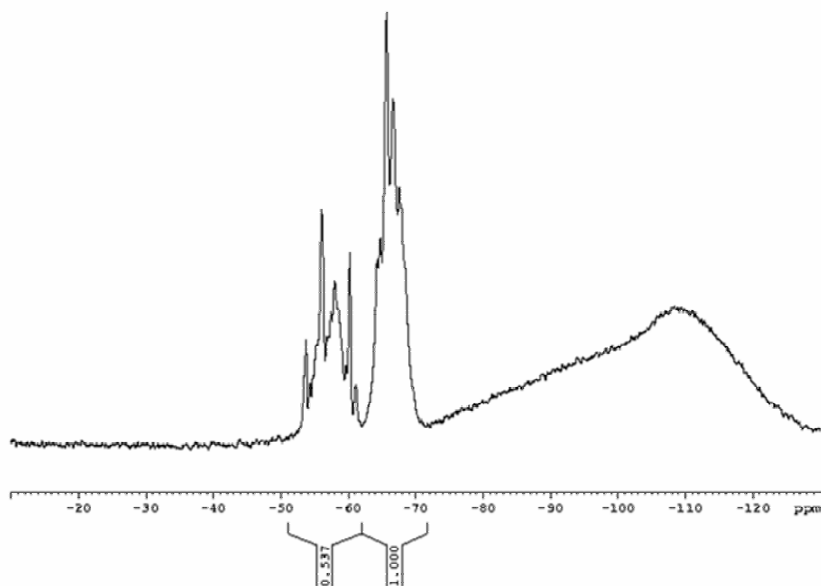


Figure B-7 Polybutylsilsesquioxane

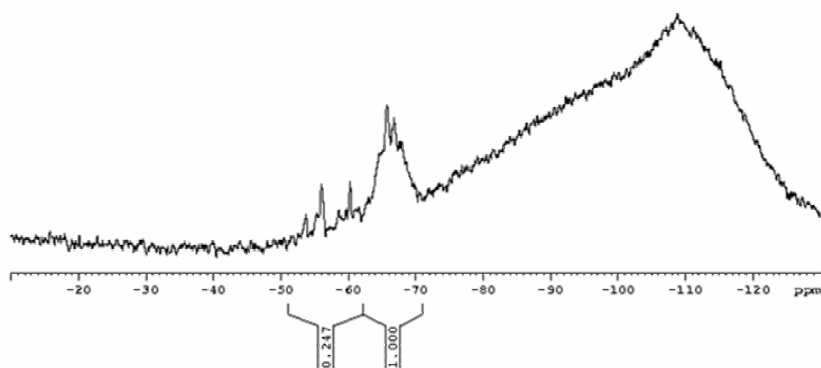


Figure B-8. Derivatized Polybutylsilsesquioxane

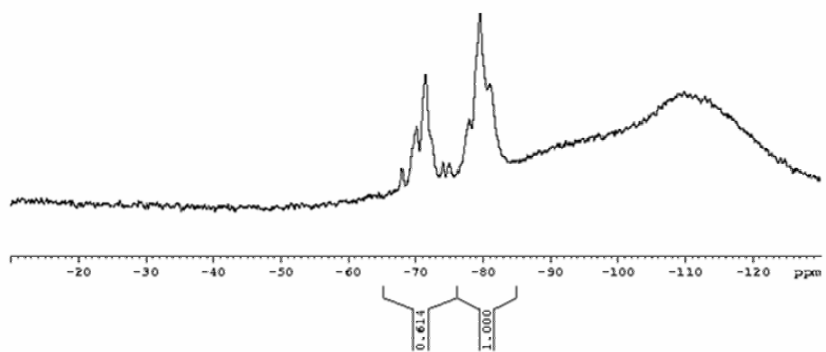


Figure B-9 Polyvinylsilsesquioxane

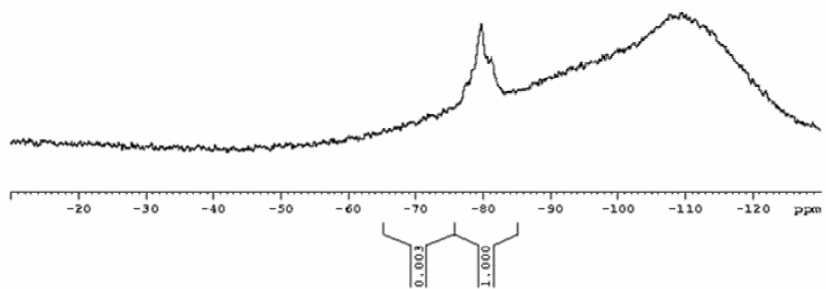


Figure B-10 Derivatized Polyvinylsilsesquioxane

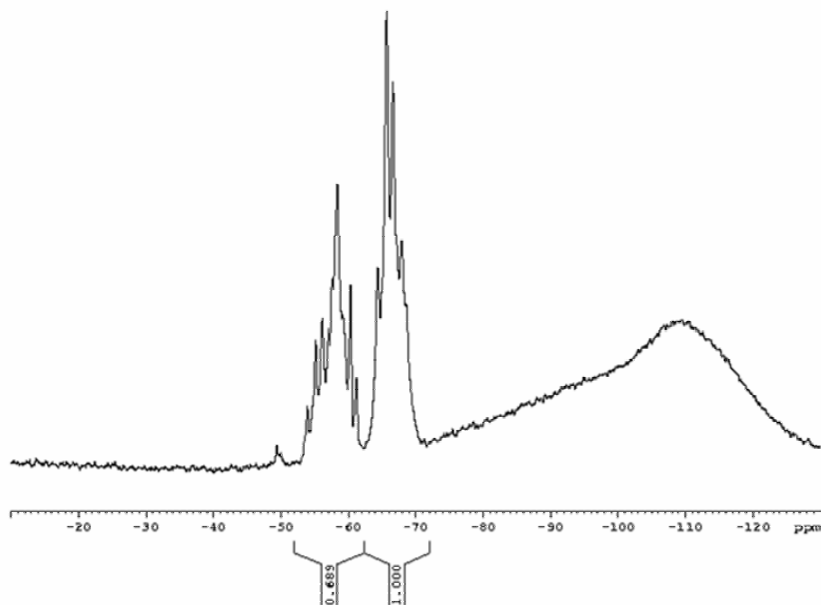


Figure B-11 Polychloropropylsilsequioxane

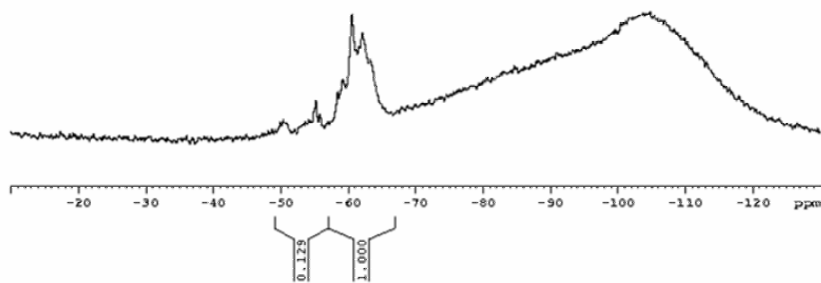


Figure B-12 Derivitized Polychloropropylsilsequioxane

APPENDIX C
STUDY OF POLYSILSEQUIOXANES

Table C-1 lists the compositions studied in this research. The samples above are the polysilsesquioxanes synthesized to investigate the nature of the cross linked polysilsesquioxane. The codes for Table C-1 can be found at the end of the table.

Table C-1. Crosslinked Silsesquioxane Compositions

#	PSQ	Sol	PSQ Con	Tin Con	Ratio ($\mu\text{l/ml}$)	Substrate
1	M	1	80	10	50/10	1
2	M	1	80	10	50/10	2
3	M	1	80	10	50/10	3
4	M	1	80	10	50/10	4
5	M	1	50	10	50/10	1
6	M	1	50	10	50/10	2
7	M	2	50	10	50/10	3
8	M	2	50	10	50/10	4
9	M	2	50	10	50/10	1
10	M	2	50	10	50/10	1
11	E	1	80	10	50/10	1
12	E	1	80	10	50/10	2
13	E	1	80	10	50/10	3
14	E	1	80	10	50/10	4
15	E	1	80	10	100/10	1
16	E	1	80	10	100/10	2
17	E	1	80	10	100/10	3
18	E	1	80	10	100/10	4
19	E	2	60	10	50/10	1
20	E	2	60	10	50/10	2
21	E	2	60	10	50/10	3
22	E	2	60	10	50/10	4
23	E	1	60	5	50/10	1
24	E	1	60	5	150/10	1
25	E	1	60	5	250/10	1
26	M	1	60	5	100/10	1
27	M	2	60	5	100/10	2
28	M	3	60	5	100/10	3
29	M	4	60	5	100/10	4
30	E	1	60	5	100/10	1

31	E	1	60	5	100/10	2
32	E	1	60	5	100/10	3
33	E	1	60	5	100/10	4
34	P	1	60	5	100/10	1
35	P	1	60	5	100/10	2
36	P	1	60	5	100/10	3
37	P	1	60	5	100/10	4
38	B	1	60	5	100/10	1
39	B	1	60	5	100/10	2
40	B	1	60	5	100/10	3
41	B	1	60	5	100/10	4
42	V	1	60	5	100/10	1
43	V	1	60	5	100/10	2
44	V	1	60	5	100/10	3
45	V	1	60	5	100/10	4
46	CP	1	60	5	100/10	1
47	CP	1	60	5	100/10	2
48	CP	1	60	5	100/10	3
49	CP	1	60	5	100/10	4
50	M	1	20	5	50/10	1

- The # is the sample number tested
- PSQ is the polysilsesquioxane investigated in that sample, M = Methyl, E = Ethyl, P = Propyl, B = Butyl, V = Vinyl, CP = Chloropropyl
- Sol is the solvent investigated, 1 = Chloroform, 2 = Carbon Tetrachloride, 3 = Acetone, 4 = Decane
- PSQ Con is the concentration of the polysilsesquioxane in the solvent by mass
- Tin Con is the concentration of Tin Octoate in the solvent
- Ratio is the ratio of Tin Octoate solution to polysilsesquioxane solution in microliters to milliliters.
- Substrate is the configuration of substrate investigated. 1 = Single Glass Pane, 2 = Double Glass Pane, 3 = Single Teflon Coated Pane, 4 = Double Teflon Coated Pane

APPENDIX D
MEASUREMENTS OF EPOXY SAMPLES

This appendix has been prepared to list the individual measurements made upon samples in chapter four. The following tables are broken up by composition, strain rate and sample number. Error was calculated as the width of one standard deviation.

Table D-1 Modulus Values for Epoxy Samples

Sample	Modulus (MPa)					
	8 phr DETA			10 phr DETA		
	0.1mm	10mm	100mm	0.1mm	10mm	100mm
1	1466	1421	1602	1380	1358	1406
2	1298	1427	1602	1284	1487	1441
3	1443	1437	1482	1392	1437	1462
4	1453	1339	1626	1439	1463	1471
5	1311	1341	1783	1368	1356	1424
6	1500	1453	1391	1463	1428	1435
7	1455	1492	1363	1469	1366	1405
8	1383	1463	1465	1429	1451	1443
9	1366	1551	1374	1422	1430	1436
10	1444	1523	1398	1424	1388	1435
Average	1412	1445	1509	1407	1416	1436
Std Dev	69	69	139	54	46	21
Error	4.9%	4.8%	9.2%	3.9%	3.3%	1.5%

Table D-2 Failure Stress Values for Epoxy Samples

Sample	Failure Stress (σ_f)					
	8 phr DETA			10 phr DETA		
	0.1mm	10mm	100mm	0.1mm	10mm	100mm
1	60	53	69	68	83	68
2	60	76	67	75	69	53
3	57	74	89	68	56	47
4	56	73	98	64	89	64
5	62	78	48	68	68	70
6	64	78	91	70	88	67
7	58	78	91	72	86	94
8	59	80	87	67	72	75
9	62	71	37	68	54	38
10	62	76	67	70	85	69
Average	60	74	74	69	75	64
Std Dev	2	8	21	3	13	16
Error	3.9%	10.5%	27.7%	4.3%	17.4%	24.4%

Table D-3 Flaw Size and Toughness Measurements for Epon 825 with 8phr DETA Strained at 0.1 mm/min

Sample	2a	2b	a	b	c	Location	Y	σ_f	K_{Ic}
1	416	333	208	167	186	Surface	1.26	60	1039
2	1255	968	628	484	551	Body	1.13	60	1598
3	690	976	345	488	410	Surface	1.26	57	1468
4	893	908	447	454	450	Surface	1.26	56	1513
5	724	618	362	309	334	Surface	1.26	62	1426
6	239	166	120	83	100	Body	1.13	64	721
7	691	614	346	307	326	Surface	1.26	58	1334
8	694	414	347	207	268	Surface	1.26	59	1219
9	827	792	414	396	405	Surface	1.26	62	1565
10	566	1036	283	518	383	Surface	1.26	62	1531

Table D-4 Flaw Size and Toughness Measurements for Epon 825 with 8phr DETA Strained at 10 mm/min

Sample	2a	2b	a	b	c	Location	Y	σ_f	K_{Ic}
1	219	176	110	88	98	Surface	1.26	53	666
2	477	377	239	189	212	Body	1.13	76	1252
3	134	156	67	78	72	Surface	1.26	74	790
4	623	760	312	380	344	Body	1.13	73	1531
5	633	258	317	129	202	Surface	1.26	78	1406
6	290	228	145	114	129	Surface	1.26	78	1123
7	480	513	240	115	166	Surface	1.26	78	1272
8	155	169	78	116	95	Surface	1.26	80	981
9	120	70	60	117	84	Surface	1.26	71	820
10	382	297	191	118	150	Body	1.13	76	1054

Table D-5 Flaw Size and Toughness Measurements for Epon 825 with 8phr DETA
Strained at 100 mm/min

Sample	2a	2b	a	b	c	Location	Y	σ_f	K_{Ic}
1	331	119	165.5	59.5	99.2	Surface	1.264	69	863
2	221	240	110.5	120	115.2	Surface	1.264	67	904
3	246	206	123	103	112.6	Surface	1.264	89	1069
4	202	426	101	213	146.7	Surface	1.264	98	1340
5	611	598	305.5	299	302.2	Body	1.128	48	932
6	401	262	200.5	131	162.1	Body	1.128	91	1313
7	176	179	88	89.5	88.7	Body	1.128	91	966
8	No	Flaw	X	X	X	X	X	X	NF
9	303	272	151.5	136	201.5	Body	1.128	87	1393
10	998	536	499	268	365.7	Body	1.128	37	798

Table D-6 Flaw Size and Toughness Measurements for Epon 825 with 10phr DETA
Strained at 0.1 mm/min

Sample	2a	2b	a	b	c	Location	Y	σ_f	K_{Ic}
1	772	563	386	282	330	Surface	1.264	68	1566
2	953	916	477	458	467	Surface	1.264	75	1832
3	1176	1000	588	500	542	Surface	1.264	68	1798
4	617	550	309	275	291	Surface	1.264	64	1378
5	557	452	279	226	251	Surface	1.264	68	1360
6	600	424	300	212	252	Surface	1.264	70	1396
7	1128	593	564	297	409	Surface	1.264	72	1632
8	250	600	125	300	194	Surface	1.264	67	1177
9	977	980	489	490	489	Surface	1.264	68	1889
10	772	564	386	282	330	Surface	1.264	70	1603

Table D-7 Flaw Size and Toughness Measurements for Epon 825 with 10phr DETA
Strained at 10 mm/min

Sample	2a	2b	a	b	c	Location	Y	σ_f	K_{Ic}
1	598	376	299	188	237.1	Surface	1.264	83	1445
2	540	860	270	430	340.7	Body	1.128	69	1440
3	248	188	124	94	108.0	Surface	1.264	56	732
4	350	428	175	214	193.5	Surface	1.264	89	1560
5	237	228	118.5	114	116.2	Surface	1.264	68	933
6	111	121	55.5	60.5	57.9	Surface	1.264	88	845
7	612	450	306	225	262.4	Surface	1.264	86	1566
8	504	770	252	385	311.5	Surface	1.264	72	1597
9	524	478	262	239	250.2	Surface	1.264	54	1081
10	524	398	262	199	228.3	Surface	1.264	85	1629

Table D-8 Flaw Size and Toughness Measurements for Epon 825 with 10phr DETA Strained at 100 mm/min

Sample	2a	2b	a	b	c	Location	Y	σ_f	K_{Ic}
1	179	378	89.5	189	130.1	Surface	1.264	68	980
2	235	200	117.5	100	108.4	Surface	1.264	53	694
3	212	180	106	90	97.7	Surface	1.264	47	587
4	No	Flaw	Visible	X	X	X	X	X	NF
5	400	400	200	200	200.0	Surface	1.264	70	1259
6	150	150	75	75	75.0	Surface	1.264	67	732
7	714	302	357	151	232.2	Body	1.128	54	652
8	90	99	45	49.5	47.2	Surface	1.264	75	652
9	400	300	200	150	173.2	Surface	1.264	38	627
10	106	140	53	70	60.9	Surface	1.264	69	682

Table D-9 Mirror Measurements for Epon 825 with 8phr DETA Strained at 0.1mm/min

Sample	c	M1	M2	MA	D*
1	186.1	1306	1320	1313	0.14
2	551.1	1856	1695	1776	0.31
3	410.3				
4	450.2				
5	334.5	1501	1397	1449	0.23
6	99.6	718	644	681	0.15
7	325.7	1269	1453	1361	0.24
8	268.0	1224	1194	1209	0.22
9	404.7	1559	1370	1465	0.28
10	382.9	1348	1515	1432	0.27

Table D-10 Mirror Measurements for Epon 825 with 8phr DETA Strained at 10mm/min

Sample	c	M1	M2	MA	D*
1	98	1100	1241	1171	0.08
2	212	1029	1014	1022	0.21
3	72	622	791	707	0.10
4	344	1368	1211	1290	0.27
5	202	1111	812	962	0.21
6	129	1364	1234	1299	0.10
7	166	868	1026	947	0.18
8	95	670	778	724	0.13
9	84	969	606	788	0.11
10	150	1110	1241	1176	0.13

Table D-11 Mirror Measurements for Epon 825 with 8phr DETA Strained at 100mm/min

Sample	c	M1	M2	MA	D*
1	99.2	695	885	784	0.13
2	115.2	945	1239	1082	0.11
3	112.6	676	724	700	0.16
4	146.7	561	859	894	0.16
5	302.2				
6	162.1	907	982	944	0.17
7	88.7	964	842	901	0.10
8					
9	201.5	1089	1095	1092	0.18
10	365.7	1890	1890	1890	0.19

Table D-12 Mirror Measurements for Epon 825 with 10phr DETA Strained at 0.1mm/min

Sample	c	M1	M2	MA	D*
1	330	1046	1005	1026	0.32
2	467	1827	1827	1827	0.26
3	542	1554	1544	1549	0.35
4	291	1430	1328	1379	0.21
5	251	1300	952	1126	0.22
6	252	1343	978	1161	0.22
7	409	1855	2060	1958	0.21
8	194	1333	1500	1417	0.14
9	489				
10	330	1667	1767	1717	0.19

Table D-13 Mirror Measurements for Epon 825 with 10phr DETA Strained at 10mm/min

Sample	c	M1	M2	MA	D*
1	237.1	727	1083	905	0.261979
2	340.7	1820	1657	1738.5	0.195993
3	108.0	412	374	393	0.274715
4	193.5	1036	1036	1036	0.186795
5	116.2	1183	1183	1183	0.098249
6	57.9	356	277	316.5	0.183084
7	262.4	1120	1120	1120	0.234279
8	311.5	1355	1321	1338	0.232795
9	250.2	1157	1198	1177.5	0.212515
10	228.3	817	874	845.5	0.270062

Table D-14 Mirror Measurements for Epon 825 with 8phr DETA Strained at 100mm/min

Sample	c	M1	M2	MA	D*
1	130.1	1206	1190	1198	0.11
2	108.4	1355	1360	1357.5	0.08
3	97.7	918	1234	1076	0.09
4					
5	200.0	907	980	943.5	0.21
6	75.0	1135	979	1057	0.07
7	232.2	1641	1328	1484.5	0.16
8	47.2	329	320	324.5	0.15
9	173.2	1752	1412	1582	0.11
10	60.9	1195	1410	1302.5	0.05

Table D-15 Image Pro Measurements for Fractal Dimensional Increment by Sample

Sample #	8 phr DETA			10 phr DETA		
	0.1mm	10mm	100mm	0.1mm	10mm	100mm
1	0.25	0.19	0.18	0.26	0.13	0.19
2	0.20	0.22	0.19	0.21	0.15	0.14
3	0.22	0.21	0.15	0.23	0.19	0.16
4	0.24	0.20	0.19	0.17	0.14	0.15
5	0.26	0.18	0.21	0.22	0.16	0.17
6	0.19	0.15	0.16	0.26	0.19	0.14
7	0.22	0.19	0.17	0.23	0.21	0.18
8	0.21	0.14	0.19	0.27	0.23	0.18
9	0.18	0.19	0.19	0.23	0.16	0.19
10	0.23	0.18	0.18	0.25	0.17	0.15

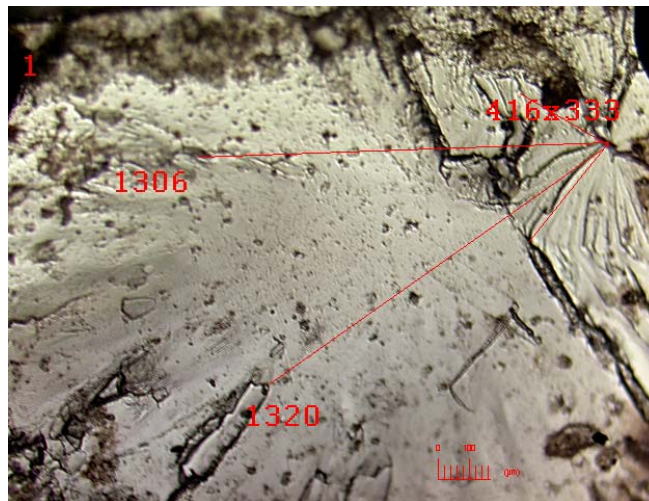


Figure D-1 Flaw Size of Epon 825 with 8phr DETA Strained at 0.1 mm/min

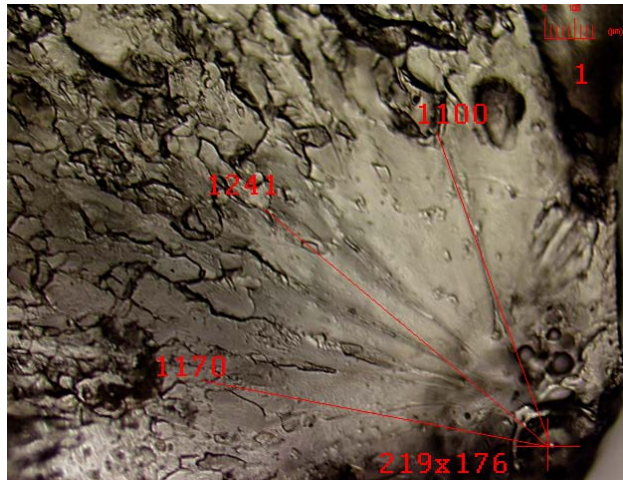


Figure D-2 Flaw Size of Epon 825 with 8phr DETA Strained at 10 mm/min

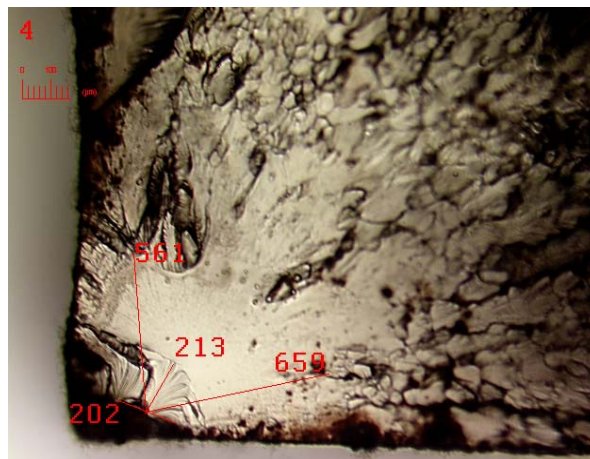


Figure D-3 Flaw Size of Epon 825 with 8phr DETA Strained at 100 mm/min

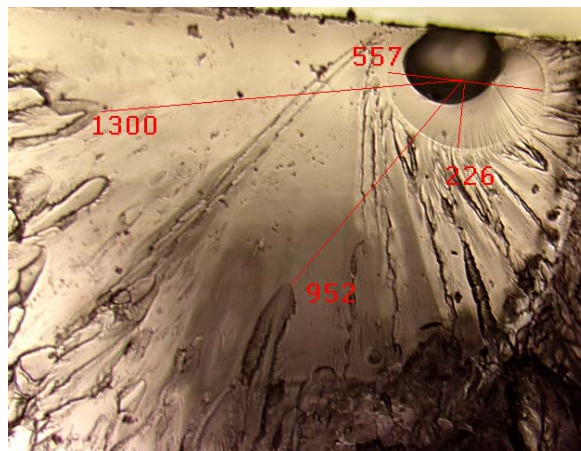


Figure D-4 Flaw Size of Epon 825 with 8phr DETA Strained at 100 mm/min

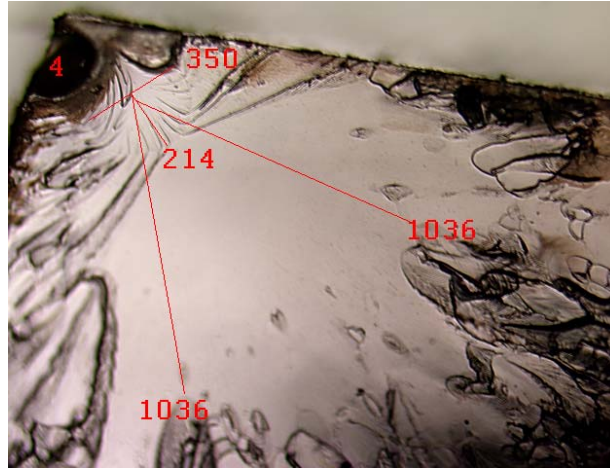


Figure D-5 Flaw Size of Epon 825 with 10phr DETA Strained at 10 mm/min

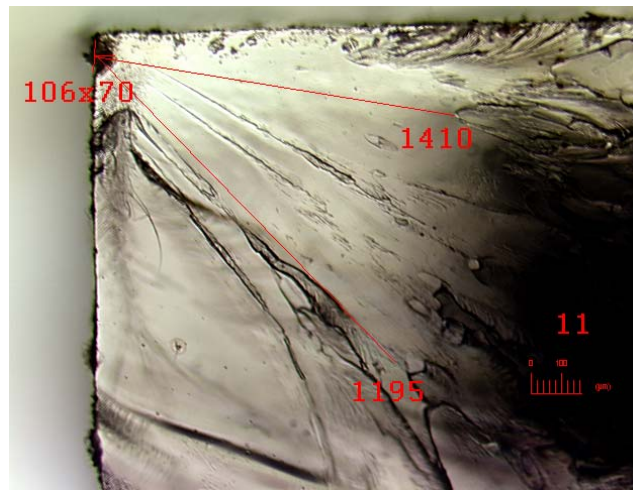


Figure D-6 Flaw Size of Epon 825 with 10phr DETA Strained at 100 mm/min

LIST OF REFERENCES

- Anderson, S. E., Baker, E. S., Mitchell, C., Haddad, T. S. and Bowers, M. T. (2005). "Structure of hybrid polyhedral oligomeric silsesquioxane propyl methacrylate oligomers using ion mobility mass spectrometry and molecular mechanics." Chemistry of Materials **17**(10): 2537-2545.
- Araki, W., Adachi, T., Yamaji, A. and Gamou, M. (2002). "Fracture toughness of bisphenol A-type epoxy resin." Journal of Applied Polymer Science **86**(9): 2266-2271.
- Arkles, B. and Larson, G. (2004). Silicon Compounds: Silanes and Silicones. Morrisville, PA, Gelest.
- Arthur, S. (2005). Fractal Explorer 2.02.
- Auad, M. L., Borrajo, J. and Aranguren, M. I. (2003). "Morphology of rubber-modified vinyl ester resins cured at different temperatures." Journal of Applied Polymer Science **89**(1): 274-283.
- Babadagli, T. and Develi, K. (2001). "On the application of methods used to calculate the fractal dimension of fracture surfaces." Fractals-Complex Geometry Patterns and Scaling in Nature and Society **9**(1): 105-128.
- Babonneau, F., Bois, L., Yang, C. Y. and Interrante, L. V. (1994). "Sol-Gel synthesis of a siloxypolycarbosilane gel and Its pyrolytic conversion to silicon oxycarbide." Chemistry of Materials **6**(1): 51-57.
- Bai, S. J. (1985). "Crosslink distribution of epoxy networks studied by small-angle neutron-scattering." Polymer **26**(7): 1053-1057.
- Bailey, J. K., Bangert, R. K., Schweitzer, J. A., Trotter, R. T., Shuster, S. M. and Whitham, T. G. (2004). "Fractal geometry is heritable in trees." Evolution **58**(9): 2100-2102.
- Balankin, A. S. (1995). "Mechanics of self-affine cracks." Revista Mexicana De Fisica **41**(4): 473-479.
- Baney, R. and Cao (1999). "Unpublished results presented to the University of Florida and Dow Corning."

- Baney, R. H., Itoh, M., Sakakibara, A. and Suzuki, T. (1995). "Silsesquioxanes." Chemical Reviews **95**(5): 1409-1430.
- Bigerelle, M. and Iost, A. (2004). "Statistical artefacts in the determination of the fractal dimension by the slit island method." Engineering Fracture Mechanics **71**(7-8): 1081-1105.
- Borodich, F. M. (1997). "Some fractal models of fracture." Journal of the Mechanics and Physics of Solids **45**(2): 239-259.
- Borodich, F. M. (1999). "Fractals and fractal scaling in fracture mechanics." International Journal of Fracture **95**(1-4): 239-259.
- Bourget, L., Leclercq, D. and Vioux, A. (1999). "Catalyzed nonhydrolytic sol-gel route to organosilsesquioxane gels." Journal of Sol-Gel Science and Technology **14**(2): 137-147.
- Brinker, C. J. and Scherer, G. W. (1989). Sol-Gel Science. San Diego, Academic Press.
- Bujalski, D. R., Grigoras, S., Lee, W. L. N., Wieber, G. M. and Zank, G. A. (1998). "Stoichiometry control of SiOC ceramics by siloxane polymer functionality." Journal of Materials Chemistry **8**(6): 1427-1433.
- Carpinteri, A., Cornetti, P., Barpi, F. and Valente, S. (2003). "Cohesive crack model description of ductile to brittle size-scale transition: dimensional analysis vs. renormalization group theory." Engineering Fracture Mechanics **70**(14): 1809-1839.
- Carpinteri, A. and Pugno, N. (2004). "Evolutionary fractal theory of erosion and experimental assessment on MIR space station." Wear **257**(3-4): 408-413.
- Carpinteri, A., Spagnoli, A. and Vantadori, S. (2002). "An approach to size effect in fatigue of metals using fractal theories." Fatigue & Fracture of Engineering Materials & Structures **25**(7): 619-627.
- Charkaluk, E., Bigerelle, M. and Iost, A. (1998). "Fractals and fracture." Engineering Fracture Mechanics **61**(1): 119-139.
- Chen, Z. and Mecholsky, J. J. (1993). "Control of strength and toughness of ceramic-metal laminates using interface design." Journal of Materials Research **8**(9): 2362-2369.
- Chen, Z., Mecholsky, J. J., Joseph, T. and Beatty, C. L. (1997). "The fractal geometry of Si₃N₄ wear and fracture surfaces." Journal of Materials Science **32**(23): 6317-6323.

- Crouzet, L., Leclercq, D., Mutin, P. H. and Vioux, A. (2003). "Organic-inorganic materials by nonhydrolytic sol-gel processes: Organosilsesquioxane-metal oxide hybrids." Journal of Sol-Gel Science and Technology **26**(1-3): 335-338.
- Della Bona, A., Hill, T. J. and Mecholsky, J. J. (2001). "The effect of contour angle on fractal dimension measurements for brittle materials." Journal of Materials Science **36**(11): 2645-2650.
- dell'Erba, I. E., Fasce, D. P., Williams, R. J. J., Erra-Balsells, R., Fukuyama, Y. and Nonami, H. (2004). "Epoxy networks modified by a new class of oligomeric silsesquioxanes bearing multiple intramolecular rings formed through Si-O-C bonds." Macromolecular Materials and Engineering **289**(4): 315-323.
- Dubuc, B., Quiniou, J. F., Roquesarmes, C., Tricot, C. and Zucker, S. W. (1989). "Evaluating the fractal dimension of profiles." Physical Review A **39**(3): 1500-1512.
- Duchet, J. and Pascault, J. P. (2003). "Do epoxy-amine networks become inhomogeneous at the nanometric scale?" Journal of Polymer Science Part B-Polymer Physics **41**(20): 2422-2432.
- Dusek, K. (1986). "Network formation in curing of epoxy-resins." Advances in Polymer Science **78**: 1-59.
- Dusek, K., Plestil, J., Lednický, F. and Lunak, S. (1978). "Are cured epoxy-resins inhomogeneous." Polymer **19**(4): 393-397.
- Eguchi, K. and Zank, G. A. (1998). "Silicon oxycarbide glasses derived from polymer precursors." Journal of Sol-Gel Science and Technology **13**(1-3): 945-949.
- Errath, E. H. and Spurr, R. A. (1959). "Occurrence of globular formations in thermosetting resins." Journal of Polymer Science **35**: 391.
- Falgarone, E., Hily-Blant, P. and Levrier, F. (2004). "Structure of molecular clouds." Astrophysics and Space Science **292**(1-4): 89-101.
- Falkenhagen, J., Jancke, H., Kruger, R. P., Rikowski, E. and Schulz, G. (2003). "Characterization of silsesquioxanes by size-exclusion chromatography and matrix-assisted laser desorption/ionization time-of-flight mass spectrometry." Rapid Communications in Mass Spectrometry **17**(4): 285-290.
- Fan, H. Y., Kathan, K., Bently, H., Clem, P. and Brinker, C. J. (2001). "Self-assembled aerogel-like low dielectric constant films." Journal of Non-Crystalline Solids **285**((1-3)): 79-83.
- Gleick, J. (1998). Chaos, London, Penguin.

- Green, D. J. (1998). An introduction to the mechanical properties of ceramics. Cambridge, Cambridge University Press.
- Gupta, V. B., Drzal, L. T., Adams, W. W. and Omlor, R. (1985). "An electron-microscopic study of the morphology of cured epoxy-resin." Journal of Materials Science **20**(10): 3439-3452.
- Hill, T. J., Della Bona, A. and Mecholsky, J. J. (2001). "Establishing a protocol for measurements of fractal dimensions in brittle materials." Journal of Materials Science **36**(11): 2651-2657.
- Hill, T. J., Mecholsky, J. J. and Anusavice, K. J. (2000). "Fractal analysis of toughening behavior in 3BaO center dot 5SiO(2) glass-ceramics." Journal of the American Ceramic Society **83**(3): 545-552.
- Issa, M. A., Islam, M. S. and Chudnovsky, A. (2003). "Fractal dimension - a measure of fracture roughness and toughness of concrete." Engineering Fracture Mechanics **70**(1): 125-137.
- Issa, M. A., Issa, M. A., Islam, M. S. and Chudnovsky, A. (2003). "Fractal dimension--a measure of fracture roughness and toughness of concrete." Engineering Fracture Mechanics **70**(1): 125-137.
- Jo, W. H. and Ko, K. J. (1991). "The effects of physical aging on the thermal and mechanical-properties of an epoxy polymer." Polymer Engineering and Science **31**(4): 239-244.
- Joseph, T., Chen, Z., Mecholsky, J. J. and Beatty, C. (1998). "Using fractal dimensions to characterize atomic force microscope images of epoxy resin fracture surfaces." Scanning **20**(2): 99-103.
- Kim, J. (2004). Thermal and hydrothermal stability of selected polymers in a nuclear reactor environment. Materials Science and Engineering. Gainesville, University of Florida: 186.
- Kondo, T., Yoshii, K., Horie, K. and Itoh, M. (2000). "Photoprobe study of siloxane polymers. 3. Local free volume of polymethylsilsesquioxane probed by photoisomerization of azobenzene." Macromolecules **33**(10): 3650-3658.
- Kozlov, G. V., Bejev, A. A. and Lipatov, Y. S. (2004). "The fractal analysis of curing processes of epoxy resins." Journal of Applied Polymer Science **92**(4): 2558-2568.
- Kurtz, S. M., Pruitt, L., Jewett, C. W., Crawford, R. P., Crane, D. J. and Edidin, A. A. (1998). "The yielding, plastic flow and fracture behavior of ultra-high molecular weight polyethylene used in total joint replacements." Biomaterials **19**: 1989-2003.

- Lee, L. H., Chen, W. C. and Liu, W. C. (2002). "Structural control of oligomeric methyl silsesquioxane precursors and their thin-film properties." Journal of Polymer Science Part a-Polymer Chemistry **40**(10): 1560-1571.
- Lopez, J., Ramirez, C., Abad, M. J., Barral, L., Cano, J. and Diez, F. (2002). "Dynamic mechanical analysis of an epoxy/thermoplastic blend: polymerization-induced phase separation." Polymer International **51**(10): 1100-1106.
- Lyu, S. P., Zhu, X. G. and Qi, Z. N. (1994). "Correlation between the fractal dimension of fracture surfaces and fracture-toughness for ductile polymer materials." Journal of Polymer Science Part B-Polymer Physics **32**(13): 2151-2154.
- Mandelbrot, B. B. (1967). "How long is the coast of Britain? Statistical self-similarity and fractal dimension." Science **155**: 636.
- Mandelbrot, B. B. (1977). Fractals: Form, Chance, and Dimension. San Francisco, W.H. Freeman.
- Mandelbrot, B. B., Passoja, D. E. and Paullay, A. J. (1984). "Fractal character of Fracture surfaces of metals." Nature **308**(5961): 721-722.
- Matyi, R. J., Uhlmann, D. R. and Koutsky, J. A. (1980). "Structure of glassy-polymers .7. Small-Angle X-Ray-Scattering from Epoxy-Resins." Journal of Polymer Science Part B-Polymer Physics **18**(5): 1053-1063.
- McEwen, C. N., Jackson, C. and Larsen, B. S. (1997). "Instrumental effects in the analysis of polymers of wide polydispersity by MALDI mass spectrometry." International Journal of Mass Spectrometry and Ion Processes **160**(1-3): 387-394.
- Mecholsky, J. J. and Freiman, S. W. (1991). "Relationship between fractal geometry and fractography." Journal of the American Ceramic Society **74**(12): 3136-3138.
- Mecholsky, J. J., West, J. K. and Passoja, D. E. (2002). "Fractal dimension as a characterization of free volume created during fracture in brittle materials." Philosophical Magazine a-Physics of Condensed Matter Structure Defects and Mechanical Properties **82**(17-18): 3163-3176.
- Mijovic, J. and Koutsky, J. A. (1979). "Correlation between nodular morphology and fracture properties of cured epoxy-resins." Polymer **20**(9): 1095-1107.
- Mijovic, J. and Tsay, L. (1981). "Correlations between dynamic mechanical-properties and nodular morphology of cured epoxy-resins." Polymer **22**(7): 902-906.
- Mijovic, J., Williams, J. G. and Donnellan, T. (1985). "Processing-morphology-property relationships in epoxy-resins." Journal of Applied Polymer Science **30**(6): 2351-2366.

- Mijovic, J. S. and Koutsky, J. A. (1977). "Etching of polymeric surfaces - Review." Polymer-Plastics Technology and Engineering **9**(2): 139-179.
- Mijovic, J. S. and Koutsky, J. A. (1979). "Effect of post cure time on the fracture properties and nodular morphology of an epoxy-resin." Journal of Applied Polymer Science **23**(4): 1037-1042.
- Mori, H., Lanzendorfer, M. G., Muller, A. H. E. and Klee, J. E. (2004). "Silsequioxane-based nanoparticles formed via hydrolytic condensation of organotriethoxysilane containing hydroxy groups." Macromolecules **37**(14): 5228-5238.
- Oberlin, A., Ayache, J., Oberlin, M. and Guigon, M. (1982). "High-resolution dark-field imaging in epoxy and polyimide systems." Journal of Polymer Science Part B- Polymer Physics **20**(4): 579-591.
- Oh, W., Shin, T. J., Ree, M., Jin, M. Y. and Char, K. (2002). "Residual stress evolution in dielectric thin films prepared from poly(methylsilsequioxane) precursor." Macromolecular Chemistry and Physics **203**(5-6): 801-811.
- Orcel, G., Gould, R. W. and Hensch, L. L. (1986). SAXS study of silica sols and gels. Better Ceramics Through Chemistry II. D. R. Ulrich. Pittsburgh, Materials Research Society. **73**: 289-294.
- Plangsammas, L., Mecholsky, J. J. and Brennan, A. B. (1999). "Determination of fracture toughness of epoxy using fractography." Journal of Applied Polymer Science **72**(2): 257-268.
- Pollard, M. and Kardos, J. L. (1987). "Analysis of epoxy-resin curing kinetics using the Avrami theory of phase-change." Polymer Engineering and Science **27**(11): 829-836.
- Racich, J. L. and Koutsky, J. A. (1976). "Nodular structure in epoxy-resins." Journal of Applied Polymer Science **20**(8): 2111-2129.
- Richardson, L. F. (1961). "The problem of contiguity: an appendix to statistics of deadly quarrels." General Systems Yearbook **6**: 139-187.
- Schaefer, D. W. and Keefer, K. D. (1986). Fractal aspects of ceramic synthesis. Better Ceramics Through Chemistry II. D. R. Ulrich. Pittsburgh, Materials Research Society. **73**: 277-288.
- Stach, S. and Cybo, J. (2003). "Multifractal description of fracture morphology: theoretical basis." Materials Characterization **51**(1): 79-86.
- Stach, S., Cybo, J. and Chmiela, J. (2001). "Fracture surface -- fractal or multifractal?" Materials Characterization **46**(2-3): 163-167.

- Stach, S., Roskosz, S., Cybo, J. and Cwajna, J. (2003). "Multifractal description of fracture morphology: investigation of the fractures of sintered carbides." Materials Characterization **51**(1): 87-93.
- Stemp, W. J. and Stemp, M. (2003). "Documenting stages of polish development on experimental stone tools: Surface characterization by fractal geometry using UBM laser profilometry." Journal of Archaeological Science **30**(3): 287-296.
- Stevens, G. C., Champion, J. V. and Liddell, P. (1982). "Investigation of local order in unreacted DGEBA epoxy-resin monomers by light-scattering." Journal of Polymer Science Part B-Polymer Physics **20**(2): 327-344.
- Su, Y. and Lei, W. S. (2000). "Relationship between fracture toughness and fractal dimension of fracture surface of steel." International Journal of Fracture **106**(3): L43-L48.
- Takahama, T. and Geil, P. H. (1982). "Structural Inhomogeneities of Cured Epoxy-Resins." Makromolekulare Chemie-Rapid Communications **3**(6): 389-394.
- Takamura, N., Gunji, T., Hatano, H. and Abe, Y. (1999). "Preparation and properties of polysilsesquioxanes: Polysilsesquioxanes and flexible thin films by acid-catalyzed controlled hydrolytic polycondensation of methyl- and vinyltrimethoxysilane." Journal of Polymer Science Part a-Polymer Chemistry **37**(7): 1017-1026.
- Tecklenburg, R. E., Wallace, W. E. and Chen, H. P. (2001). "Characterization of a $(O_3/2SiMe)_x(OSi(OH)Me)_y(OSiMe_2)_z$ silsesquioxane copolymer resin by mass spectrometry." Rapid Communications in Mass Spectrometry **15**(22): 2176-2185.
- Turcotte, D. L. (1992). "Fractals, chaos, self-organized criticality and tectonics." Terra Nova **4**(1): 4-12.
- Vanlandingham, M. R., Eduljee, R. F. and Gillespie, J. W. (1999). "Relationships between stoichiometry, microstructure and properties for amine-cured epoxies." Journal of Applied Polymer Science **71**(5): 699-712.
- Volland, S. and Kruhl, J. H. (2004). "Anisotropy quantification: the application of fractal geometry methods on tectonic fracture patterns of a Hercynian fault zone in NW Sardinia." Journal of Structural Geology **26**(8): 1499-1510.
- Wallace, W. E., Guttman, C. M. and Antonucci, J. M. (1999). "Molecular structure of silsesquioxanes determined by matrix-assisted laser desorption/ionization time-of-flight mass spectrometry." Journal of the American Society for Mass Spectrometry **10**(3): 224-230.
- Wallace, W. E., Guttman, C. M. and Antonucci, J. M. (2000). "Polymeric silsesquioxanes: degree-of-intramolecular-condensation measured by mass spectrometry." Polymer **41**(6): 2219-2226.

- Wang, C. Y., Zheng, J. Z., Shen, Z. X., Xu, Y., Lim, S. L., Liu, R. and Huan, A. C. H. (1999). "Characterization of a low-k organic spin-on-glass as an intermetal dielectric." Surface and Interface Analysis **28**(1): 97-100.
- Watchman, J. B. (1996). Mechanical Properties of Ceramics. New York, John Wiley & Sons.
- West, J. K., Mecholsky, J. J. and Hench, L. L. (1999). "The application of fractal and quantum geometry to brittle fracture." Journal of Non-Crystalline Solids **260**(1-2): 99-108.
- Woo, E. M., Seferis, J. C. and Bravenec, L. D. (1991). "Processing-structure relationships for multiphase epoxy matrix systems." Journal of Materials Science **26**(6): 1691-1698.
- Wu, C. S. (1991). "Effect of stirring on morphology and properties in a catalyst cured epoxy system." Journal of Applied Polymer Science **43**(8): 1421-1429.
- Wu, W. L. and Bauer, B. J. (1985). "Network structure of epoxies .1. A neutron-scattering study." Polymer Communications **26**(2): 39-42.
- Xie, H., Wang, J.-A. and Kwasniewski, M. A. (1999). "Multifractal characterization of rock fracture surfaces." International Journal of Rock Mechanics and Mining Sciences **36**(1): 19-27.
- Xie, H., Wang, J.-a. and Stein, E. (1998). "Direct fractal measurement and multifractal properties of fracture surfaces." Physics Letters A **242**(1-2): 41-50.
- Yang, S., Pai, J. C. H., Pai, C. S., Dabbagh, G., Nalamasu, O., Reichmanis, E., Seputro, J. and Obeng, Y. S. (2001). "Processing and characterization of ultralow-dielectric constant organosilicate." Journal of Vacuum Science & Technology B **19**(6): 2155-2161.

BIOGRAPHICAL SKETCH

Kyle Kathan was born in Clarksboro, New Jersey, where he lived with his parents Chris and Russ Kathan, and sister, Kendra. Kyle graduated high school in 1997 from Kingsway Regional High School with a strong interest in math and science. After graduating from high school, he attended Rutgers University in New Brunswick, New Jersey, where he studied ceramic engineering and materials science. Dr. Kathan first developed a love for silicon chemistry while working for Jeff Brinker at Sandia National Labs on a NSF research experience for undergraduates program. After graduating from Rutgers University, Kyle enrolled in the University of Florida to pursue a Ph.D. in Materials Science and Engineering in the fall of 2001. Kyle was married to Dana Cole of Ocala, Florida on August 7th, 2004.